Short-Wave Vortex Instabilities in Stratified Flow

by

Luke Bovard

A thesis
presented to the University of Waterloo
in fulfillment of the
thesis requirement for the degree of
Master of Mathematics
in
Applied Mathematics

Waterloo, Ontario, Canada, 2013

I hereby declare that I am the sole author of this thesis. This is a true copy of the thesis, including any required final revisions, as accepted by my examiners.

I understand that my thesis may be made electronically available to the public.

Abstract

Density stratification is one of the essential underlying physical mechanisms for atmospheric and oceanic flow. As a first step to investigating the mechanisms of stratified turbulence, linear stability plays a critical role in determining under what conditions a flow remains stable or unstable. In the study of transition to stratified turbulence, a common vortex model, known as the Lamb-Chaplygin dipole, is used to investigate the conditions under which stratified flow transitions to turbulence. Numerous investigations have determined that a critical length scale, known as the buoyancy length, plays a key role in the breakdown and transition to stratified turbulence. At this buoyancy length scale, an instability unique to stratified flow, the zigzag instability, emerges. However investigations into sub-buoyancy length scales have remained unexplored. In this thesis we discover and investigate a new instability of the Lamb-Chaplyin dipole that exists at the sub-buoyancy scale. By numerically performing the linear stability analysis we show that this short-wave instability exhibits growth rates similar to that of the zigzag instability. We conclude with nonlinear studies of this short-wave instability and demonstrate this new instability saturates at a level proportional to the cube of the aspect ratio.

Acknowledgements

Thanks to my supervisor Dr. Michael Waite. Additional thanks goes to Dr. Marek Stastna and Dr. Francis Poulin.

Obligatory thanks to everyone else who I have learnt from and talked to over all these year. There are too many to name, so I won't. Just know that if you knew me I'd probably thank you. This saves me having to remember people and just cover everyone in one full swoop.

The work for this thesis was written under the music of, in order of most played, Queen, Taylor Swift, The Beatles, Dire Straits, and Billy Joel. I kept statistics and it works out to be a few thousands plays of each, which is probably about 4 days straight of music per artists!

Richard you wanted me to add you punching Chris by mistake many years ago to this thesis. Here you go.

Special thanks to Patricia for conversations during the last few months. It made writing this thesis much easier. Thanks et merci y gracias por todo.

Finally, and most importantly, I dedicate this thesis to the two best teachers I've ever had. Without both of them, who knows where I'd be now.

Dedication

To Dr. Edward Vrscay and Dr. Jamal Sakhr.

Table of Contents

List of Figures

ix

Chapter 1

Introduction

Vortices play a fundamental role in the transition to turbulence by providing a mechanism to cascade energy from large to small scales. In the atmosphere and ocean, vortices are strongly influenced by density stratification and the rotation of the earth. However, stratification dominates at intermediate length scales – the small-scale end of the atmospheric mesoscale and the oceanic submesoscale – which are small enough for the Coriolis effects to be weak, but large enough for the stable density stratification to be strong (e.g. [52, 54, 65]). There has recently been much work, using full direct numerical simulations of the Boussinesq equations with various initial configurations, to uncover the emergence and evolution of stratified turbulence from vortices [2, 3, 20, 66]. Turbulence in this regime is governed by the Reynolds number $Re = UR/\nu$ as well as the horizontal Froude number $F_h = U/NR$, where U is the characteristic velocity, R is the characteristic horizontal length, N is the Brunt-Väisälä frequency, and ν is the kinematic viscosity. Because of this extra dependence on the Froude number, the underlying dynamics are not as well understood and a full picture of stratified turbulence is not complete [38, 52, 53, 54, 65].

In large-scale atmosphere and ocean simulations, it is difficult or impossible to resolve all possible processes. As a result, obtaining a proper parameterisation of small-scale phenomena is critical to correctly modelling the evolution. A useful approach to investigating these small-scale dynamics is to consider the transition problem in an idealised flow, which can elucidate the key features that govern the more comprehensive turbulence problem. One model that may be used to study the transition to stratified turbulence is that of a columnar counter-rotating vortex dipole. There is a large body of literature on the instability of vortex dipoles in unstratified fluids, including the Crow instability at large length scales (e.g. [19, 70, 36]) and the elliptic instability at smaller scales (e.g. [70, 49, 4, 68]). In stratified fluids, laboratory and numerical experiments of dipoles have uncovered an

instability unique to stratified flow, the zigzag instability, so named due to the zigzag-like structure exhibited by the flow [9, 11]. The zigzag instability has a dominant vertical wavelength of around U/N, which is known as the buoyancy scale [64]. This instability has also been found in other flow configurations including co-rotating vortices [48] and vortex arrays [21]. The breakdown of this dipole into turbulence due to the growth and saturation of the zigzag instability has also been investigated [66, 2, 20]. However, these studies mainly consider dipoles perturbed at the zigzag scale U/N, and do not investigate the growth of smaller vertical scale perturbations. Growth in such small-scale perturbations has been reported in nonlinear simulations [66]. In this work we investigate the linear stability of the dipole at these small vertical scales.

The buoyancy scale is an important length scale in stratified turbulence. It is the vertical scale at which the vertical Froude number is $\mathcal{O}(1)$ [12], and it naturally emerges as the thickness of layers in stratified turbulence [12, 65]. There is a direct transfer of energy, believed to be due to Kelvin-Helmholtz instability [64, 3], from large horizontal scales into the buoyancy scale in stratified turbulence [64] and in the breakdown of the zigzag instability [3]. This breakdown generates small-scale turbulence which ultimately fills the spectrum at scales below the buoyancy scale. But it is possible that primary instabilities of the large-scale vortex may also directly excite vertical scales below the buoyancy scale. We investigate this possibility here.

In this thesis we extend the linear stability analysis of Billant and Chomaz [11] by investigating short, sub-buoyancy scale vertical wavelength perturbations of the Lamb-Chaplygin dipole in a stratified flow. In addition, we further investigate the nonlinear evolution of these sub-buoyancy scales.

The thesis is organised as follows. Chapter 2 and 3 deal with the relevant background on fluid dynamics and numerical methods used. Chapter 4 investigates the linear stability of sub-buoyancy scales. Chapter 5 investigates the nonlinear evolution of the short-wave instability derived through linear theory. Parts of this thesis, including the introduction, linear stability background and results, and conclusions are based on the manuscript Bovard and Waite [13].

Chapter 2

Fluids background

2.1 Boussinesq approximation

The Navier-Stokes equations are the mathematical equations that govern the evolution of fluid flow. In the context of the ocean and atmosphere, the Navier-Stokes equations, along with equations for conservation of mass and energy and an equation of state, provide a good model of the evolution of fluid flow (e.g. Batchelor [6]). For our purposes, however, these equations are too general and an approximation, called the Boussinesq approximation, can be made which results in a simplified version of the Navier-Stokes equations:

$$\frac{\partial \boldsymbol{u}}{\partial t} + \boldsymbol{u} \cdot \nabla \boldsymbol{u} = -\frac{1}{\rho_0} \nabla p - \frac{\rho' g}{\rho_0} \hat{\boldsymbol{e}}_z + \nu \nabla^2 \boldsymbol{u}, \tag{2.1}$$

$$\nabla \cdot \boldsymbol{u} = 0, \tag{2.2}$$

$$\frac{\partial \rho'}{\partial t} + \boldsymbol{u} \cdot \nabla \rho' = \kappa \nabla^2 \rho' - \frac{\partial \bar{\rho}}{\partial z} w, \tag{2.3}$$

where we have the following dimensional variables:

- $\mathbf{u}(x, y, z, t) = (u(x, y, z, t), v(x, y, z, t), w(x, y, z, t))$ is the velocity field in the x, y, z-directions respectively,

- $p(x, y, z, t)$ is the pressure field,

- $\rho(x, y, z, t)$ is the density,

- ρ_0 is a constant reference density,

- $\bar{\rho}(z)$ is a background density profile,

- $\rho'(x, y, z, t) = \rho(x, y, z, t) - \bar{\rho}(z)$ is the perturbation density,

- g is the gravitational constant,

- $\nu = \mu/\rho_0$ is the constant kinematic viscosity,

- μ is the constant dynamic viscosity,

- κ is the constant molecular diffusivity.

Equations (2.1)-(2.3) are a set of five coupled partial differential equations for the unknowns $\mathbf{u}, p, \rho$. Herein, we will refer to equation (2.1) as the velocity or momentum equations, equation (2.2) as the continuity equation, and equation (2.3) as the density equation. An additional useful quantity is the buoyancy frequency or the Brunt-Väisälä frequency which is defined as

$$N^2 = -\frac{g}{\rho_0}\frac{d\bar{\rho}}{dz}. \tag{2.4}$$

Since the background density is assumed to decrease upwards, N^2 is non-negative and N is real. We now assume that N is constant, which implies $\bar{\rho}(z)$ is linear.

A rigorous derivation of the Boussinesq equation is quite delicate and we provide a brief overview of the derivation. A complete derivation, along with many of the subtleties can be found in numerous books such as [6, 32, 58, 60]. The Navier-Stokes equations for a compressible Newtonian fluid can be written as

$$\rho\frac{D\mathbf{u}}{Dt} = -\nabla p - \rho\mathbf{g} + \mu\nabla^2\mathbf{u}, \tag{2.5}$$

$$\frac{1}{\rho}\frac{D\rho}{Dt} + \nabla \cdot \mathbf{u} = 0. \tag{2.6}$$

$$\rho c_p \frac{DT}{Dt} - \alpha T\frac{D\rho}{Dt} = k\nabla^2 T + \phi, \tag{2.7}$$

where $\alpha = -\rho^{-1}(\partial\rho/\partial T)_p$ is the coefficient of thermal expansion, c_p is the specific heat, and ϕ represent conversion of kinetic energy to internal energy by viscous dissipation [63]. To close the system, we need an equation of state, for which a simple approximation for water is [32],

$$\rho = \rho_0(1 - \alpha(T - T_0)). \tag{2.8}$$

The first approximation we make is that of incompressibility. The conditions for incompressibility are [6, 32, 63]

1. Unsteadiness: the time scale of the flow is longer than that of the sound waves.

2. Speed: the characteristic velocity of the flow is much smaller than the speed of sound.

3. Gravity: the vertical scale of the flow is not too large.

Mathematically, letting v denote the speed of sound in the medium, T the characteristic time, u the characteristic velocity, and L_v the characteristic vertical length, these three conditions become [63]

$$\text{unsteadiness: } T^2 \gg L^2/v^2, \tag{2.9}$$

$$\text{speed: } (u/v)^2 \ll 1, \tag{2.10}$$

$$\text{gravity: } L_v \ll v^2/g. \tag{2.11}$$

For the atmosphere, $v \approx 330$ m/s and $g = 9.8$ m/s^2. The speed condition is easily satisfied if $u < 100$ m/s. The gravity condition holds as long as $L \ll 11$ km which implies that the unsteadiness condition holds as long as $T \gg 30$ s. Such conditions are reasonable for shallow motions in the atmosphere. For the ocean $v \approx 1500$ m/s, and thus the speed condition is satisfied if $u \ll 500$ m/s, $L \ll 230$ km, and $T \ll 300$ s. Again, such conditions are satisfied in the ocean. Assuming incompressibility, the conservation of mass equation can be approximated as [32, 63]

$$\frac{1}{\rho}\frac{D\rho}{Dt} + \nabla \cdot \boldsymbol{u} = 0 \Rightarrow \nabla \cdot \boldsymbol{u} = 0. \tag{2.12}$$

The Boussinesq approximation is based on the following decomposition of the density [32, 60]

$$\rho(\boldsymbol{x}, t) = \rho_0 + \bar{\rho}(z) + \rho'(\boldsymbol{x}, t), \tag{2.13}$$

where we assume that $|\rho'| \ll |\bar{\rho}(z)| \ll |\rho_0|$. In other words, variations to the density are small compared to a reference density. Using this approximation, some basic thermodynamics, and the linearity of $\bar{\rho}(z)$, Eq (2.7) simplifies [32, 60] to

$$\frac{DT}{Dt} = \kappa \nabla^2 T. \tag{2.14}$$

Substituting in the equation of state (2.8) and using (2.13) we obtain (2.3).

Consider the first two terms in (2.13). To these background densities, we associate [32, 60] a corresponding background pressure term in hydrostatic balance so that

$$\nabla \bar{p}(z) = -(\rho_0 \mathbf{g} + \bar{\rho}(z)\mathbf{g}). \tag{2.15}$$

Substituting in (2.13) into the momentum equation (2.1) and dividing through by ρ_0 we obtain

$$\left(1 + \frac{\bar{\rho}}{\rho_0} + \frac{\rho'}{\rho_0}\right)\frac{D\mathbf{u}}{Dt} = -\frac{1}{\rho_0}\nabla p - \left(1 + \frac{\bar{\rho}}{\rho_0} + \frac{\rho'}{\rho_0}\right)\mathbf{g} + \nu\nabla^2\mathbf{u}, \tag{2.16}$$

and subtracting (2.15) yields

$$\left(1 + \frac{\bar{\rho}}{\rho_0} + \frac{\rho'}{\rho_0}\right)\frac{D\mathbf{u}}{Dt} = -\frac{1}{\rho_0}\nabla p' - \frac{\rho'}{\rho_0}\mathbf{g} + \nu\nabla^2\mathbf{u}, \tag{2.17}$$

where $p' = p - \bar{p}$. Using $|\rho'| \ll |\bar{\rho}| \ll |\rho_0|$, we can neglect the ratios in front of the material derivative to obtain [32] (2.1). Thus we have derived the Boussinesq equations.

2.2 Linear stability analysis

The study of flow stability has a long and rich history within fluid dynamics. The classic experiment on the stability of fluid flow is that of Reynolds [51]. In this experiment, Reynolds injected dye into the laminar flow through a pipe. By varying the velocity of the flow through the pipe Reynolds observed various effects. If the velocity was sufficiently low, Reynolds was able to observe "a beautiful straight line through the tube" [51]. At slightly higher velocities, the straight line behaviour remained near the initial part of the pipe but further down "the streak would shift about the tube, but there was no appearance of sinuosity" [51]. By increasing the velocity significantly, the dye would again initially remain straight near the initial part of the tube, but instead of shifting about the tube "the colour band would all at once mix up with the surrounding water, and fill the rest of the tube with a mass of coloured water" [51].

What Reynolds observed was the transition and breakdown of a flow into turbulence. Through careful observation, he determined that the dimensionless quantity that governed the behaviour of the flow was the Reynolds number

$$Re = \frac{UL}{\nu}, \tag{2.18}$$

6

a dimensionless number which represents the ratio between the inertial and viscous terms in the Navier-Stokes equations. Reynolds found that if $Re < 13000$ then the flow would remain stable [51].

A natural question to ask is whether we can predict such criteria for any given flow. Ideally, given information about a certain flow, one would be like to be able to determine how the fluid will evolve based on various parameters of the flow, such as viscosity, temperature, or velocity. Unfortunately this task has not been achieved in general and there is no known way to determine such criteria for any arbitrary flow. This is due to the complicated nonlinear behaviour of the Navier-Stokes equations which makes devising a general algorithm for this task incredibly difficult. Tackling this goal in general is immensely difficult and beyond current mathematics, indeed it is not even known whether or not in three dimensions given an initial condition a solution even exists for all times [29].

Thus, to proceed, a simplifying approach must be derived. In order to do this, consider the following idea. Let $(\boldsymbol{u}_0, p)$ denote a basic steady state that solves the Navier-Stokes equations and let $(\boldsymbol{u}', p')$ denote a small unknown perturbation such that $|\boldsymbol{u}', p'| \ll |\boldsymbol{u}_0, p|$. Mathematically this means

$$\boldsymbol{u}(\boldsymbol{x}, t) = \boldsymbol{u}_0(\boldsymbol{x}) + \boldsymbol{u}'(\boldsymbol{x}, t), \qquad p(\boldsymbol{x}, t) = p_0(\boldsymbol{x}, t) + p'(\boldsymbol{x}, t). \tag{2.19}$$

Now let us plug (2.19) into the Navier-Stokes equations and expand, dropping the $(\boldsymbol{x}, t)$ notation,

$$\frac{\partial \boldsymbol{u}_0}{\partial t} + \frac{\partial \boldsymbol{u}'}{\partial t} + (\boldsymbol{u}_0 + \boldsymbol{u}') \cdot \nabla(\boldsymbol{u}_0 + \boldsymbol{u}') = -\frac{1}{\rho_0}\nabla(p_0 + p') + \nu\nabla^2(\boldsymbol{u}_0 + \boldsymbol{u}'), \tag{2.20}$$

$$\nabla \cdot \boldsymbol{u}_0 + \nabla \cdot \boldsymbol{u}' = 0. \tag{2.21}$$

Expanding out the advection term yields

$$(\boldsymbol{u}_0 + \boldsymbol{u}') \cdot \nabla(\boldsymbol{u}_0 + \boldsymbol{u}') = \boldsymbol{u}_0 \cdot \nabla\boldsymbol{u}_0 + \boldsymbol{u}_0 \cdot \nabla\boldsymbol{u}' + \boldsymbol{u}' \cdot \nabla\boldsymbol{u}_0 + \boldsymbol{u}' \cdot \nabla\boldsymbol{u}' \tag{2.22}$$

$$= \boldsymbol{u}_0 \cdot \nabla\boldsymbol{u}_0 + \boldsymbol{u}_0 \cdot \nabla\boldsymbol{u}' + \boldsymbol{u}' \cdot \nabla\boldsymbol{u}_0 + \mathcal{O}(\boldsymbol{u}'^2), \tag{2.23}$$

where we have written the $\boldsymbol{u}' \cdot \nabla\boldsymbol{u}'$ term has $\mathcal{O}(\boldsymbol{u}'^2)$ because this term is of order $\boldsymbol{u}'$ squared, which we assume to be small. Now recall that the basic state has the form $\boldsymbol{u}_0$ solves the Navier-Stokes equations. Thus in (2.20) there are terms that depend just on $\boldsymbol{u}_0$ and they will vanish by definition of it being a solution to the Navier-Stokes equations. Thus we now have that

$$\frac{\partial \boldsymbol{u}'}{\partial t} + \boldsymbol{u}_0 \cdot \nabla\boldsymbol{u}' + \boldsymbol{u}' \cdot \nabla\boldsymbol{u}_0 + \mathcal{O}(\boldsymbol{u}'^2) = -\frac{1}{\rho_0}\nabla p' + \nu\nabla^2\boldsymbol{u}', \tag{2.24}$$

$$\nabla \cdot \boldsymbol{u}' = 0. \tag{2.25}$$

So far, the above equations are exact and we have just rewritten the quadratic nonlinear term in the Big-O notation. The critical assumption we make is that the magnitude of the perturbation, $|\boldsymbol{u}'|$, is small compared to the basic state, $|\boldsymbol{u}_0|$, i.e. $|\boldsymbol{u}'| \ll |\boldsymbol{u}_0|$. In other words, we are neglecting the quadratic nonlinearity because the perturbation is small.

Now making the approximation that $\mathcal{O}(\boldsymbol{u}'^2)$ is small we obtain

$$\frac{\partial \boldsymbol{u}'}{\partial t} + \boldsymbol{u}_0 \cdot \nabla \boldsymbol{u}' + \boldsymbol{u}' \cdot \nabla \boldsymbol{u}_0 = -\frac{1}{\rho_0} \nabla p' + \nu \nabla^2 \boldsymbol{u}', \tag{2.26}$$

$$\nabla \cdot \boldsymbol{u}' = 0. \tag{2.27}$$

The above set of equations is linear which means they are more amenable to analytical and numerical techniques.

To illustrate the usefulness in this approach, we present an example of linear stability and apply the method to the problem of plane parallel shear flow. This is a standard example and we follow the derivation of [22]. It will also elucidate the key features of linear stability analysis that we will use throughout this thesis.

The first simplifying assumption we make is that the basic state $\boldsymbol{u}_0 = U(z)\hat{\boldsymbol{e}}_x$, a parallel shear flow, which simplifies the above equations to

$$\frac{\partial \boldsymbol{u}'}{\partial t} + U\frac{\partial \boldsymbol{u}}{\partial x} + w'\frac{dU}{dz}\hat{\boldsymbol{e}}_x = -\frac{1}{\rho_0}\nabla p' + \nu\nabla^2 \boldsymbol{u}', \tag{2.28}$$

$$\nabla \cdot \boldsymbol{u}' = 0. \tag{2.29}$$

If we had considered the Euler equations instead of the Navier-Stokes equations, we would have the same equations as above except with $\nu = 0$. Despite this seemingly simple modification, the resulting equation is very different. When the inviscid equations are considered, there are many elegant results about the stability of the flow that can be derived for the special case of parallel shear flow. For example, the Rayleigh's inflection point theorem states that a necessary condition for instability is that the basic velocity profile should have an inflection point [22]. Unfortunately, many of the results for inviscid flow theory do not hold for viscous flow theory. A complete discussion of this result and its generalisation, among other theorems, can be found in [22, 32].

Since the resulting set of equations is a set of coupled linear equations, the solution set involves complex exponentials. Thus, the next natural step is to expand the solution as Fourier modes

$$\boldsymbol{u}'(\boldsymbol{x}, t) = \hat{\boldsymbol{u}}(z)e^{i(\alpha x + \beta y - \alpha c t)}, \tag{2.30}$$

$$p'(\boldsymbol{x}, t) = \hat{p}(z)e^{i(\alpha x + \beta y - \alpha c t)}, \tag{2.31}$$

8

where we take the real part of the above solutions. We require that the solution remains bounded as $x, y \to \pm\infty$ which means that α, β must remain real. For c, however, we let it remain an arbitrary complex number $c = c_r + ic_i$. Depending on the sign of c_i the result will either decay or grown exponentially as time goes to infinity. We thus associate stability with $c_i \leq 0$ and instability with $c_i > 0$. Hence, if we are able to solve the above system for c_i as a function of the parameters we will be able to derive some criteria for the stability of the flow.

Substituting in the above Fourier expansions into the linear equations would yield an eigenvalue problem with c being the undetermined eigenvalue as a function of α, β, Re. Then, we can apply methods from numerical linear algebra to solve for c for various Re, α, β and obtain a stability curve for c. However, a result due to Squire allows us to simplify the problem significantly. Squire's theorem states that to obtain the minimum critical Reynolds number it is sufficient to consider only two-dimensional disturbances [22]. In other words, for every three dimensional mode, there is a more unstable two dimensional eigenmode. A proof is provided in [22]. Because we only need to consider two-dimensional flow, the unknown velocity $\boldsymbol{u}'$ can be rewritten in terms of the stream function $\psi'(x, z, t)$.

Expanding ψ' as a complex exponential and denoting ϕ as the amplitude of the stream function and $D = d/dz$, the linear equations can be re-written as a single equation,

$$(D^2 - \alpha^2)^2 \phi = (i\alpha Re)(U - c)(D^2 - \alpha^2)\phi - (i\alpha Re)U''\phi, \qquad (2.32)$$

along with the appropriate boundary conditions. This equation is known as the Orr-Sommerfeld equation and has a rich history in the development of fluid mechanics. A comprehensive discussion of the various methods of solving this equation and others like it using techniques such as WKB theory, asymptotics, and perturbation theory, is contained in [22, 61, 7].

This simple derivation has resulted in a single equation with three parameters α, c, Re and by choosing different Re and α, we can determine a criteria for c. Although much work has been done at the beginning of the 20th century to derive approximate solutions to the Orr-Sommerfeld equation, numerically it is very easy to solve. We can reformulate the above equation as a generalised eigenvalue problem for a given parallel shear flow and solve the problem rather easily on a computer [56].

Linear stability is a useful technique for determining whether or not a given flow is stable, however it is important to not forget the underlying assumptions. Since we are explicitly assuming that $|\boldsymbol{u}'| \ll |\boldsymbol{u}_0|$ the resulting linear equations are only valid when this is the case. As we shall see in numerical simulations, this assumption is not necessarily valid at all times.

Additionally, depending on whether we or not we ignore viscosity, energy may or may not be conserved. However, in both cases, in the absence of external forcing, the energy will always remain bounded since energy is not being pumped into the system. However we have stated that if $c_i > 0$ then we have exponential growth. Clearly, as time advances, this energy grows very quickly which implies that the perturbation will grow unbounded. This seems to violate conservation of energy, since the total amount of energy of the perturbation is growing, and violates the assumption that the perturbation is small.

The reason this occurs in linear stability analysis is simple: we implicitly assume that the basic state remains undisturbed, i.e. that the perturbations are small enough so they do not change the basic state. This means, when running a numerical simulation, the perturbation is able to grow in time while the basic state remains unchanged. Thus we can think of the basic state as continuously pumping in energy into the perturbation state, allowing it to grow unbounded. Physically, this is not the case. In a full nonlinear simulation, the basic state does not remain unchanged and as the perturbation begins to grow, the basic state loses energy and changes and eventually reaches a point where we can no longer assume the perturbation is small compared to the basic state. Thus we have a breakdown of the linear theory and would need to turn to a nonlinear theory to continue our modeling.

However, linear stability still provides useful information. Even though the individual eigenmodes grow exponentially, which eigenmodes are growing gives insight into what mechanisms are causing the growth. As we shall see, linear stability theory tells us what length scales dominate in the transition to turbulence in a stratified fluid. Given this information, it is possible to assume a certain scaling of the full nonlinear equations that can provide us with a potential simplified model to study the problem of turbulence in stratified fluids.

So far, we have considered the Navier-Stokes equations directly instead of the simpler Euler equations. Recall the Euler equations arise by setting the viscosity to 0 or letting the Reynolds number go to infinity. The Euler equations also have some other nicer features, such as explicit conservation of energy which might provide a useful potential invariant that we can exploit in the study of stability and turbulence.

To motivate the possible use of the Euler equations, consider the observation that turbulence is very often observed at a high Reynolds number. In the atmosphere for example, the Reynolds number is on the order of $10^8 - 10^9$ or higher. Since the inverse of the Reynolds number appears in front of the diffusion term, it seems reasonable to instead ignore the diffusion term since the coefficient is $\mathcal{O}(Re^{-1}) \ll 1, Re \gg 1$. This would be a mistake. This is because the limit $Re \to \infty$ is a singular limit. Consider the following

simplified model which arises in the study of boundary layers of shear bounded wall flow [1, 7, 32] (even though our work does not involve boundaries directly, it cleanly illustrated the problems with setting $\nu = 0$ in our equations and trying to draw conclusions from the resulting equations):

$$\epsilon y'' - y = 0, \qquad y(0) = 0, \qquad y(1) = 1. \tag{2.33}$$

Suppose that we are interested in the limiting behaviour of $\epsilon \to 0$. If we set $\epsilon = 0$ the problem would become

$$-y = 0, \qquad y(0) = 0, \qquad y(1) = 1. \tag{2.34}$$

which has the solution $y = 0$ which only satisfies one of the boundary conditions. If we tried a perturbation expansion of the form $y(x) = \sum_{n=0} y_n(x)\epsilon^n$ we would get nowhere because the lowest order term does not exist. If we solve the full equation we obtain

$$y(x) = \frac{e^{x/\epsilon} - 1}{e^{1/\epsilon} - 1}. \tag{2.35}$$

In this equation, we cannot set $\epsilon = 0$ because that results in a singular limit. Thus regardless of how small we choose ϵ, there will be a thin layer, called the boundary layer, which is essential to the fluid flow. For a discussion of techniques in singular perturbation theory in terms of the linear stability of the Navier-Stokes equations see [22, 61]. Hence, even though it seems reasonable to neglect the diffusion term to study instability and turbulence, it is not as promising an avenue as one might first expect. In one sense, this singular limit of the Navier-Stokes equations contributes to making turbulence a very difficult problem to investigate analytically and numerically.

Finally, the experimental investigation into instability of fluids and the transition to turbulence produces very appealing images which really illustrate the beauty of fluid dynamics and the reader is recommended to peruse the coffee table book by Van Dyke [62] which illustrates many images from experiments of the classical results in stability theory.

2.3 The zigzag instability

2.3.1 A brief history of vortex instabilities

The origin of the study of vortex instabilities begins with Lord Kelvin who in 1880 studied perturbations to columnar vortices and determined that they were stable. For the next 90

years, the theory of vortex instability remained relatively quiet until the field was re-ignited by the investigations of Crow [19]. Motivated by aeronautical engineering applications, he discovered that for long wavelength perturbations of a pair of counter-rotating vortices that there was a symmetric deformation of the vortices. This work was extended a few years later by Widnall et al. [70] to small wavelength perturbations. Further investigations into small wavelength perturbations were carried out by numerous others e.g. [24, 59]. It was noticed in these studies that the streamlines of the vortex became elliptical when perturbed. Motivated by this, Pierrehumbert [49] investigated the simple case of a single two-dimensional (2D) elliptical vortex subject to a three-dimensional (3D) perturbation. Extensions to this elliptical model were done by Bayly [4] and Waleffe [68] and led to this instability being called the elliptical instability. A complete and detailed history of the elliptical instability, including derivations and results of the above papers and nonlinear investigations, is presented in the review by Kerswell [30]. Most of the investigations into the elliptical instability were concerned with unstratified flow, but an investigation by Miyazaki and Fukumoto [43] showed with a sufficiently strong stratification, the elliptical instability is suppressed. The effects of weak stratification, which we do not considere here, has been studied in the context of Kelvin-Helmholtz billows (e.g. Potylitsin and Peltier [50]).

2.3.2 Discovery of the zigzag instability

Experimental studies on the elliptical instability by Leweke and Williamson [35] led Billant, Brancher, and Chomaz [8] to investigate the stability of a three dimensional vortex pair numerically. As we shall show below, their basic state provides a good model for the vortices generated in the experiment. Initially this work was unstratified and confirmed the existence of the elliptical instability. However, following up this work, Billant and Chomaz added in the effects of stratification and discovered a new type of instability at small scales that was distinct from the elliptical instability. They labeled this new instability the "zigzag instability" due to its zigzag-like structure, as we shall see below. In a series of three papers they investigated experimentally [9], theoretically [10], and numerically [11] the evolution of a pair of columnar vortices in a stratified tank.

First Billant and Chomaz investigated the zigzag instability experimentally [9]. To do this, they investigated a columnar vortex pair created by a pair of flaps in a tank of stratified fluid. We now briefly discuss their experimental procedure since it provides important motivation for the resulting numerical study.

In order to study the effects of stratification on the evolution of vortices, they first needed to create the vortices. To do this, they used a pair of motor-controlled flaps whose

initial angle and closing time could be controlled precisely by a computer. When the flaps were closed, a pair of counter-rotating vortices was produced. They found that the important determining factor in the creation of the vortices was the initial angle of the flaps. If the angle was too small, additional vortices created when the flaps finally stopped closing were being advected by the dipole and causing spurious instability. For large angles, fluid that was initially in-between the flaps was being injected in the flow and again causing spurious oscillations. In order to balance out these effects, an angle of 14° was chosen. Additionally, to enforce the emergence of the zigzag instability, tape was applied to the flaps in order to force certain wavenumbers of the evolving flow (see Fig. 8 of [9] for the importance of forcing).

After fixing the separation angle they found that by varying the closing time of the flaps, the velocity of the pair of vortices could be changed. Interestingly, the decay of the vortices, was roughly 90s, was independent of the closing time of the flaps. This variation in the velocity determined the experimental parameters for the experiment.

The two important dimensional parameters in this experiment were the horizontal Froude number

$$F_h = \frac{U}{NR}, \tag{2.36}$$

and the Reynolds numbers

$$Re = \frac{UR}{\nu}, \tag{2.37}$$

where U is the propagating velocity of the dipole as above, R is the radius of the dipole, ν is the viscosity of the tank, and N is the buoyancy frequency. Here the viscosity ν and the radius R were fixed by experimental conditions and could not be varied. Thus the only parameters that could be varied were N and U. Since the buoyancy frequency was more difficult to vary, as changing it required draining and refilling the tank, only four stratifications were considered ranging from $N = 1.26$ rad s^{-1} to $N = 1.97$ rad s^{-1}. Thus the parameter that was easiest to control was the initial velocity U. Because U shows up in both dimensionless numbers, changing U resulted in the changing of both numbers, i.e. they are directly related by the following relationship

$$Re = F_h \frac{NR^2}{\nu}, \tag{2.38}$$

and for the given stratification numbers the range of Froude numbers was between $0.10 - 0.23$ and for the Reynolds number was $200 - 450$.

To derive a theoretical model of the dipole, they computed the Fourier transform of the measured vorticity in order to determine the stream function. They found that there was a linear fit between the vorticity ω and the stream function ψ such that $\omega = k^2\psi$ where $k^2 = 1.15\text{cm}^{-2}$ which, as we will show below, corresponds to a columnar Lamb-Chaplygin dipole.

Figure 10 of [9] demonstrates the evolution for the zigzag instability for $F_h = 0.19$ and $Re = 365$. The structure of the vortices displays a zigzag like structure. Additionally, the anisotropy between the vertical and horizontal directions is quite clear. The behaviour of the vertical structure of the vortex pair is also evident.

Following up the experimental work, Billant and Chomaz provided a theoretical account of the zigzag instability starting from the Boussinesq equations [10]. We will only discuss the main result of their paper, which is a long technical perturbation analysis of the Boussinesq equations. In the paper, they investigated the limit where $F_{h,v} = U/L_{h,v}N \ll 1$ and found that the zigzag motion was accounted for by combination of translation and rotation, which agrees with the experimental observations of [9]. Additionally, they found that the most unstable vertical length scale of the zigzag instability should behave as $F_v \sim \mathcal{O}(1)$, i.e. $L_v \sim U/N$. This length is known as the buoyancy length scale (e.g. Waite [64]) and has proven to be a very important length scale in stratified fluid flow, as we shall discuss below. This emergence of the buoyancy length scale in their calculations, however, should be treated with some care since Billant and Chomaz assumed that $F_v \ll 1$ and showed that $F_v \sim \mathcal{O}(1)$.

In the third paper, Billant and Chomaz conducted a numerical linear stability analysis of the zigzag instability [11]. In this study, they numerically solved the linear Boussinesq equations for the growth rate of the leading eigenmode for specific wavenumbers. We will not discuss the results of the paper here as their paper forms the basis for much of this thesis and we will re-derive and discuss their results throughout the next three chapters. In the remainder of this chapter we derive the numerical equations that Billant and Chomaz used in [11] and provide some more background information. In Chapter 3 we introduce and discuss the numerical technique of spectral methods used to solve the numerical equations. In Chapter 4 we extend the analysis of Billant and Chomaz to length scales well below the sub-buoyancy scale of $L_b \sim U/N$.

2.4 Formulation of the linear problem

Following Billant and Chomaz [11], we consider the non-dimensional Boussinesq approximation to the Navier-Stokes equations in Cartesian co-ordinates

$$\frac{D\boldsymbol{u}}{Dt} = -\nabla p - \rho'\hat{\boldsymbol{e}}_z + \frac{1}{Re}\nabla^2\boldsymbol{u}, \qquad (2.39)$$

$$\nabla \cdot \boldsymbol{u} = 0, \qquad (2.40)$$

$$\frac{D\rho'}{Dt} - \frac{w}{F_h^2} = \frac{1}{ReSc}\nabla^2\rho', \qquad (2.41)$$

where we have non-dimensionalised by the characteristic velocity U, length R, time-scale R/U, pressure $\rho_0 U^2$, density $\rho_0 U^2/gR$, and defined $Sc = \nu/\kappa$ as the Schmidt number, where κ is the molecular diffusivity, ρ_0 is the background density, and g is the gravitational constant. The Reynolds and horizontal Froude number are as defined above. The buoyancy frequency N, and hence the Froude number F_h, is assumed to be constant.

In order to investigate the linear growth rate, we proceed as in Section 1.2 and expand the full velocity field as the sum of a basic state and a perturbation state:

$$\boldsymbol{u} = \boldsymbol{u}_0 + \tilde{\boldsymbol{u}}, \qquad (2.42)$$

$$p = p_0 + \tilde{p}, \qquad (2.43)$$

$$\rho' = \rho'_0 + \tilde{\rho}'. \qquad (2.44)$$

The basic is chosen to be the Lamb-Chaplygin dipole which we will now discuss and explain how it provides a convenient theoretical model for the experiment by Billant and Chomaz [9].

2.4.1 The Lamb-Chaplygin dipole

As the basic state for linear stability analysis we use the Lamb-Chaplygin dipole in a comoving frame [40]. This dipole is a solution to the 2D inviscid Euler equations. This basic state is motivated by numerous laboratory experiments [9, 35], as discussed above, which demonstrated that a vertically oriented Lamb-Chaplygin dipole is a good approximation to the vortex generated by two flaps closing in a tank of salt-stratified water. The dipole,
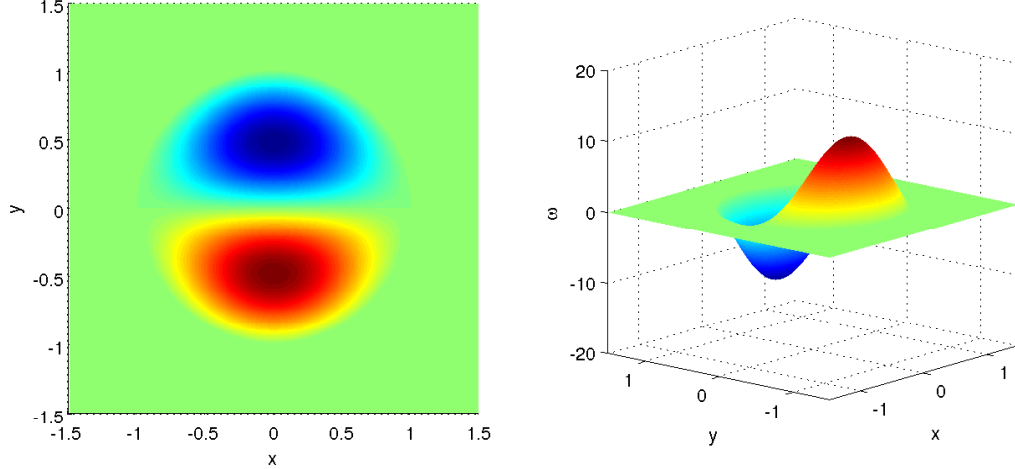
Figure 2.1: The vertical vorticity ω_z of the Lamb-Chaplygin dipole.

in cylindrical coordinates, is given by the stream function

$$\psi_0(r,\theta) = \begin{cases} -\dfrac{2}{\mu_1 J_0(\mu_1)} J_1(\mu_1 r) \sin\theta & r \leq 1, \\[2ex] -r\left(1 - \dfrac{1}{r^2}\right) \sin\theta & r > 1, \end{cases} \tag{2.45}$$

and the corresponding vertical vorticity $\omega_{z0} = \nabla_h^2 \psi_0$

$$\omega_{z0}(r,\theta) = \begin{cases} \mu_1^2 \psi_0(r,\theta) & r \leq 1, \\ 0 & r > 1, \end{cases} \tag{2.46}$$

where J_0, J_1 are the zero and first order Bessel functions, $\mu_1 \approx 3.8317$ is the first root of J_1, and ∇_h is the horizontal Laplacian. The basic state velocity is purely horizontal and is given by $\boldsymbol{u}_{h0} = \nabla_h \psi_0 \times \hat{\boldsymbol{e}}_z$. Recall from the previous section, Billant and Chomaz found experimentally that $\omega = k^2 \psi$ where $k = 1.15$. Here we have that $\omega_{z0} = \mu_1^2 \psi_0$. If we consider the dimensional version, we would have that $k^2 = \mu_1^2/R^2$ where $R = 3.6$ cm. This gives $k^2 = 1.13$ cm^{-2} which corresponds very well with the experimental value of 1.15. Fig. 2.1 is a plot of the vorticity.

Let us now discuss the derivation of this result, which was first written down by Lamb and investigated further, independently, by Chaplygin [40]. Although Lamb was the first to

16

write down the above solution to the Euler equations, he did not provide any motivation for the derivation beyond it being an exact solution of the 2D steady Euler equations. However, a decade later, Lamb provided a slightly more in depth derivation motivating somewhat the study of this dipole. Independently, in Russia, Chaplygin provided a complete derivation and motivation for studying this dipole, although it remained unknown outside of Russia until the 1980s[40]. Following [40] we repeat the key points of Chaplygin's argument.

Recall that the steady 2D Euler equations can be written in terms of the stream function ψ and a vorticity ω, where

$$\nabla^2 \psi = -\omega. \tag{2.47}$$

To choose ω, Chaplygin was motivated by the situation where we have a continuous vortex whose outer region is steady irrotational flow while the cylindrical inner region is a translating vortex. Recall that the potential function for irrotational flow outside a cylinder is

$$\psi = v_0 \left(r - \frac{a^2}{r} \right) \sin \theta, \tag{2.48}$$

where a is the radius of the dipole and v_0 is the propagation velocity.

Inside the radius a, Chaplygin chose the vorticity to be $\omega = n^2 \psi$ where n is a constant. In polar coordinates (2.47) becomes the following boundary value problem

$$\frac{\partial^2 \psi}{\partial r^2} + \frac{1}{r} \frac{\partial \psi}{\partial r} + \frac{1}{r^2} \frac{\partial^2 \psi}{\partial \theta^2} = n^2 \psi, \tag{2.49}$$

which we can guess has a solution of the form $\psi(r, \theta) = Z(r) \sin \theta$. Although Chaplygin did not provide specific motivation for choosing this specific vorticity, the above equation has a form that is similar to the irrotational flow outside the dipole and this makes the matching conditions simple. The resulting equation for $Z(r)$ is the well known Bessel equation [40] and after working through the algebra, one obtains (2.45). Chaplygin also investigated the resulting pressure field produced by the dipole and was able to compute the circulation of the dipole [40]. Unlike Lamb, he also considered a generalisation of the above where the dipole is no longer symmetric about the x-axis. The corresponding vorticity in this case is given by

$$\omega = n^2 (\psi - \lambda), \tag{2.50}$$

where λ is an arbitrary parameter where $\lambda = 0$ is a completely symmetric dipole and $\lambda \to \infty$ corresponds to a completely asymmetric dipole. Here, again, Chaplygin investigated fully the pressure and circulation produced by this dipole. Additionally, in the same set of papers, Chaplygin also investigated the case of the dipole in a rotating fluid, which was independently rediscovered 80 years later. Full details of this derivation are in [40].

17

2.5 Scaling analysis

We have mentioned two dimensionless numbers in stratified flows, the Reynolds number and the Froude number. Both these dimensionless numbers arise when comparing the relative sizes of various terms in the Navier-Stokes equations. Depending on what aspect of a problem we are looking at, these numbers can appear in different places when we choose different scalings. We will now discuss some of the scaling arguments that have been used in stratified flow as it can provide insights into what mechanisms underlie the transition to and evolution of turbulence. A comprehensive review of scaling in stratified turbulence is provided in a recent review by Riley and Lindborg [54] and we will discuss the important scaling arguments therein.

For reference, we reproduce the Boussinesq equations here

$$\frac{\partial \mathbf{u}_h'}{\partial t'} + \mathbf{u}_h' \cdot \nabla_h' \mathbf{u}_h' + u_z' \frac{\partial \mathbf{u}_h'}{\partial z'} = -\frac{1}{\rho_0}\nabla_h' p' + \nu\nabla'^2 \mathbf{u}_h, \tag{2.51}$$

$$\frac{\partial u_z'}{\partial t'} + \mathbf{u}_h' \cdot \nabla_h' u_z' + u_z' \frac{\partial u_z'}{\partial z'} = -\frac{1}{\rho_0}\frac{\partial p'}{\partial z'} - \frac{\rho' g}{\rho_0} + \nu\nabla'^2 u_z, \tag{2.52}$$

$$\nabla_h' \cdot \mathbf{u}_h' + \frac{\partial u_z'}{\partial z'} = 0, \tag{2.53}$$

$$\frac{\partial \rho'}{\partial t'} + \mathbf{u}_h' \cdot \nabla_h' \rho' + u_z' \frac{\partial \rho'}{\partial z'} = \kappa\nabla^2 \rho', \tag{2.54}$$

where the primed quantities denote the dimensional quantities.

As a starting point, we produce a scaling argument that separates the horizontal and vertical directions. As we saw in the experiment of Billant and Chomaz [9], in the zigzag instability there was a clear separation between the vertical and horizontal scales. This difference in the vertical and horizontal directions suggests defining two length scales, the horizontal length scale L_h and the vertical length scale L_v. Associated with this separation we introduce the horizontal velocity scale U and the vertical velocity scale W. The resulting scaling is

$$x' = L_h x, \qquad y' = L_h y, \qquad z' = L_v z, \qquad \mathbf{u}_h' = U\mathbf{u}, \qquad u_z' = W u_z. \tag{2.55}$$

We also define another useful quantity that plays an important role in the scaling of stratified flows, the aspect ratio

$$\delta = \frac{L_v}{L_h}, \tag{2.56}$$

which measures how anisotropic the length scales are. For the time scale, we choose the advective time scale

$$t' = \frac{L_h}{U} t, \tag{2.57}$$

which is the characteristic time of a vortex to be advected around the characteristic length [53, 12, 37]. Following these references the pressure scales such that the horizontal pressure gradient is the same order as the advection terms and density scales from approximate hydrostatic balance

$$p' = \rho_0 U^2 p, \qquad \rho' = \frac{U^2 \rho_0}{g L_v} \rho. \tag{2.58}$$

The only quantity left unspecified is the vertical velocity which can be determined by balancing the linear terms and the time derivative terms in the density equation [12, 53] giving the scaling

$$u'_z = U \frac{F_h^2}{\delta} u_z. \tag{2.59}$$

This scaling now leads to the following set of equations [54]

$$\frac{\partial \mathbf{u}_h}{\partial t} + \mathbf{u}_h \cdot \nabla_h \mathbf{u}_h + \frac{F_h^2}{\delta^2} u_z \frac{\partial \mathbf{u}_h}{\partial z} = -\nabla_h p + \frac{1}{Re} \left(\nabla_h^2 \mathbf{u}_h + \frac{1}{\delta^2} \frac{\partial^2 \mathbf{u}_h}{\partial z^2} \right), \tag{2.60}$$

$$F_h^2 \left(\frac{\partial u_z}{\partial t} + \mathbf{u}_h \cdot \nabla_h u_z + \frac{F_h^2}{\delta^2} u_z \frac{\partial u_z}{\partial z} \right) = -\frac{\partial p}{\partial z} - \rho + \frac{F_h^2}{Re} \left(\frac{1}{\delta^2} \frac{\partial u_z}{\partial z^2} + \nabla_h^2 u_z \right), \tag{2.61}$$

$$\nabla_h \cdot \mathbf{u}_h + \frac{F_h^2}{\delta^2} \frac{\partial u_z}{\partial z} = 0, \tag{2.62}$$

$$\frac{\partial \rho}{\partial t} + \mathbf{u}_h \cdot \nabla_h \rho + \frac{F_h^2}{\delta^2} u_z \frac{\partial \rho}{\partial z} = \frac{1}{ReSc} \left(\frac{1}{\delta^2} \frac{\partial^2 \rho}{\partial z^2} + \nabla_h^2 \rho \right), \tag{2.63}$$

where

$$Re = \frac{U L_h}{\nu}, \qquad F_h = \frac{U}{L_h N}, \qquad Sc = \frac{\nu}{\kappa}. \tag{2.64}$$

Lilly was the first to write these equations down although he assumed isotropy, i.e. $\delta = 1$.

Let us now investigate the limit of strong stratification, i.e. $F_h \to 0$ but let us leave the behaviour of F_h/δ undetermined. Additionally, let us consider $Re \gg 1$ and following [54]

ignore the diffusion terms that only depend on Re while keeping those with $Re\delta^2$. This results in the following equations

$$\frac{\partial \mathbf{u}_h}{\partial t} + \mathbf{u}_h \cdot \nabla_h \mathbf{u}_h + \frac{F_h^2}{\delta^2} u_z \frac{\partial \mathbf{u}_h}{\partial z} = -\nabla_h p + \frac{1}{Re} \frac{1}{\delta^2} \frac{\partial^2 \mathbf{u}_h}{\partial z^2}, \tag{2.65}$$

$$0 = -\frac{\partial p}{\partial z} - \rho, \tag{2.66}$$

$$\nabla_h \cdot \mathbf{u}_h + \frac{F_h^2}{\delta^2} \frac{\partial u_z}{\partial z} = 0, \tag{2.67}$$

$$\frac{\partial \rho}{\partial t} + \mathbf{u}_h \cdot \nabla_h \rho + \frac{F_h^2}{\delta^2} u_z \frac{\partial \rho}{\partial z} = \frac{1}{ReSc} \frac{1}{\delta^2} \frac{\partial^2 \rho}{\partial z^2}. \tag{2.68}$$

It was initially assumed by Lilly [37] and Riley et al.[53] that as $F_h \to 0$ then so does F_h/δ. Thus the resulting equations are

$$\frac{\partial \mathbf{u}_h}{\partial t} + \mathbf{u}_h \cdot \nabla_h \mathbf{u}_h = -\nabla_h p + \frac{1}{Re} \frac{1}{\delta^2} \frac{\partial^2 \mathbf{u}_h}{\partial z^2}, \tag{2.69}$$

$$0 = -\frac{\partial p}{\partial z} - \rho, \tag{2.70}$$

$$\nabla_h \cdot \mathbf{u}_h = 0, \tag{2.71}$$

$$\frac{\partial \rho}{\partial t} + \mathbf{u}_h \cdot \nabla_h \rho = \frac{1}{ReSc} \frac{1}{\delta^2} \frac{\partial^2 \rho}{\partial z^2}. \tag{2.72}$$

Notice that in these resulting equations, the horizontal and vertical velocity equations have become almost completely decoupled. They are not completely decoupled because there is still dependence through the pressure term. However this decoupling led Lilly to conjecture that stratified turbulence in the strong stratification limit will resemble layerwise 2D turbulence with an inverse energy cascade [37]. However, subsequent numerical simulations of stratified turbulence were not able to reproduce an inverse cascade, raising doubts about the applicability of Lilly's equations (e.g. Herring and Metais [41], Waite and Bartello [65]).

Building on the work of Lilly [37] and Riley et al.[53], Billant and Chomaz [12] modified the argument suggesting that instead $F_h/\delta \to 1$, not 0, as $F_h \to 1$. This scaling analysis leads to $L_v \sim U/N$ which is the dominant vertical scale for the zigzag instability. The resulting equations are

$$\frac{\partial \mathbf{u}_h}{\partial t} + \mathbf{u}_h \cdot \nabla_h \mathbf{u}_h + u_z \frac{\partial \mathbf{u}_h}{\partial z} = -\nabla_h p + \frac{1}{Re}\frac{1}{\delta^2}\frac{\partial^2 \mathbf{u}_h}{\partial z^2}, \tag{2.73}$$

$$0 = -\frac{\partial p}{\partial z} - \rho, \tag{2.74}$$

$$\nabla_h \cdot \mathbf{u}_h + \frac{\partial u_z}{\partial z} = 0, \tag{2.75}$$

$$\frac{\partial \rho}{\partial t} + \mathbf{u}_h \cdot \nabla_h \rho + u_z \frac{\partial \rho}{\partial z} = \frac{1}{ReSc}\frac{1}{\delta^2}\frac{\partial^2 \rho}{\partial z^2}. \tag{2.76}$$

The assumption that $F_h/\delta \to 1$ can be rewritten to state that $L_v \sim U/N$, which is the buoyancy scale. In this case, there is no decoupling between the horizontal and vertical directions and the advection terms and incompressibility condition are fully three-dimensional.

Chapter 3

Numerical background

In this chapter we discuss the numerical techniques and methods used in this thesis. In this thesis we use the spectral method to numerically solve the linear and nonlinear Navier-Stokes equations. Fourier-based spectral methods provide a convenient and quick way to compute derivatives of sufficiently well-behaved periodic functions. In evaluating derivatives of smooth periodic functions, spectral methods provide an advantage over other methods of evaluating derivatives, such as finite difference, as the derivatives can be computed with greater accuracy, in exchange for only a relatively modest increase in complexity. Specifically, finite difference methods run in $\mathcal{O}(N)$ time, where N is the number of grid points, but the error tends to be on the order of $\mathcal{O}(N^{-p})$ where p is a small integer [23]. Spectral methods, however, run in $\mathcal{O}(N \log N)$ time but the errors are on the order of $\mathcal{O}(N^{-p})$ when the function is C^p [56]. A complete overview of spectral methods is beyond the scope of this thesis and we only discuss the key features needed for numerical work. Comprehensive reviews of spectral methods are provided in many books, e.g. Trefethen [56], Boyd [14], and Canuto [16].

3.1 Spectral methods motivation

Spectral methods have their origins in the Fourier transform. Let us denote the Fourier transform, $\mathcal{F}$, of $f(x)$ as $\mathcal{F}(f(x)) = \hat{f}(k)$, given by

$$\mathcal{F}(f(x)) = \hat{f}(k) = \int_{-\infty}^{\infty} dx \, e^{-ikx} f(x). \tag{3.1}$$

Now consider the Fourier transform of the derivative df/dx:

$$\mathcal{F}\left(\frac{df}{dx}\right) = \int_{-\infty}^{\infty} dx e^{-ikx} \frac{df}{dx} = e^{-ikx} f(x)\Big|_{-\infty}^{\infty} + ik \int_{-\infty}^{\infty} dx e^{-ikx} f(x) = ik\hat{f}(k), \qquad (3.2)$$

and thus the Fourier transform of a derivative is just ik times the Fourier transform of $f(x)$. An important assumption here that $f(x)$ vanishes sufficiently quickly at infinity otherwise the $e^{-ikx} f(x)$ term is non-negligible. For most applications of the Fourier transform, but not all, this assumption is valid. For a complete treatment of the conditions of the existence of the Fourier transform, see e.g. Kammler [31]. With this result in hand, it is easy to show via induction that the Fourier transform of $d^n f/dx^n$ is $(ik)^n \hat{f}(k)$. Hence, once we have the Fourier transform $\hat{f}(k)$, the n-th derivative is obtained by computing the inverse Fourier transform

$$\frac{d^n f}{dx^n} = \frac{1}{2\pi} \int_{-\infty}^{\infty} dx e^{ikx} (ik)^n \hat{f}(k). \qquad (3.3)$$

This procedure suggests a method to compute the derivative of a function. Computationally, if we have a way to evaluate $\hat{f}(k)$ from $f(x)$ and $f(x)$ from $\hat{f}(k)$, then the n-th derivative is easy to compute via the following algorithm:

1. Compute $\hat{f}(k)$ from $f(x)$

2. Multiply $\hat{f}(k)$ by $(ik)^n$

3. Invert $(ik)^n \hat{f}(k)$ to obtain $f^{(n)}(x)$

We need a method to evaluate the integrals (3.1) and (3.3). One possible avenue would be to apply well known integral quadratures to evaluate these integrals. However, there are more efficient and better alternatives. The correct avenue to implementing the above algorithm is to consider the discrete analogue of the Fourier transform, the discrete Fourier transform. From the discrete Fourier transform, we discuss the Fast Fourier Transform, which is a fast way to evaluate the discrete Fourier transform.

3.2   FFT and spectral derivatives

Let us now investigate how we can quickly compute the Fourier transform of a function on a computer. In analogy to the Fourier transform, we define [56] the discrete Fourier

transform[1] (DFT) on N data points v_j

$$\hat{v}_k = \frac{2\pi}{N} \sum_{j=1}^{N} e^{-ikx_j} v_j, \qquad k = -\frac{N}{2} + 1, \ldots, \frac{N}{2}, \tag{3.4}$$

and the inverse discrete Fourier transform (IDFT) on N data points $\hat{v}_k$

$$v_j = \frac{1}{2\pi} \sum_{k=-N/2+1}^{N/2} e^{ikx_j} \hat{v}_k, \qquad j = 1, \ldots, N. \tag{3.5}$$

where $x_j \in [0, 2\pi]$. Here we take N to be even to simplify the formulas, however all results hold for odd N with slight modification. The range of the wavenumbers is from $-N/2+1$, not $-N/2$, due to the 2π periodicity of v_j. Wavenumbers $-N/2$ are equivalent to $N/2$ and we do not want to count this wavenumber twice.

From the definitions of the DFT and inverse DFT, we can see a close analogy to the continuous Fourier and inverse Fourier transforms. It can be shown [56] that these are the correct discrete analogies.

In order to approximate the derivative of a function, we first need to determine how to sample the function $f(x)$. We assume $f(x)$ to periodic on $0 \leq x \leq 2\pi$. If the domain is different, a simple scaling can transform the periodic domain to this standard interval. To compute the derivative of $f(x)$, we first sample at the points

$$x_j = \frac{2\pi j}{N}, j = 1, \ldots, N, \tag{3.6}$$

and set $v_j = f(x_j)$. Now we can compute the DFT from v_j giving the coefficients $\hat{v}_k$ which is the discrete analogue of $\hat{f}(k)$. Since this is the analogue of the Fourier transform, we now multiply by ik resulting in the analogue of computing the first derivative. Finally, we compute the inverse DFT from $ik\hat{v}_k$ which produces the spectral approximation, v'_j, to the derivative of the sampled function $f'(x)$ at points x_j. However, there is some subtlety involved in treating the wavenumber $N/2$, which is usually set to zero [56].

Despite having a discrete algorithm to compute an analogue of the Fourier transform, our goal has still not been reached because we are still left with doing $\mathcal{O}(N^2)$ operations. This results because there are N coefficients and for each coefficient a sum of N terms must be added together. For small N, computing spectral derivatives are not that much

---

[1]Note that there is no universal standard on where to put the factors of N and 2π.

slower than finite differences methods, however they quickly become impractical for large N. This barrier can be overcome through the Fast Fourier Transform (FFT) algorithm. This algorithm has a rich history and has been rediscovered multiple times, beginning with Gauss in the early 1800s before Fourier published his results on Fourier series [31]. The modern FFT algorithm was developed by Cooley-Tukey in 1965 [17], although it had previously been discovered by others, including Gauss.

The FFT employs a divide and conquer algorithm. The basic idea is to notice that computing the discrete Fourier transform can be divided into even and odd terms which can be computed independently of each other. Thus assuming N is a power of two, we have two new discrete Fourier transform problems of size $N/2$. Each other those problems can themselves be decomposed into problems of size $N/4$. Repeating this process recursively we are able to divide the computation of the DFT into $\mathcal{O}(\log N)$ problems. Computing the DFT of each problem takes roughly $\mathcal{O}(N)$ and thus the total running time is on the order of $\mathcal{O}(N \log N)$. In this simple case, it is easy to prove rigorously from the recursion relationship that the running time is $\mathcal{O}(N \log N)$ using the Master theorem [18].

$\mathcal{O}(N \log N)$ is a general result that holds for all values of N, but the proofs are more complicated and in most applications, N is chosen to be a power of small primes for which their exist many well optimised and developed algorithms. The derivation and implementation of the FFT for general values of N is an interesting and complicated question that has sparked a lot of research into the best way to decompose the problem. Additionally, the actual implementation details can differ depending on the value of N, the type of computer, and the type of data being considered. It is beyond the scope of this thesis to discuss such implementation details and further technical and hardware details that can be used in implementations can be found in [26].

Now that we have an algorithm to compute the FFT, the inverse Fast Fourier Transform (IFFT) can easily be derived since the form of (3.5) is very similar to that of (3.4) and the same strategy of divide and conquer can be applied. With this we have the following algorithm for computing the spectral derivative:

1. Sample function $f(x)$ at N data points x_j to obtain $v_j, j = 1, \ldots, N$.

2. Compute, using the FFT, $\hat{v}_k$ from v_j.

3. Multiply $\hat{v}_k$ by $(ik)^n$ to compute the n-th derivative.

4. Invert $(ik)^n \hat{v}_k$ using the IFFT to obtain an approximation to $f^{(n)}(x)$ at x_j.

To illustrate spectral derivatives, we follow [56] and demonstrate spectral differentiation using two simple examples. Consider the following two periodic functions

$$f(x) = \max(0, 1 - |x - \pi|/2), \qquad g(x) = e^{\sin x} \tag{3.7}$$

which are both periodic on the interval $[0, 2\pi]$.

As we can see in Fig. 3.1 when the original function is sufficiently smooth and periodic, here $g(x)$, the accuracy of the derivative is very good. However, when the function is not smooth, as exhibited in $f(x)$, the accuracy is not very good. Here $g(x)$ is not differentiable at π and spectral methods have a difficult time dealing with this. For a complete discussion of the specific smoothness and accuracy is contained in Chapter 4 of [56].

In this section, we have focused only on simple one-dimensional examples, but the method easily generalises to arbitrary dimensions. To compute multiple partial derivatives, the only change to the algorithm is that we have separate wavenumbers for the different directions. The only modification is computing the higher dimensional FFTs. To compute the n-dimensional FFT of a given function, we must compute the FFT of the all the columns and all the rows in each dimension [31]. For example in 2D dimensions, we would compute the FFT of each of the columns, and then computing the FFT of all the rows of the previous result [39].

3.3 Dealiasing

In the previous section we demonstrated that spectral differentiation can produce very accurate results in only $\mathcal{O}(N \log N)$ operations. However, we have only considered the spectral derivative of a single function $f(x)$. The question naturally arises about what happens if we have products of functions, for example the nonlinear advection terms in the Navier-Stokes equations

$$u\frac{\partial u}{\partial x} + v\frac{\partial u}{\partial y} + w\frac{\partial u}{\partial z}, \tag{3.8}$$

where we now have a product of a function and a derivative. Such terms are known as a convolution and require a more careful treatment. In this section, we introduce two closely related methods for evaluating expressions of the above form, the spectral method and the pseudospectral method. For this we carefully follow the treatment of Durran [23].

Consider the following general 1D non-linear PDE

$$\frac{\partial \psi}{\partial t} + F(\psi) = 0, \tag{3.9}$$
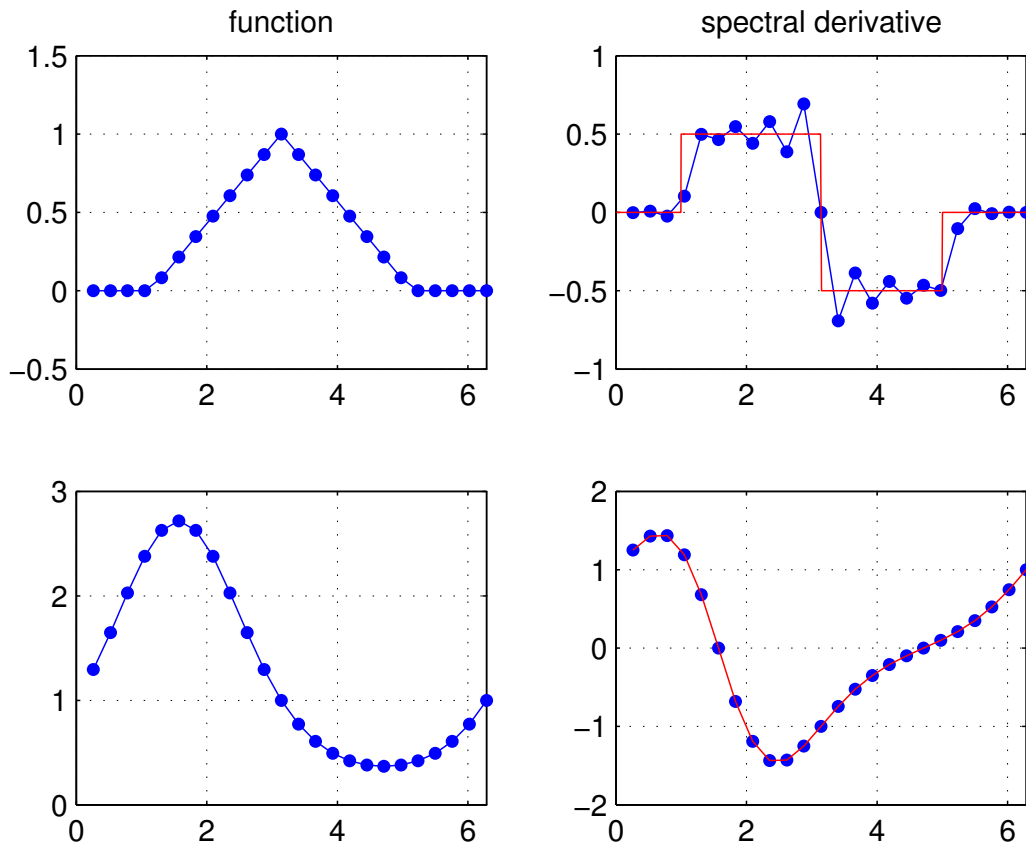
Figure 3.1: Spectral differentiation of two functions $\max(0, 1 - |x - \pi|/2)$ (top) and $e^{\sin x}$ (bottom) following [56]. On the right is the spectral derivative computed with $n = 24$. Red curve represents the exact derivative. Even with such small N, the derivative of $e^{\sin x}$ is very smooth and the $L^{\inf}$ error is on the order of $\mathcal{O}(10^{-13})$. The spectral derivative of $\max(0, 1 - |x - \pi|/2)$ is not as good due to the non-differentiability at $x = \pi$.

where $F(\psi)$ is some general nonlinear function. Consider seeking a series expansion of the form [23]

$$\psi(x,t) \approx \phi(x,t) = \sum_{k=1}^{N} a_k(t)\varphi_k(x), \qquad (3.10)$$

where φ_k are basis functions around which we are interested in expanding the solution. Some examples of such functions might be complex exponentials, Bessel functions, or spherical harmonics. In general, we will not be able to find the eigenfunctions that provide the natural basis to seek a series expansion. Without the proper basis functions, it is clear that the approximate solution will never exactly solve the original PDE and we have to determine a way to minimise the error. For many problems, there is often some degree of symmetry so choosing a certain basis makes sense. For example, for a problem within a periodic box, it makes sense to choose complex exponentials as a basis; if the problem is based on a sphere, spherical harmonics are a natural choice. Thus, we are interested in not finding the correct φ_k for a given problem but instead focus picking a known basis and appropriately choosing $a_k(t)$ to minimise the residual [23],

$$R(\phi) = \frac{\partial \phi}{\partial t} + F(\phi), \qquad (3.11)$$

in some way.

3.3.1 Spectral method

How we choose to minimise this error leads to different methods of solving the problem. The spectral method is a special case of a very general technique called Galerkin approximation. The spectral method requires the residual be orthogonal to the basis functions φ_k, i.e.

$$\int_S R(\phi(x))\varphi_k(x)dx = 0 \qquad k = 1, \ldots, N. \qquad (3.12)$$

For the special case of the spectral method, we require that the basis functions be orthogonal. Other basis functions that are not orthogonal but satisfy other constraints, such as support over very small areas, lead to a different approximation known as the finite element method [23]. It can be shown [23] that (3.12) is equivalent to minimising the L^2 error of the residual.

28

By imposing the above integral, it can be shown [23] that the resulting system of ODEs for the above is

$$\frac{da_k}{dt} = -\frac{1}{M_{k,k}} \int_S \left[F\left(\sum_{n=1}^{N} a_n \varphi_n \right) \varphi_k \right] dx \qquad k = 1, \ldots, N, \tag{3.13}$$

where $M_{k,k} = \langle \varphi_k, \varphi_k \rangle$. For our work, we are interested in a specific case of basis functions, $\varphi_k(x) = e^{ikx}$ and the inner product is the standard inner product for complex functions

$$\int_S g(x) h^*(x) dx = 0. \tag{3.14}$$

To demonstrate the above formulation, we use the spectral method to solve the 1D advection equation with variable windspeed on the interval $[0, 2\pi]$,

$$\frac{\partial \phi}{\partial t} + c(x,t)\frac{\partial \phi}{\partial x} = 0, \, F(\phi) = c(x,t)\frac{\partial \phi}{\partial x}. \tag{3.15}$$

We now expand out $\phi(x,t)$ as the sum of $N = 2K + 1$ Fourier modes, where here we are now letting N be an odd number in contrast to the previous section where N was even. This is chosen because it simplifies the formulas, however the results hold for even N as well, but with some slight alterations to the algebra. Expanding the variable in terms of a Fourier basis

$$\phi(x_j, t) = \sum_{n=K}^{K} a_n(t) e^{inx_j}, \tag{3.16}$$

and substituting this into the above yields

$$\frac{da_k}{dt} = -\frac{i}{2\pi} \sum_{n=-K}^{K} n a_n \int_{-\pi}^{\pi} c(x,t) e^{i(n-k)x} dx \qquad k = -K, \ldots, K. \tag{3.17}$$

Expanding out $c(x,t)$ as a Fourier series we obtain

$$\frac{da_k}{dt} = -\frac{i}{2\pi} \sum_{n=-K}^{K} \sum_{m=-K}^{K} n a_n c_m \int_{-\pi}^{\pi} e^{i(n+m-k)x} dx \qquad k = -K, \ldots, K, \tag{3.18}$$

and upon using the orthogonality of the integral, we obtain

$$\frac{da_k}{dt} = - \sum_{\substack{m+n=k \\ |m|,|n| \leq K}} i n c_m a_n, \tag{3.19}$$

29

where we require that $n+m = k$ and $|n|, |m| \leq K$. If we want to evaluate this sum directly, we would need to evaluate $\mathcal{O}(K^2)$ operations due to the double sum in the convolution. Historically, this was a barrier for spectral methods because even though they provided accurate results, this $\mathcal{O}(K^2)$ bottleneck did not allow for larger numerical simulations, where $\mathcal{O}(K)$ finite differences method could [23].

In order to get around this bottleneck, we can turn the $\mathcal{O}(K^2)$ to $\mathcal{O}(K \log K)$ using the FFT. The general idea is as follows: transform the Fourier coefficients to real space in $\mathcal{O}(K \log K)$, multiply the two terms together at each grid point in $\mathcal{O}(K)$, and transform back to Fourier space in $\mathcal{O}(K \log K)$. The resulting algorithm is $\mathcal{O}(K \log K)$. However, if we were to implement this naively, errors would arise, due to the phenomena of aliasing.

At a basic level, aliasing is the result of multiplying two terms grid-pointwise that generate short waves that can be aliased into long waves. This arises in the spectral method when we compute the product of two Fourier coefficients. A very similar, but exaggerated example, is known as the wagon wheel effect and can illustrate the general idea of short waves being interpreted as long waves [72]. The wagon wheel effect arises when an object appears to be stationary but is really moving. For example, imagine a camera that takes a picture every second of a turbine, but the turbine is moving at 10 revolutions per second. For someone looking at the shots from the camera, they would claim the turbine isn't moving. If the turbine is moving slightly faster, say 10.1 revolutions per second, the camera would show that the turbine is moving, albeit rather slowly. If it were moving slightly slower, say 9.9 revolutions per second, the camera would show the turbine moving backwards. Thus one would interpret the turbine as moving very slowly in either case and thus conclude that it must have a very slow period, or long wavelength. In actuality, the period is much more rapid and the wavelength of one revolution is much shorter.

Mathematically, we can see a similar phenomena by sampling a sine wave. Consider Fig. 3.2 which has 11 points. The short wavelength red sine curve samples these points with a short wavelength while a longer wavelength blue curve also samples, despite being non-existent in the actual data. The goal is to minimise this effect.

To illustrate this consider two functions $f(x), g(x)$. We want to compute the Fourier coefficients of the product

$$f(x)g(x) = \sum_{m=-K}^{K} p_k e^{ikx}, \tag{3.20}$$
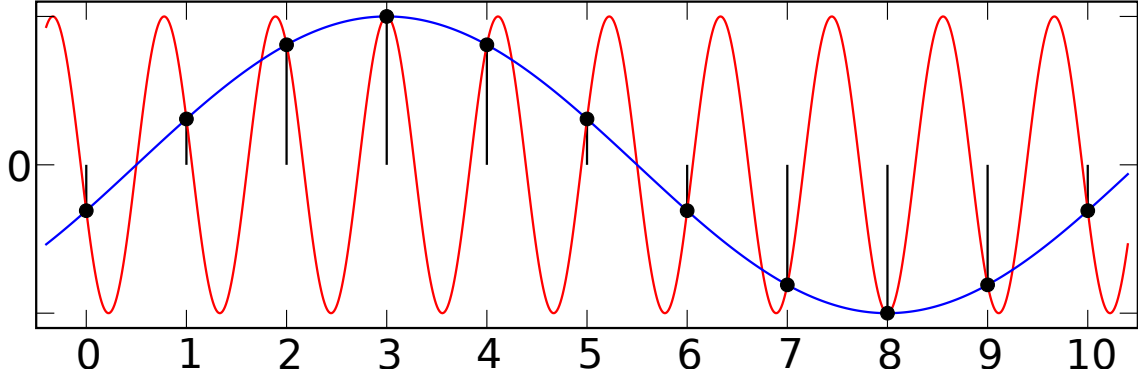
Figure 3.2: Different sine curves that fit the same set of data points (from [71]). This is an example of aliasing.

and we can expand $f(x), g(x)$ as Fourier series

$$f(x) = \sum_{m=-K}^{K} a_m e^{imx}, \qquad g(x) = \sum_{n=-K}^{K} b_n e^{inx}. \tag{3.21}$$

The above algorithm states that we convert the Fourier coefficients a_m, b_n to real space and multiply. Suppose that in real space the spacing between the grid points is

$$\Delta x = \frac{2\pi}{2N+1}, \tag{3.22}$$

where we let $2N + 1$ denotes the total number of grid points.

How do we choose N? Naively, it seems logical to set that $N = K$ so that both real and Fourier space have the same number of co-efficients. This naive choice leads to aliasing error and instead we must choose $N > K$ to avoid this aliasing error. To get intuition for why, aliasing error arises when two poorly resolved waves are multiplied together and produce a longer wavelength wave, as discussed above in Fig. 3.2. We can avoid this if all short wavelengths are resolved properly.

To find the optimal value of N, consider multiplying two functions given by Fourier modes, each with the largest wavenumber K. This product generates a wave with wavenumber $2K$, recalling that multiplication of waves is addition of the wavenumbers. The largest possible resolvable wavenumber in the real space grid is $\pi/\Delta x = N$. Here we can explicitly

31

see what happens if $K = N$. The $2K = 2N$ waves would not be resolved properly because the largest possible wavenumber to be resolved is only N. An obvious choice to fix this is to choose $N = 2K$ and thus we could resolve all possible wavenumbers. However this choice is too loose a bound since it would imply that for every simulation, we would require twice as many grid space coefficients as Fourier coefficients. It is possible to do better.

To do better, consider which wavenumber the $2K$ would be aliased into, which will be $2K - 2\pi/\Delta x$ thus

$$K < |2K - \frac{2\pi}{\Delta x}|, \tag{3.23}$$

and upon subbing in Δx we find that

$$N > \frac{3}{2}K - 1. \tag{3.24}$$

There is an alternative way to get at the same result. Consider the discrete Fourier transform of the product $f(x)g(x)$

$$p_k = \frac{1}{2N+1} \sum_{j=1}^{2N+1} f(x_j)g(x_j)e^{-ikx_j}, \tag{3.25}$$

and now plug in the

$$f(x) = \sum_{m=-N}^{N} a_m e^{imx}, \qquad g(x) = \sum_{n=-N}^{N} b_n e^{inx}, \tag{3.26}$$

where we have replaced K with N where $N > K$. This is the same expansion as before but we have set $a_l, b_l = 0$ if $K < |l| \le N$. Substituting these into the above yields

$$p_k = \frac{1}{2N+1} \sum_{m=-N}^{N} \sum_{n=-N}^{N} \sum_{j=1}^{2N+1} a_m b_n e^{i(m+n-k)x_j}. \tag{3.27}$$

Recalling that $x_j = 2\pi j/(2N+1)$ the inner summation is

$$\sum_{j=1}^{2N+1} e^{i(m+n-k)x_j} = \begin{cases} 1 & m+n-k = 0, \\ 1 & m+n-k = 2N+1, \\ 1 & m+n-k = -(2N+1), \\ 0 & \text{otherwise}, \end{cases} \tag{3.28}$$

32

which is a restatement of the well known orthogonality condition [23]. Thus we can break up the above summation into three cases, $m + n = k, m + n = k \pm (2N + 1)$ which gives

$$p_k = \sum_{\substack{m+n=k \\ |m|,|n| \leq N}} a_m b_n + \sum_{\substack{m+n=k+2N+1 \\ |m|,|n| \leq N}} a_m b_n + \sum_{\substack{m+n=k-2N-1 \\ |m|,|n| \leq N}} a_m b_n. \qquad (3.29)$$

Note the similarity with the result from the spectral method, which is identical to summation encountered in the spectral method, recalling that the coefficients are zero for values greater then K. The aliasing error arises from the second two terms. We want to eliminate this error so we have to decide how to choose N to eliminate this term. We consider the first aliasing error term. We have that if $m, n > K$ then $a_m b_n = 0$. It follows that $m + n > 2K$ this term will vanish, i.e. $m + n = k + 2N + 1 > 2K$ for all $k = -K, \ldots, K$. Thus we want to consider $k = -K$ since this is the smallest possible value of this summation, i.e. $-K + 2N + 1 > 2K$. Rearranging this yields $N > (3K - 1)/2$ as before. An identical argument gives the same result for the other aliasing term.

This dealiasing rule is known as the "two-thirds rule" and will completely eliminate aliasing effects. The above algorithm tells us how to choose N given K, however in many applications we typically work the other way around, choosing N and limiting K. We now can now write down the algorithm for evaluating the following term $c(x)\partial\phi/\partial x$ in Fourier space, when we are initially only given M samples:

- Sample $c(x), \phi(x, t)$ at M points.

- Compute the Fourier coefficients of $c(x), \phi(x, t)$ using the FFT yielding M Fourier coefficients a_i, b_j respectively.

- Evaluate the spectral derivative of ϕ by multiplying the coefficients by ik, i.e $a_l = ik a_l$.

- Modify the Fourier coefficients so the top $1/3$ are zero.

- Take the IFFT back to real space.

- Multiply the real space coefficients gridwise.

- Take the FFT of this product.

This procedure will allow us to evaluate the Navier-Stokes equations in Fourier space by evaluating convolution terms by multiplying fields in real space and to eliminate numerical error. In the next section, we provide a simple example that illustrates this method in practice.

3.3.2 Pseudospectral method

We have so far been focusing on eliminating the aliasing error at the cost of eliminating some Fourier modes which can be achieved by taking $N > 3K/2$. A closely related method known as the pseudospectral method is an alternative way to evaluate the above equations. In this case, instead of enforcing that the residual is orthogonal to the basis functions, we instead choose a collocation method [23], i.e.

$$R(\phi(j\Delta x)) = 0, \tag{3.30}$$

where we enforce that the coefficients satisfying the equation at each grid point. An alternate viewpoint of the pseudospectral method using interpolation of sinc functions [14, 56]. Let us now expand $\phi(x,t), c(x,t)$ are Fourier series

$$\phi(x,t) = \sum_{n=-K}^{K} a_n e^{inx}, \qquad c(x,t) = \sum_{m=-K}^{K} c_m e^{imx}. \tag{3.31}$$

Substituting into the test equation and enforcing the collocation requirement yields

$$\sum_{n=-K}^{K} \frac{da_n}{dt} e^{inx_j} + \sum_{m=-K}^{K} c_m e^{imx_j} \sum_{n=-K}^{K} ina_n e^{inx_j} = 0. \tag{3.32}$$

which we can alternatively write as

$$\frac{d\phi_j}{dt} + c_j \frac{\partial \phi_j}{\partial x} = 0, \tag{3.33}$$

where we have written

$$\phi(x_j) = \sum_{n=-K}^{K} a_n e^{inx_j}, c(x_j) = \sum_{n=-K}^{K} c_n e^{inx_j}, \frac{\partial \phi_j}{\partial x} = \sum_{n=-K}^{K} ina_n e^{inx_j}. \tag{3.34}$$

This is the set of equations we want to solve. Thus we now have a way to evaluate using the following algorithm:

1. Evaluate $\phi(x,t), c(x,t)$ at M points.

2. Compute the spectral derivative of $\phi(x,t)$ using the methods of the previous sections.

3. Multiply all the coefficients gridpoint wise.

4. Timestep the resulting solution.

3.3.3 Spectral vs pseudospectral

The equations resulting from the pseudospectral method are actually very similar to the spectral equations except that there is no dealiasing. To see why, multiply the above equation by e^{-ikx_j} and sum over all j and we will obtain

$$\frac{da_k}{dt} = -\sum_{\substack{m+n=k \\ |m|,|n|\leq K}} inc_m a_n - \sum_{\substack{m+n=k+2K+1 \\ |m|,|n|\leq K}} inc_m a_n - \sum_{\substack{m+n=k-2K-1 \\ |m|,|n|\leq K}} inc_m a_n. \tag{3.35}$$

For comparison, the spectral method equations are

$$\frac{da_k}{dt} = -\sum_{\substack{m+n=k \\ |m|,|n|\leq K}} inc_m a_n, \tag{3.36}$$

where in both equations $k = -K \ldots, K$.

There are many similarities between these two equations but we have to remember that they were derived in two completely different ways. Recall that to evaluate the convolution term in the spectral method, we obtained the following equation

$$p_k = \sum_{\substack{m+n=k \\ |m|,|n|\leq N}} a_m b_n + \sum_{\substack{m+n=k+2N+1 \\ |m|,|n|\leq N}} a_m b_n + \sum_{\substack{m+n=k-2N-1 \\ |m|,|n|\leq N}} a_m b_n. \tag{3.37}$$

which has the exact same form as the pseudospectral method but the crucial difference is that the sum is over N and not K. If we set $N = K$, which would result in dealiasing error, we would obtain the pseudospectral method. Thus, at a fundamental level, the pseudospectral method is just the spectral method without dealiasing.

3.4 Timestepping and examples

Recall that our model 1D problem is

$$\frac{\partial \psi}{\partial t} + F(\psi) = 0. \tag{3.38}$$

We have been focusing on evaluating the $F(\psi)$ term but now we turn to the time derivative term. Fortunately, this term is much simpler to deal with than the nonlinear terms since it appears only as a single derivative.

To evaluate this term, consider the approximation to the first derivative [23]

$$\frac{\partial \psi}{\partial t} \approx \frac{\psi^{n+1} - \psi^n}{\Delta t}. \tag{3.39}$$

Here the subscript now denote the solution ψ evaluated at nth timestep. Now that the time derivative is handled, at what timestep do we evaluate the $F(\psi)$ term? We could evaluate it at ψ_n or ψ_{n+1} or maybe other possible previous times. Let us consider evaluating at ψ_n. Now substituting everything in we obtain the following scheme, known as the forward Euler scheme [23]

$$\psi_{n+1} = \psi_n - \Delta t F(\psi_n). \tag{3.40}$$

Here the right hand side is a function solely of ψ_n. When a scheme can be written as a function of all previous terms, the scheme is known as explicit. However, we could have chosen to evaluate ψ at ψ_{n+1} and we would obtain the backward Euler scheme [23]

$$\psi_{n+1} = \psi_n - \Delta t F(\psi_{n+1}). \tag{3.41}$$

Here, if $F(\psi)$ is nonlinear function, we cannot isolate for ψ_{n+1}. Instead we would have to use some sort of root finding solver to find the correct ψ_{n+1} given ψ_n. Schemes that exhibit this property are known as implicit schemes. Depending on the problem at hand, one scheme may be better than the other. For this thesis, we uses second and third order Adams-Bashforth, following previous work [11, 66].

Once we have chosen a time-stepping scheme, the stability of the scheme is important to know. If we pick Δt too large, for example, the right hand side might grow too large and become unstable. By finding the stability region of a scheme, it tells us when we can except our solution to not blow up. To investigate this we define the amplitude A to be

$$A = \frac{\psi_{n+1}}{\psi_n}, \tag{3.42}$$

and stability is defined to be

$$|A|^2 \leq 1, \tag{3.43}$$

since A can potentially be complex. The reasoning from this equation arises from rearranging the above so that $\psi_{n+1} = A\psi_n$. If $|A| \leq 1$ then the solution is not growing in time. If $|A| > 1$ then at each time-step the solution is being multiplied by a number greater then

one, hence it is growing. To illustrate, we use the second order Adams-Bashforth scheme [23]

$$\psi_{n+1} = \psi_n + \frac{\Delta t}{2}(3F(\psi_n) - F(\psi_{n-1})). \tag{3.44}$$

Clearly the growth rate of a scheme will depend on the given function $F(\psi)$. However the standard procedure is to investigate the following model problem [23]

$$\frac{d\psi}{dt} = (\lambda + i\omega)\psi. \tag{3.45}$$

where λ, ω are real numbers.

To determine the stability region we use the method from Leveque [34] which gives a stability region of

$$z = \frac{2(\xi^2 - \xi)}{3\xi - 1}, \tag{3.46}$$

where ξ is the unit circle. Fig. 3.3 illustrates the stability region of the Adams-Bashforth second order.

To illustrate time-stepping schemes and how they are applied to problems, consider the following one dimensional advection equation [56]

$$\frac{\partial u}{\partial t} + c(x)\frac{\partial u}{\partial x} = 0, \qquad c(x) = \frac{1}{5} + \sin^2(x - 1), \qquad u(x,0) = e^{-100(x-1)^2}, x \in [0, 2\pi], \tag{3.47}$$

that we solve on a periodic domain. The physical interpretation of this equation is the simple one dimensional advection of a velocity field $u(x,t)$ by the fixed velocity $c(x)$. To evaluate the advection term, we use a spectral method with 2/3-rule dealiasing. As discussed in the previous section, there is still non-standard terminology throughout the literature regrading the names of the various methods of using FFTs. Trefethen, for example, calls pseudospectral methods, 'collocation methods' [56] which is also a term used by Durran [23], although Durran prefers the term pseudospectral.

For a time-stepping scheme, we use a second-order Adams-Bashforth[23] scheme. Rewriting wave-equation as

$$\frac{\partial u}{\partial t} = -c(x)\frac{\partial u}{\partial x} = F(u), \tag{3.48}$$
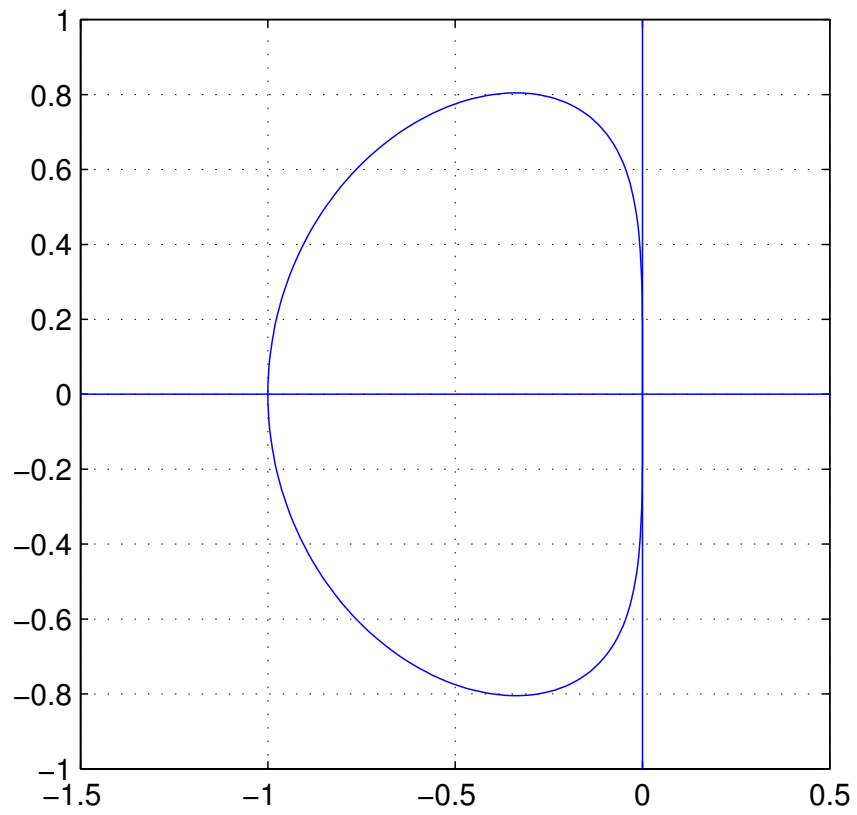
37

Figure 3.3: Stability region of Adams-Bashforth second order. Adapted from [56]

which we can write in Fourier space as

$$\frac{\partial \hat{u}}{\partial t} = -\widehat{c(x)\frac{\partial u}{\partial x}} = F(\hat{u}), \tag{3.49}$$

where the dependence on k has been suppressed for clarity. The Adams-Bashforth scheme is

$$\hat{u}^{n+1} = \hat{u}^n + \frac{\Delta t}{2}[3F(\hat{u}^n) - F(\hat{u}^{n-1})]. \tag{3.50}$$

Since the Adams-Bashforth scheme uses a previous time-step, we will use forward Euler for the first time-step. To evaluate $F(\hat{u})$ we will use the spectral differentiation, as discussed above. See Appendix A for the sample MATLAB code which illustrates how to achieve dealiasing in practice.

Fig. 3.4 demonstrates the solution to the above advection equation using spectral methods. As can be observed, the solution is very smooth and evolves very clearly for only $N = 128$.

In the previous section we discussed spectral and pseudospectral schemes. To illustrate another difference between the two, we solve the viscous Burgers equation using both spectral and pseudospectral methods [23]

$$\frac{\partial \psi}{\partial t} + \psi\frac{\partial \psi}{\partial x} = \nu\frac{\partial^2 \psi}{\partial x^2}. \tag{3.51}$$

The initial condition used was a Gaussian. To handle the time-stepping, we use an Adams-Bashforth second order as discussed above. Fig. 3.5 illustrates the results of the numerical experiment. Initially, both the spectral and pseudospectral codes have similar energy but after around 1 time unit, the pseudospectral solution is dissipating energy faster than the spectral. However, the key difference is that at around $T = 3.6$ the pseudospectral code blows up due to nonlinear instability associated with aliasing error [23]. The spectral code, which does dealiasing, does not experience this divergence and continues to decay due to viscous effects. Indeed, it can be shown [23] that for inviscid problems, the spectral method will conserve energy. This example illustrates the importance and necessity of dealiasing.

3.5 Navier-Stokes equations in Fourier space

3.5.1 Fourier transformed Navier-Stokes

We now turn to the formulation of the Navier-Stokes equations in the Fourier domain which provides a convenient formulation to analyse the underlying mechanisms of turbulence.
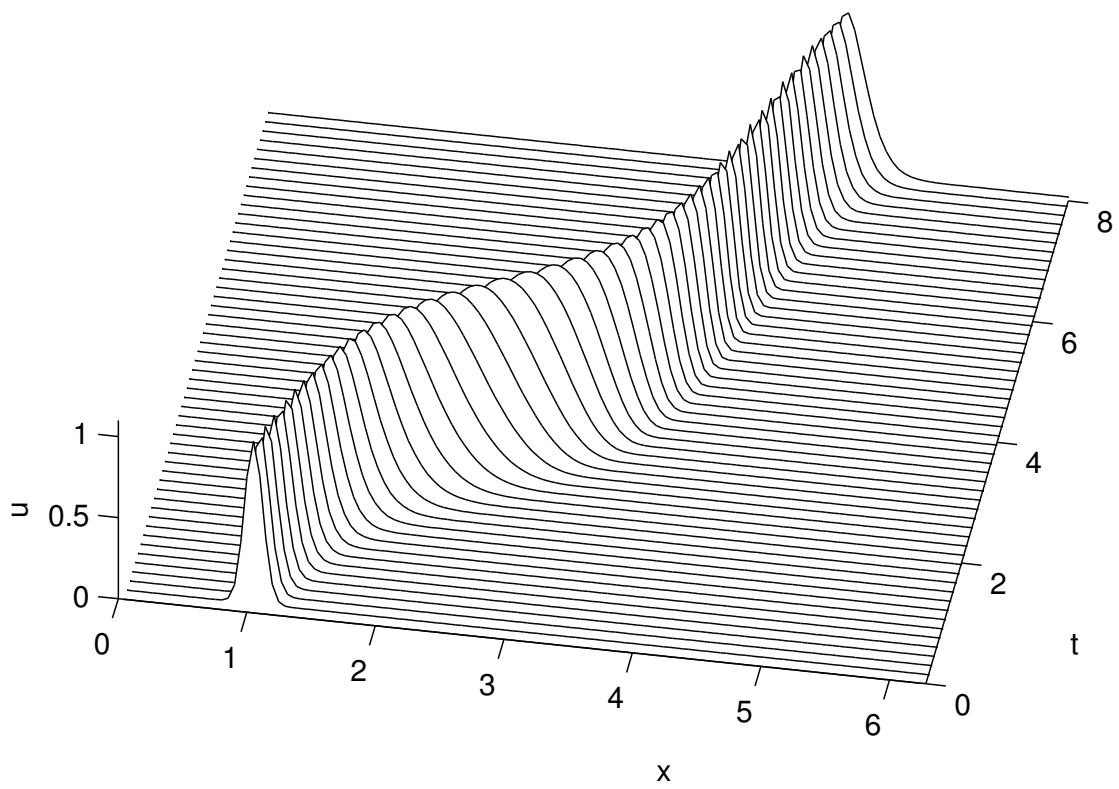
Figure 3.4: Spectral solution to the advection equation with variable windspeed. This figure is based on Output 6 of Trefethen [56] modified to include dealiasing.
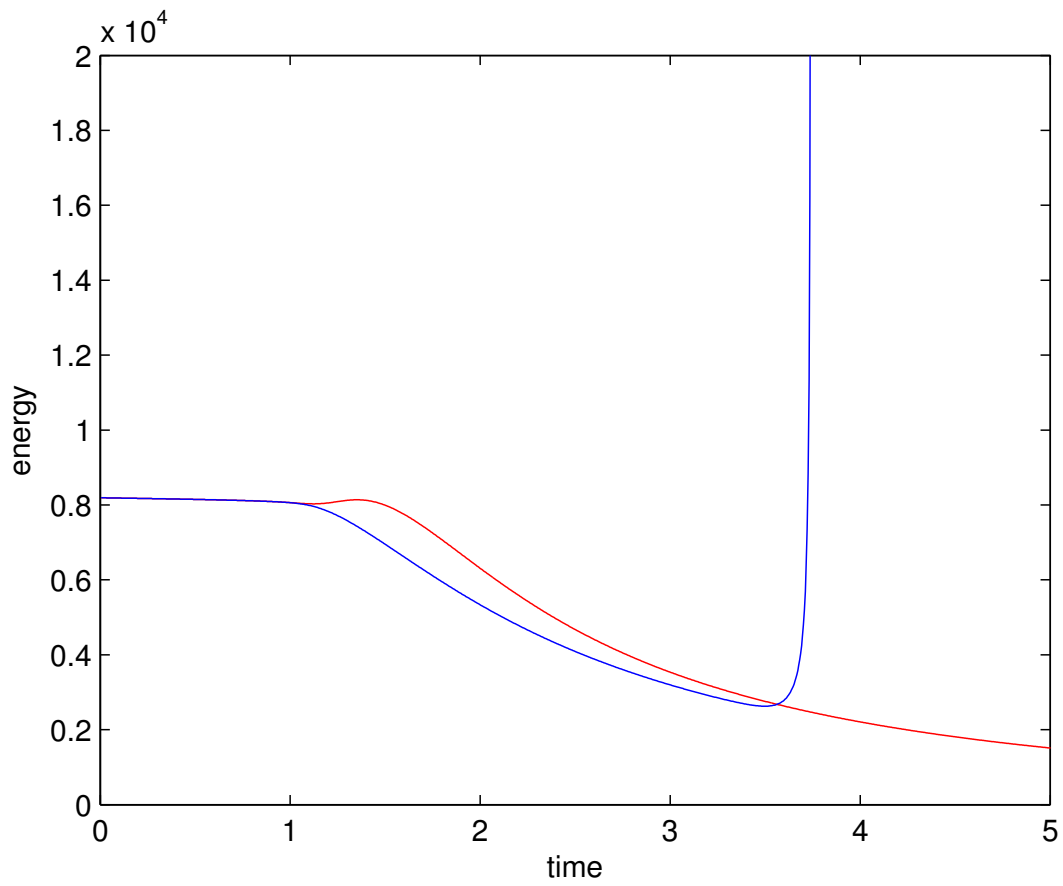
Figure 3.5: Solution to the viscous Burgers equation using spectral (red) and pseudospectral (blue).

Recall that in the Fourier domain, derivatives become multiplication of wavenumbers which converts the spatial derivatives of the Navier-Stokes equations into algebraic equations. To demonstrate the formulation in Fourier space, let us cast the standard Navier-Stokes equations into Fourier space.

$$\frac{\partial \boldsymbol{u}}{\partial t} + \boldsymbol{u} \cdot \nabla \boldsymbol{u} = -\frac{1}{\rho_0} \nabla p + \nu \nabla^2 \boldsymbol{u}, \qquad \nabla \cdot \boldsymbol{u} = 0, \tag{3.52}$$

Taking the Fourier transform of the above equation is straight-forward for all terms except the advection term $\boldsymbol{u} \cdot \nabla \boldsymbol{u}$, which we postpone for now.

In Fourier space, we can also exploit the following observation to eliminate the pressure term (e.g. [33]). The incompressibility condition becomes $\mathbf{k} \cdot \hat{\boldsymbol{u}}(\mathbf{k}, t) = 0$ in Fourier space. Geometrically, this means that the vectors $\mathbf{k}$ and $\hat{\boldsymbol{u}}$ are orthogonal. This realisation tells us that vectors that are proportional to $\hat{\mathbf{u}}$ are orthogonal to vectors that are proportional to $\mathbf{k}$. Thus writing out the Navier-Stokes equations

$$\frac{\partial \hat{\boldsymbol{u}}}{\partial t} + \mathcal{F}(\boldsymbol{u} \cdot \nabla \boldsymbol{u}) = -\frac{1}{\rho_0} \mathbf{k} \hat{p} - \nu k^2 \hat{\boldsymbol{u}}, \tag{3.53}$$

take the dot product with $\mathbf{k}$ and using the orthogonality condition we obtain

$$\mathbf{k} \cdot \mathcal{F}(\boldsymbol{u} \cdot \nabla \boldsymbol{u}) + \frac{1}{\rho_0} k^2 \hat{p} = 0. \tag{3.54}$$

Isolating for pressure and substituting back into (3.53) we obtain

$$\frac{\partial \hat{\boldsymbol{u}}}{\partial t} + \mathcal{F}(\boldsymbol{u} \cdot \nabla \boldsymbol{u})(\mathbf{1} - \frac{\mathbf{k}\mathbf{k}}{k^2}) = -\nu k^2 \hat{\boldsymbol{u}}. \tag{3.55}$$

This result is unsurprising, since all we have done is take the divergence of the Navier-Stokes equations, which in Fourier space corresponds to taking the dot product with respect to $\mathbf{k}$. But using this observation we can avoid the need for solving the pressure altogether because the pressure term is orthogonal to the $\hat{\boldsymbol{u}}$-plane. But what about the advection term? As can be seen in (3.55), it has this factor $\mathbf{1} - \mathbf{k}\mathbf{k}/k^2$ multiplying it. This term represents a projection into the $\hat{\boldsymbol{u}}$-plane. The advection term can thought of a vector that is pointing in some direction in-between the planes of $\mathbf{k}$ and $\hat{\boldsymbol{u}}$. By projecting the advection term into the $\hat{\boldsymbol{u}}$-plane, we would have a set of equations that are independent of the pressure completely.

3.5.2   Projection tensor

In order to project the Navier-Stokes equations onto the $\hat{\boldsymbol{u}}$-plane, we define the following projection operator

$$\mathbf{P} = \mathbf{1} - \frac{\mathbf{kk}}{k^2} \text{ or } P_{ij}(\mathbf{k}) = \delta_{ij} - \frac{k_i k_j}{k^2}, \tag{3.56}$$

where we are using Einstein summation notation [33, 67]. It is straightforward to verify that $P_{ij}P_{jk} = P_{ik}$ or in matrix notation $\mathbf{P}^2 = \mathbf{P}$, in other words the projection tensor is idempotent. Idempotence is a defining feature of projection operators [42]. It is straightforward to verify that $k_j P_{ij} = 0$ and $\hat{u}_j P_{ij} = \hat{u}_i$. These simple observations confirm that the projection tensor projects a vector onto the $\hat{\boldsymbol{u}}$-plane.

Applying P_{ij} to (3.53) we obtain the following

$$\frac{\partial \hat{\boldsymbol{u}}}{\partial t} + \mathbf{P}\mathcal{F}(\boldsymbol{u} \cdot \nabla \boldsymbol{u}) = -\nu k^2 \hat{\boldsymbol{u}}, \tag{3.57}$$

where $\mathbf{P}$ is acting on the Fourier transform of the advection term. In order to compute the Fourier transform of the advection term, we note that

$$\boldsymbol{u} \cdot \nabla \boldsymbol{u} = u_j \frac{\partial u_i}{\partial x_j} = \frac{\partial(u_i u_j)}{\partial x_j}, \tag{3.58}$$

where the incompressibility condition has been used to bring the velocity inside the derivative. Thus we are able to write

$$\mathcal{F}(\boldsymbol{u} \cdot \nabla \boldsymbol{u}) = ik_j \int_{\mathbf{p}+\mathbf{q}=\mathbf{k}} d\mathbf{k} \hat{u}_i(\mathbf{p}) \hat{u}_j(\mathbf{q}), \tag{3.59}$$

and hence we can finally write out the Navier-Stokes equations in Fourier space as [33]

$$\frac{\partial \hat{u}_i}{\partial t} + iP_{ij}k_m \int_{\mathbf{p}+\mathbf{q}=\mathbf{k}} d\mathbf{k} \hat{u}_j(\mathbf{p}) \hat{u}_m(\mathbf{q}) = -k^2 \hat{u}_i. \tag{3.60}$$

3.5.3   Numerical formulation of Navier-Stokes in Fourier

Although we have eliminated the pressure completely, we still have the nonlinear term in the equation. To formulate this problem numerically, we make the following observation that is useful in spectral methods [33, 47].

Recall the following identity [32, 1]

$$\boldsymbol{u} \cdot \nabla \boldsymbol{u} = \boldsymbol{\omega} \times \boldsymbol{u} - \frac{1}{2} \nabla \boldsymbol{u}^2, \tag{3.61}$$

When we apply the projection operator $\mathbf{P}$ to the above equation, the $\nabla \boldsymbol{u}^2$ term will vanish since it is orthogonal to the $\hat{\boldsymbol{u}}$-plane. For the cross product between the vorticity and velocity, we use the methods discussed above from dealiasing. Thus to evaluate the cross product term, we assume we have the Fourier transform of the vorticity and velocity $\hat{\boldsymbol{\omega}}, \hat{\boldsymbol{u}}$ and re-write the cross product term as

$$\mathcal{F}(\boldsymbol{\omega} \times \boldsymbol{u}) = \mathcal{F}(\mathcal{F}^{-1}(\hat{\boldsymbol{\omega}}) \times \mathcal{F}^{-1}(\hat{\boldsymbol{u}})). \tag{3.62}$$

Using this result we can reformulate the Navier-Stokes equations into a form to be solved numerically using a spectral method

$$\frac{\partial \hat{\boldsymbol{u}}}{\partial t} = -\mathbf{P}(\mathbf{k}) \mathcal{F}(\mathcal{F}^{-1}(\hat{\boldsymbol{\omega}}) \times \mathcal{F}^{-1}(\hat{\boldsymbol{u}})) - \nu k^2 \hat{\boldsymbol{u}}, \tag{3.63}$$

where the $\mathcal{F}, \mathcal{F}^{-1}$ can be evaluated by FFTs, as discussed above.

This reformulation of the Navier-Stokes equations into Fourier space simplifies numerical calculations immensely and provides many advantages over the real space formulation. The absence of the pressure term means that there is no Poisson equation to be solved at each time-step for the pressure. If one did want the pressure, one can solve (3.54) for $\hat{p}$. In addition there is no need to enforce a divergence free solution[2] as the equations are formulated by definition to satisfy divergence free condition. The only additional technical difficulty is evaluating the vorticity, but this can easily be handled because of the simple structure of the curl.

The above has been focused on the Navier-Stokes equations and not the Boussinesq equations, however the extension to these equations is straightforward. The only additional complexities are an additional equation which can be solved analogously to the momentum equation [33].

3.5.4 Integrating factor

Another advantage of the Fourier formulation is the ability to exactly integrate the diffusion term. Let us denote the advective projective term as $F(\hat{\boldsymbol{u}})$ and we have

$$\frac{\partial \hat{\boldsymbol{u}}}{\partial t} + \nu k^2 \hat{\boldsymbol{u}} = F(\hat{\boldsymbol{u}}), \tag{3.64}$$

---

[2] Except possibly at the initial time step and periodically during a simulation due to numerical errors.

where the left-hand side has been explicitly written out. Written in this form, the common trick of writing a product as a derivative is observed since

$$\frac{\partial \hat{\boldsymbol{u}}}{\partial t} + \nu k^2 \hat{\boldsymbol{u}} = e^{-\nu k^2 t} \frac{\partial}{\partial t}(\hat{\boldsymbol{u}} e^{\nu k^2 t}), \tag{3.65}$$

Thus we can re-write the Navier-Stokes equations as

$$\frac{\partial}{\partial t}(\hat{\boldsymbol{u}} e^{\nu k^2 t}) = e^{\nu k^2 t} F(\hat{\boldsymbol{u}}). \tag{3.66}$$

For notational convenience, let us write $g(t) = e^{\nu k^2 t}$ and note the following trivial identities

$$g(t \pm \Delta t) = g(t)g(\pm\Delta t), \qquad g(0) = 1, \qquad g(t)^{-1} = g(-t). \tag{3.67}$$

With this notation the Navier-Stokes equations become

$$\frac{\partial(\hat{\boldsymbol{u}} g(t))}{\partial t} = g(t) F(\hat{\boldsymbol{u}}). \tag{3.68}$$

Now let us solve the above system using an Adams-Bashforth second order time-stepping scheme. Initially we obtain

$$\hat{\boldsymbol{u}}^{n+1} g(t_n + \Delta t) = \hat{\boldsymbol{u}}^n g(t_n) + \frac{3}{2}\Delta t g(t_n) F(\hat{\boldsymbol{u}}^n) - \frac{1}{2}\Delta t g(t_{n-1}) F(\hat{\boldsymbol{u}}^{n-1}). \tag{3.69}$$

Using the identities in (3.67) the scheme reduces to

$$\hat{\boldsymbol{u}}^{n+1} = g(-\Delta t)\hat{\boldsymbol{u}}^n + \frac{3}{2}\Delta t g(-\Delta t) F(\hat{\boldsymbol{u}}^n) - \frac{1}{2}\Delta t g(-2\Delta t) F(\hat{\boldsymbol{u}}^{n-1}), \tag{3.70}$$

and the diffusion term has been reduced to a multiplication by a constant factor $g(-\alpha\Delta t)$.

3.5.5 Hyperviscosity

Unless we are performing direct numerical simulations, in which all scales down to the viscous scales are resolved, fluid simulations will not resolve all scales of a flow. As a result, some mechanism is necessary to smooth the solution at small scales and avoid a build-up of energy at the grid scale. Approaches for spectral methods, which have no implicit numerical diffusion, include filtering and hyperviscosity (e.g. Boyd [14]).

Hyperviscosity is a method of simulating higher Reynolds number flow by replacing the diffusion term with higher derivatives. In the Fourier picture, the diffusion term is $-\nu k^2 \hat{\boldsymbol{u}}$.

The diffusion timescale τ_d is given by the inverse of νk^2. This implies that the longest wavelengths (smallest k) have very long diffusive time-scales while the shortest wavelengths (larger k) have very short diffusive time-scales. This picture makes physical sense since viscosity plays the most important role at the very small scales. As we decrease the viscosity ν the time-scales of all scales increases. Numerically, if we decrease the viscosity too much, resolution of the smallest scales becomes critical and can lead to unwanted grid-scale effects. Thus, in order to decrease the diffusive time-scales of all wavelengths we can instead vary the power of the wave number. For example, going from k^2 to k^4, and adjusting the coefficient accordingly, the time-scales of the various wavelengths would decrease. This is illustrated in Fig 3.6.

In order to incorporate hyperviscosity numerically, we scale the coefficient by the maximum wavenumber k_{max}. We want the diffusive timescales of the smallest scales to be the same for both the regular viscosity and the hyperviscosity. That is we want

$$\nu k_{max}^2 = \nu_i k_{max}^i, \tag{3.71}$$

where i is an even integer. Solving for ν_i then gives the following replacement

$$\nu k^2 \Rightarrow \nu k_{max}^{2-i} k^i. \tag{3.72}$$

For hyperviscosity simulations in this thesis, we will use $i = 4$, although $i = 8$ is also common [3, 38].

3.5.6 Concluding remarks

Although we have done all our manipulations in Fourier space, we could have equally well formulated the above equations in real space. The idea of projecting the velocity field onto the $\hat{\boldsymbol{u}}$-plane is motivated by the Helmholtz decomposition. This decomposition states, for any C^2 vector field in a bounded region of $\mathbb{R}^3$, we can decompose the vector field into a divergence-free and curl-free component. The divergence free part corresponds to taking the divergence of the Navier-Stokes equations which would yield the Poisson equation for the pressure. Taking the curl of the Navier-Stokes equation - which we define to be the vorticity - would yield the vorticity equation which does not have a pressure term.

3.6 Numerical scheme for linear Boussinesq equations

We now write the fields as a basic state, denoted by a subscript 0, plus perturbations, denoted by $\sim$. Ignoring the viscous diffusion of the basic state [11, 22] and neglecting products

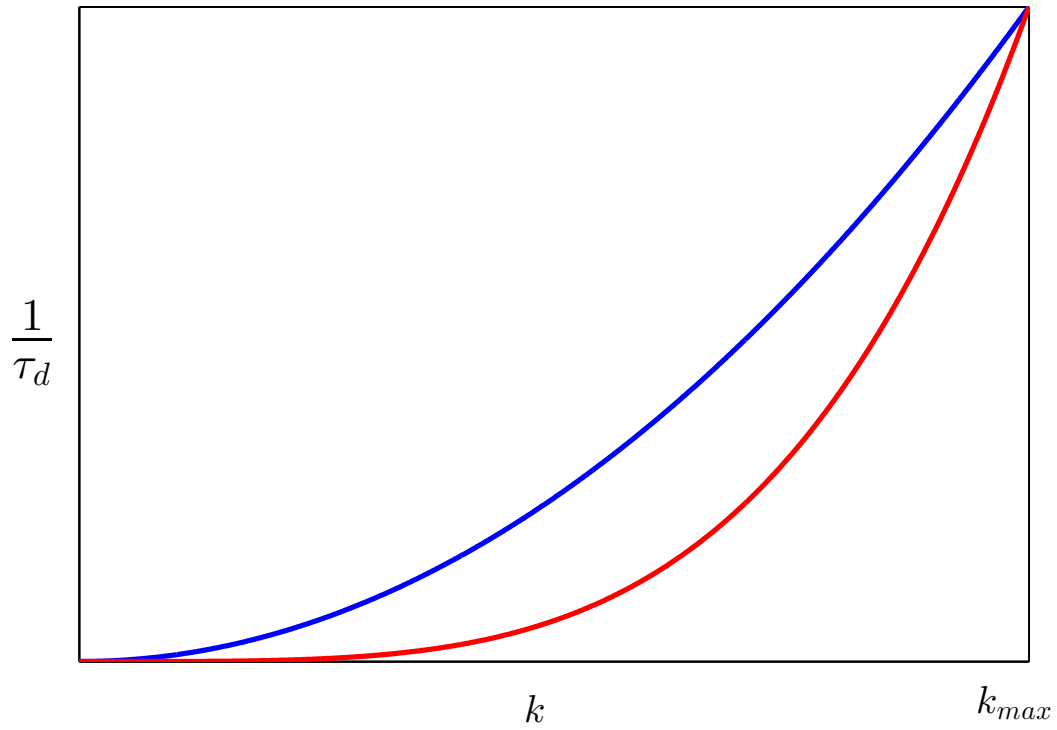Figure 3.6: The inverse diffusion times, $1/\tau_d$, of the wavenumbers for the regular viscosity, blue, and the hyperviscosity case, red. The hyperviscosity inverse diffusion times are lower then the regular viscosity case, corresponding to longer diffusion times. This has the effect of simulating larger Reynolds numbers. Note that the hyperviscosity coefficient is chosen such that at k_{max} the two cases coincide.

of the perturbations, we obtain the following set of linear equations for the perturbations

$$\frac{\partial \tilde{\boldsymbol{u}}}{\partial t} + \omega_{z0}\hat{\boldsymbol{e}}_z \times \tilde{\boldsymbol{u}} + \tilde{\boldsymbol{\omega}} \times \boldsymbol{u}_{h0} = -\nabla(\tilde{p} + \boldsymbol{u}_{h0} \cdot \tilde{\boldsymbol{u}}) - \tilde{\rho}'\hat{\boldsymbol{e}}_z + \frac{1}{Re}\nabla^2\tilde{\boldsymbol{u}}, \qquad (3.73)$$

$$\nabla \cdot \tilde{\boldsymbol{u}} = 0, \qquad (3.74)$$

$$\frac{\partial \tilde{\rho}'}{\partial t} + \boldsymbol{u}_{h0} \cdot \nabla_h \tilde{\rho}' - \frac{1}{F_h^2}\tilde{w} = \frac{1}{ScRe}\nabla^2\tilde{\rho}', \qquad (3.75)$$

where $\tilde{\boldsymbol{\omega}} = \nabla \times \tilde{\boldsymbol{u}}$.

To justify ignoring the diffusion of the basic state, we used the full nonlinear code, which will be discussed below, with the same Lamb-Chaplygin dipole initial state and no perturbation, and let it diffuse out. We found that over 50 time units, the total kinetic energy decreased by about 10%, and hence we are justified in ignoring the viscous diffusion of the basic state. As we shall see in the next chapters, the timescales of the instability are much smaller than the diffusive time scales. Thus, in our simulations, the diffusion of the basic state is negligible over the time scales of the instability.

As stated above, the Lamb-Chaplygin dipole is oriented vertically. As a result we can separate the dependence of the perturbation the vertical and horizontal directions as

$$[\tilde{\boldsymbol{u}}, \tilde{p}, \tilde{\rho}'](x, y, z, t) = [\boldsymbol{u}, p, \rho'](x, y, t)e^{ik_z z} + \text{c.c.}, \qquad (3.76)$$

where c.c. is the complex conjugate. From here we can now take the 2D Fourier transform and recall the projection operator $\mathbf{P}(\mathbf{k})$, with components $P_{ij}(\mathbf{k}) = \delta_{ij} - k_i k_j/k^2$ to eliminate pressure, to obtain a set of equations for the Fourier coefficients

$$\frac{\partial \hat{\boldsymbol{u}}}{\partial t} = \mathbf{P}(\mathbf{k})[\widehat{\boldsymbol{u} \times \omega_{z0}\hat{\boldsymbol{e}}_z} + \widehat{\boldsymbol{u}_{h0} \times \boldsymbol{\omega}} - \hat{\rho}'\hat{\boldsymbol{e}}_z] - \frac{k^2}{Re}\hat{\boldsymbol{u}}, \qquad (3.77)$$

$$\frac{\partial \hat{\rho}'}{\partial t} = -i\boldsymbol{k}_h \cdot \widehat{\boldsymbol{u}_{h0}\rho'} + \frac{1}{F_h^2}\hat{w} - \frac{k^2}{ScRe}\hat{\rho}', \qquad (3.78)$$

where k_z, Re, Sc, F_h are input parameters, $\boldsymbol{k}_h = (k_x, k_y)$ is the horizontal wavenumber and $k^2 = k_x^2 + k_y^2 + k_z^2$ is the total wavenumber.

To numerically solve (3.77) and (3.78), we use a spectral transform method to evaluate derivatives, with 2/3-rule de-aliasing and second order Adams-Bashforth for time-stepping. Each simulation was initialised with a random field and integrated over an $N \times N$ grid for 100 time units to determine the behaviour of the fastest growing mode. After several time units, the leading eigenmodes for $\boldsymbol{u}, \rho$ behave exponentially (e.g. Billant and Chomaz [11])

$$\boldsymbol{u}, \rho \propto C(x, y)e^{\sigma t}, \qquad (3.79)$$

48

and we can obtain the largest growth rate by the formula

$$\sigma = \lim_{t\to\infty} \frac{1}{2}\frac{d\ln E}{dt}, \tag{3.80}$$

where σ is the real growth rate of the mode and E is the kinetic energy $\frac{1}{2}(u^2 + v^2 + w^2)$. This follows directly from the exponential behaviour of the leading eigenmode. The energy behaves as

$$E \sim \frac{3}{2}C(x,y)^2 e^{2\sigma t} \Rightarrow \ln E = \ln(3C^2/2) + 2\sigma t, \tag{3.81}$$

and upon taking the time derivative of both sides yields the desired result. To obtain the energy, we use Parseval's theorem which relates the real space energy to the sum of the squares of the Fourier coefficients. Thus the total kinetic energy is obtained by summing the squares of the Fourier transform of the velocities over all wavenumbers.

To evaluate σ, we compute the average value of the growth rate from the later portion of the time series. Initially, there is transient behaviour where the various modes are all growing and none dominant. After $t = 20$, after the initial transient behaviour has died out and the leading mode dominants in all the cases observed. In the case of an oscillatory growth rate, as considered in [8], we drop the assumption that σ is real and instead compute the growth rate from

$$\sigma_r = \lim_{t\to\infty} \frac{1}{2T}\ln\left(\frac{E(t+T)}{E(t)}\right), \tag{3.82}$$

where T is the period of the oscillatory mode. The imaginary growth rate is given as $\sigma_i = 2\pi/T$. As above, we compute σ from the time series beginning at $t = 20$, however we first measure the period T from roughly 10 oscillations, and then compute the average.

Chapter 4

Linear equation simulations

4.1 Introduction

In this chapter we extend the results of Billant and Chomaz [11] to the sub-buoyancy length-scales. We also reproduce the numerical results presented by Billant and Chomaz and confirm their conclusions about the existence of the zigzag instability at the buoyancy scale. The results in this chapter are based on the paper by Bovard and Waite [13] which focused on the short-wave instability. More background information has been included in this chapter.

4.2 Set-up

The equations that we want to solve are the linear Boussinesq equations, which we derived in Chapter 2 and for which we derived the numerical scheme in Chapter 3. We repeat the equations here:

$$\frac{\partial \hat{\boldsymbol{u}}}{\partial t} = \mathbf{P}(\mathbf{k})[\widehat{\boldsymbol{u} \times \omega_{z0}}\hat{\boldsymbol{e}}_z + \widehat{\boldsymbol{u}_{h0} \times \boldsymbol{\omega}} - \hat{\rho}'\hat{\boldsymbol{e}}_z] - \frac{k^2}{Re}\hat{\boldsymbol{u}}, \tag{4.1}$$

$$\frac{\partial \hat{\rho}'}{\partial t} = -i\boldsymbol{k}_h \cdot \widehat{\boldsymbol{u}_{h0}\rho'} + \frac{1}{F_h^2}\hat{w} - \frac{k^2}{ScRe}\hat{\rho}'. \tag{4.2}$$

The parameter regime to be explored is a function of k_z, Re, F_h.

In our simulations, we investigate a range of Reynolds numbers $Re = 5000 - 20{,}000$ and Froude numbers $F_h = 0.05 - 0.2$. These numbers have been chosen to be within the range

Re	F_h	Δt	k_z
10,000	∞	0.000950	1-220
20,000	0.2	0.000950	1-160
10,000	0.2	0.000950	1-160
5000	0.2	0.000950	1-160
2000	0.2	0.000950	1-160
20,000	0.1	0.000375	1-160
10,000	0.1	0.000375	1-160
5000	0.1	0.000375	1-160
2000	0.1	0.000375	1-160
20,000	0.05	0.000375	1-140
10,000	0.05	0.000375	1-140
5000	0.05	0.000375	1-140
2000	0.05	0.000375	1-140

Table 4.1: Overview of the numerical parameters.

of the results of Billant and Chomaz [11]. Additionally, these parameters are within the range of potential experimental studies using techniques of Billant and Chomaz [9]. For each F_h and Re a wide range of vertical wavenumber, k_z, were investigated with k_z ranging from 1 to 200. This wavenumber range incorporates the scale of the zigzag instability down to the viscous damping scale. We additionally consider the Schmidt number to be unity, following the main results of Billant and Chomaz [11]. In order to compare with experiments, Billant and Chomaz investigated a non-zero Schmidt number, however their numerical work mainly focused on $Sc = 1$ and thus we do not consider different Schmidt numbers here.

For our simulations a box size of $L = 9$ with $N = 512$ grid points was used. The reason for choosing $L = 9$ was to minimise interactions of the fields with themselves across the periodic boundary. Domain sizes of $L = 5$ have been used in practice [3], however we erred on the side of caution and repeated the box size conditions of Billant and Chomaz [11]. For robustness results were checked at smaller box size and agree with the tests of [11]. The parameters for our simulations are summarised in Table 4.1. These were chosen following Billant and Chomaz [11].

The code was written in Fortran and all the FFTs were done by FFTW V3.0 [26] and was tested by comparing the growth rates given by Billant and Chomaz in [11], specifically their Figure 1 and Tables 1 and 2. Unlike Billant and Chomaz [11] we did not restart each simulation with the previous eigenmode which allowed us to use a serial farming par-

allel approach for evaluating multiple k_z simultaneously as we did not need the previous wavenumber eigenmode to initialise the simulation. The trade-off is the individual simulations had to be run longer but they could be done in parallel allowing for a greater variability in the parameters explored.

4.3 Growth rate

As discussed in Chapter 3, the growth rates are computed by evaluating the time derivative of the energy of the eigenmode. Fig. 4.1 demonstrates two different types of growth rates that are representative of all the growth rate plots for all the simulations. Here we have chosen $F_h = 0.1, Re = 20,000$ and $k_z = 20$ in panel (a) and $k_z = 60$ in panel (b). In both panels, the perturbation initially goes through some transient behaviour which is when the various eigenmodes all grow together and none of have become dominant. After about 20 time units this transient behaviour has died off and the dominant eigenmode has emerged. This 20 time unit delay was observed for all simulations. In panel (a), there is a case of an oscillatory growth rate. As can be observed, the growth rate of this wavenumber is highly oscillatory and thus the true value of the growth rate must be computed using the period of the oscillation. Panel (b) represents the more typical case of the growth being non-oscillatory and quickly settling down onto a certain value.

Using these types of plots of the growth rate, we are able to extract the leading growth rate of the eigenmode with the maximum growth rate by examining the long term behaviour. From these times series, we determined the maximum growth rate of the leading eigenmode for a wide range of wavenumbers, Reynolds numbers, and Froude numbers. The growth rate curves for a given F_h and Re can be plotted by determining this maximum growth rate for each vertical wavenumber. Following Billant and Chomaz [11], we scale the vertical wavenumber by F_h to obtain $k_z F_h$. This is, in our units, the vertical wavenumber scaling by the buoyancy scale $L_b = U/N$. Recall that k_z has been non-dimensionalised by R, i.e. $k_z = k'_z R$ where k'_z is the dimensional wavenumber with units of inverse length. So the dimensionless $F_h k_z$ would become $F_h k'_z R$ in dimensional units, k'_z denoting the dimensional vertical wavenumber. Re-writing this we obtain $F_h k'_z R = k'_z U/N = k'_z L_b$, using the definition of the Froude number, and hence dimensional $F_h k'_z R = k'_z L_b$.

Fig. 4.2 shows the largest eigenmode growth rate as a function of vertical wavenumber for fixed F_h and Re for a wide range of F_h and Re. The qualitative behaviour for the growth rates at different Reynolds numbers are very similar to one another. We now investigate the various regimes in some detail.
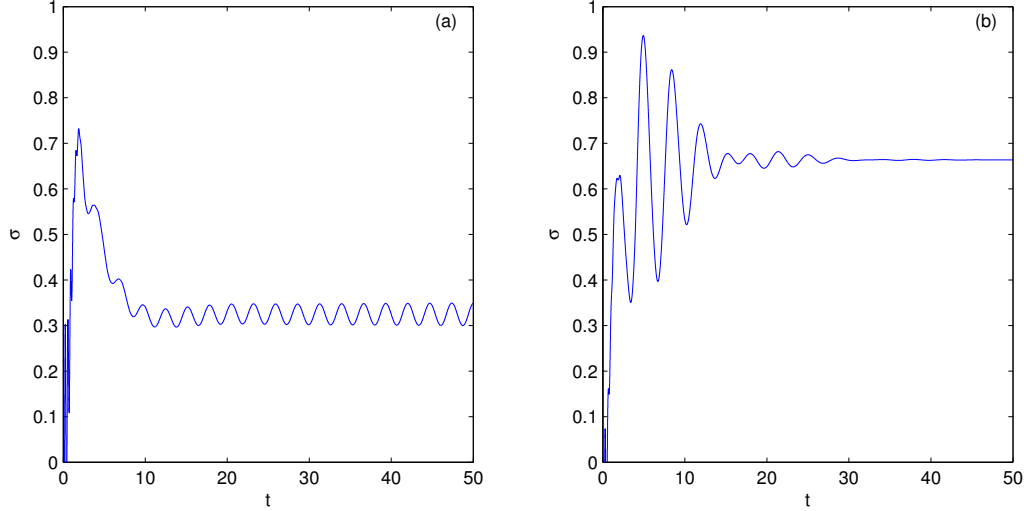
Figure 4.1: Time series of the growth rate, obtained from the derivative of the energy, for $F_h = 0.1$ and $Re = 10,000$. Panel (a) is $k_z = 20$ and Panel (b) is $k_z = 60$.

At small $F_h k_z$, the growth rate reaches a local maximum, the zigzag peak, as predicted by Billant and Chomaz [9, 10, 11]. As discussed in Chapter 2 the zigzag instability appears at the buoyancy wavelength L_b. It is clear from the figure where we see the peak growth rate occurs at the same $F_h k_z$, here roughly $F_h k_z \approx 0.6$. In panels (a) and (b) it is especially clear that the growth rate curves all collapse onto each other and have almost identical growth rates regardless of Reynolds number, confirming the results of the prediction of Billant and Chomaz [10, 11]. Panel (c) has similar growth rates for $Re = 20,000, 10,000$, and 5000 but for $Re = 2000$ the growth rate is a bit lower. Despite the slight difference in growth rates, they do all occur at the same $k_z F_h$. The lower growth rates of the $Re = 2000$ cases suggests that diffusion is playing an important role and is damping out the instability, as can be seen by the rapid decrease in the growth rate of the curve. Since the theoretical results of Billant and Chomaz [10] were conducted in an inviscid regime, it is not unexpected to observe a breakdown of this assumption. Some numerical experiments were run at even lower Froude number, but here the diffusion was dominating and the growth rate curves were dropping off very rapidly near the zigzag peak and thus even obscuring the zigzag peak. Thus for $F_h < 0.05$ and $Re < 10,000$ we find that the sub-buoyancy length scales are being diffused out.

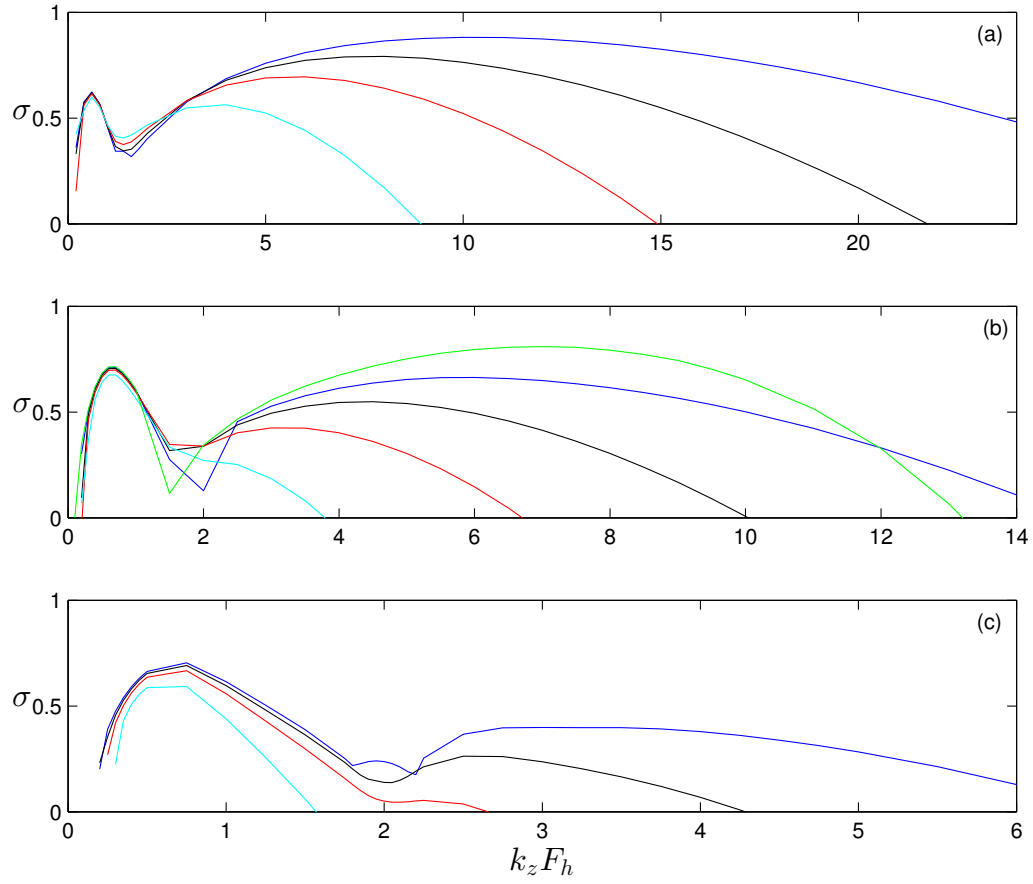For k_z increasing beyond the zigzag peak, the growth rate then decreases for increasing

Figure 4.2: Growth rate σ as a function of $k_z F_h$ for fixed $F_h = 0.2$ (a) , 0.1 (b), 0.05 (c) with Re= 2000 (cyan), Re= 5000 (red), Re= 10,000 (black), Re= 20,000 (blue). In panel (b) the green line is the hyperviscosity case with $Re = 20,000$.
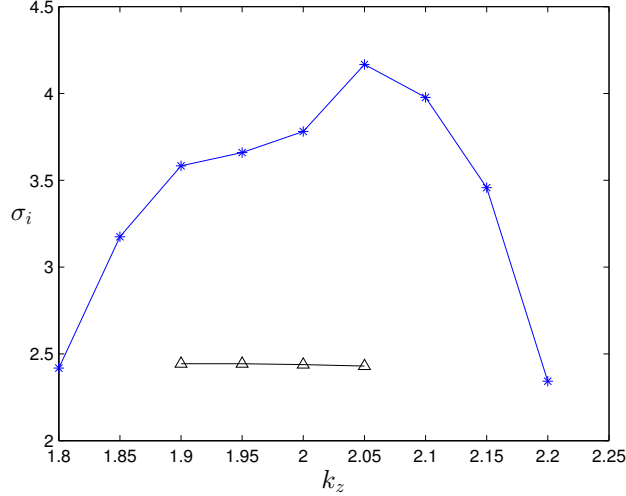
Figure 4.3: Frequency of the growth rate for $F_h = 0.05$ and $Re = 20{,}000$ (blue) and $Re = 10{,}000$ (black).

$F_h k_z$ to a local minimum before increasing to a second local maximum. At this local minimum oscillatory growth rates are observed. The imaginary part of the growth rate, the frequency, σ_i remains zero everywhere else except in this small region between the two local maxima, with the exception of very small $k_z F_h$. Oscillatory growth rates are also observed in this small wavenumber regime, as observed in [8] and we did not explore this regime further. Fig. 4.3 displays the frequency growth rates for $F_h = 0.05$ and $Re = 10{,}000$ and 20,000. The frequency growth rate for $Re = 10{,}000$ is a straight line but such a trend is not observed for $Re = 20{,}000$. The shape of this curve, when it did appear, depended highly on the Reynold and Froude number, and did not suggest any sort of general result that could be determined about the frequency growth rate. Additionally, the range of this oscillatory instability also depended on the Reynolds and Froude numbers and also did not suggest any sort of general result.

After this local minimum, the growth rate increases to a secondary maximum. We will discuss this maximum further below. Continuing to even smaller vertical scales, viscous effects increase and may damp out the instability, and hence the growth rate decays with increasing $k_z F_h$ in the limit of large $k_z F_h$.

For $F_h = 0.2$ (Fig. 4.2a), the peak growth rate of the short-wave instability exceeds that of the zigzag instability for increasing Reynolds numbers. The growth rates at the second

55

peak is smaller for $F_h = 0.1$ (Fig. 4.2b), but they continue to increase with increasing Re. For $F_h = 0.05$ (Fig. 4.2c), the second peak is weaker than the zigzag peak. Fig. 4.4 shows the growth rate for fixed Reynolds numbers with varying Froude numbers. Examining the case of $Re = 20,000$ (Fig. 4.4a), the growth rate at the second peak increases with increasing Froude. A similar result is observed for $Re = 10,000$ and 5000 (Fig. 4.4b-c). $Re = 2000$ is not included because viscous effects have damped out the second peak in this case. Overall, the dependence of the short-wave growth rate on Froude is also more pronounced than that of Reynolds. For example, the growth rate of the second peak at fixed $Re = 20,000$ (Fig. 4.4a) doubles from $F_h = 0.05$ to $F_h = 0.2$. By contrast, at fixed $F_h = 0.2$ (Fig. 4.2a), the increase in the growth rate from $Re = 5000$ to $Re = 20,000$ is only about 25% larger.

The above analysis demonstrates that the short-wave growth-rate peak moves to larger $k_z F_h$ with increasing F_h and increasing Re, but has a stronger dependence on Froude than Reynolds. Some of this joint dependence can be explained by examining the dependence on the buoyancy Reynolds number $Re_b = F_h^2 Re$ [15, 28, 52]. In stratified turbulence, the buoyancy Reynolds number is analogous to the Reynolds number in the viscous term due to the vertical gradients [15]. Recall from the scaling analysis in Chapter 2, that the vertical diffusion term has a scale-factor of $Re\delta^2$. At the buoyancy length scale, this can be rewritten as ReF_h^2 and has been found to be an important dimensionless parameter in stratified turbulence [15]. As k_z increases, we move to smaller vertical scales where the vertical viscosity terms, controlled by the buoyancy Reynolds number, dominates, so it follows that the second peak may be governed by Re_b. In Fig. 4.5 the location of the second peak from Fig. 4.2 is plotted as a function of the buoyancy Reynolds number. The peak location line is approximately linear and can be fitted with the curve $k_z F_h = Re_b^{2/5}$, which is plotted. This scaling implies that the vertical wavenumber, k_z, of the short-wave instability is approximately

$$k_z \sim F_h^{-1/5} Re^{2/5}. \tag{4.3}$$

The dependence of the growth rate on $k_z F_h$ appears to be similar in the cases with different F_h and Re but the same Re_b. Fig. 4.6 demonstrates the similarity of the growth rate plotted against $k_z F_h$ for two cases with $Re_b = 500$ and two cases with $Re_b = 50$. For both cases, the locations of the zigzag and second peak line up quite well. The difference between the red and blue curves at the second peak is 4% for $Re_b = 200$ and 6% for $Re_b = 50$, a reasonable variation.

In Fig. 4.2 (b) the green curve corresponds to a hyperviscosity run with $Re = 20,000$, which has $Re_h = 2.8 \times 10^8$. The motivation for using hyperviscosity is to capture the higher-Reynolds number regime by restricting dissipation to only the largest wavenumbers. As
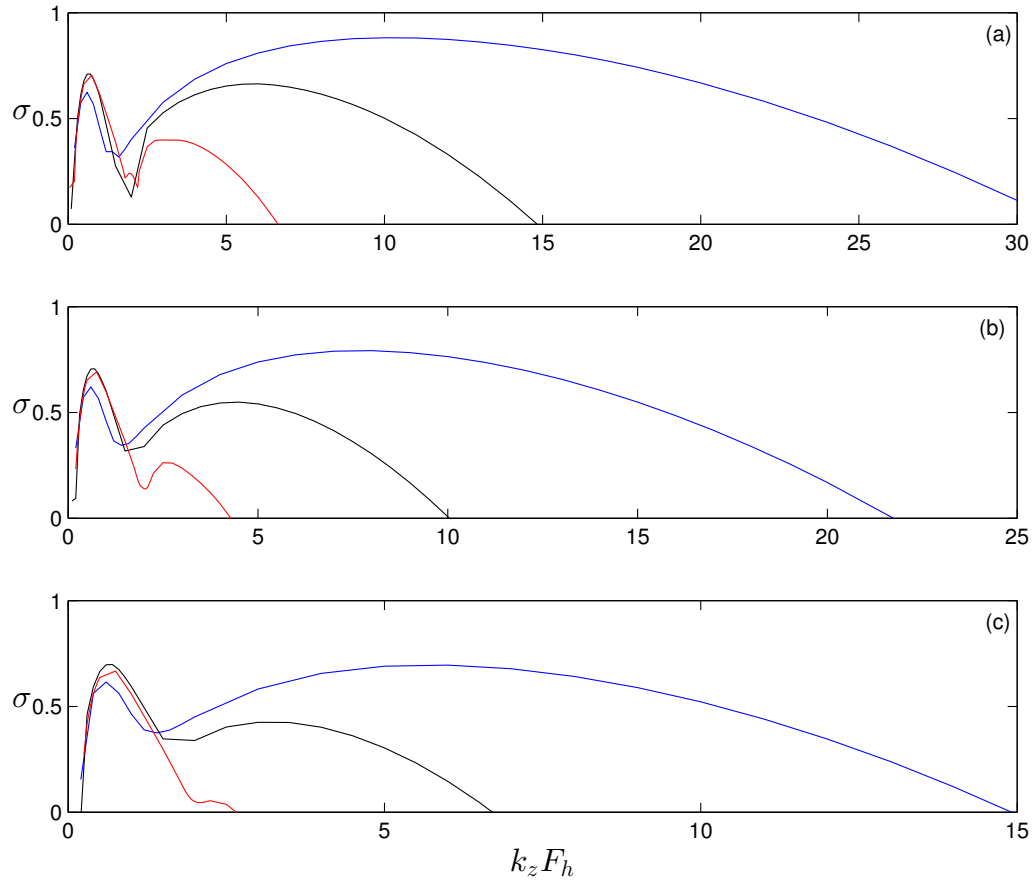
Figure 4.4: Growth rate σ as a function of $k_z F_h$ for fixed $Re = 20,000$ (a) , 10,000 (b), 5000 (c), with $F_h = 0.05$ (red), $F_h = 0.1$ (black), $F_h = 0.2$ (blue).
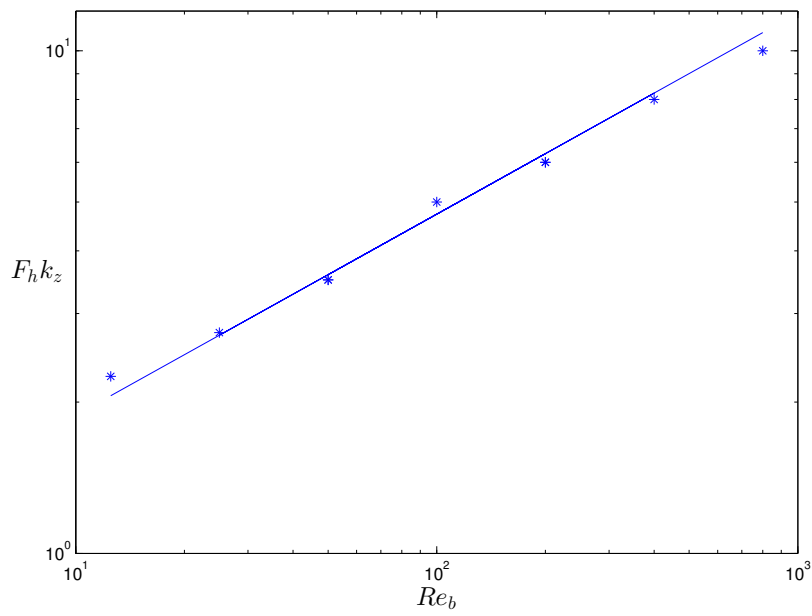
Figure 4.5: The location of the second peak as a function of the buoyancy Reynolds number Re_b. $k_z F_h$ is taken from Fig. 4.2. The straight line is $Re_b^{2/5}$.
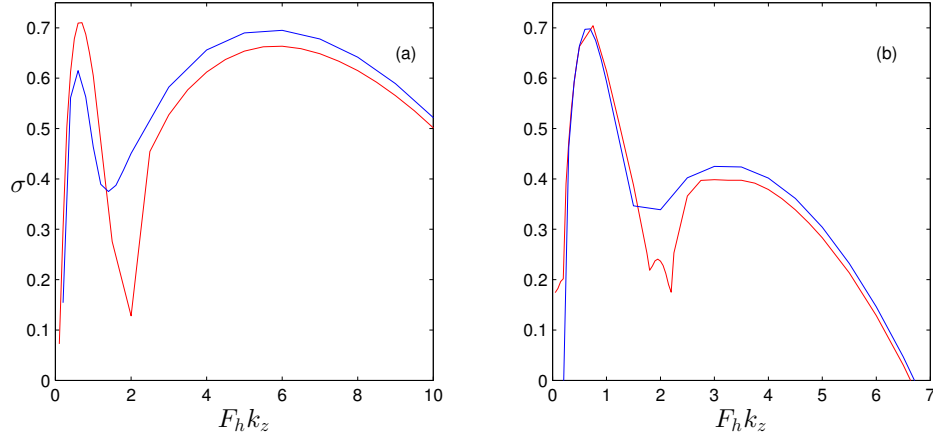
Figure 4.6: Growth rate σ as a function of $F_h k_z$ for fixed Re_b. In (a), red is $Re = 20{,}000, F_h = 0.1$ and blue is $Re = 5000, F_h = 0.2$, both corresponding to $Re_b = 500$; in (b) red is $Re = 20{,}000, F_h = 0.05$ and blue is $Re = 5000, F_h = 0.1$, both corresponding to $Re_b = 50$.

the hyperviscosity run demonstrates, the zigzag peak is independent of Reynolds number and the existence of the peak would be expected at higher Reynolds numbers. For the second peak, we note that the growth rate of the hyperviscosity run exceeds that of $Re = 20{,}000$ for $k_z F_h > 3$ and reaches a maximum around $k_z F_h = 7$. The maximum growth rate in the hyperviscosity case is around 25% larger than the regular viscosity case with $Re = 20{,}000$. At $k_z F_h = 12$ we see the hyperviscosity and non-hyperviscosity curves cross. This intersection corresponds to the horizontal wavenumber at which the hyperviscosity damping rate equals the regular viscous damping rate for $Re = 20{,}000$. For k_z greater than this maximum, the hyperviscosity operator experiences greater damping than the regular viscosity, which can be seen by the sudden drop off of the growth rate. This simulation presents evidence that as $Re \to \infty$, the growth rate of the second peak will the same order as, or larger than, the growth rate of the zigzag instability.

4.4 Structure

Briefly, we discuss the structure of the zigzag instability. Fig. 4.7 demonstrates the vertical vorticity of the zigzag peak for $F_h = 0.2, 0.1, 0.05$ and $Re = 20{,}000$. In all vertical vorticity
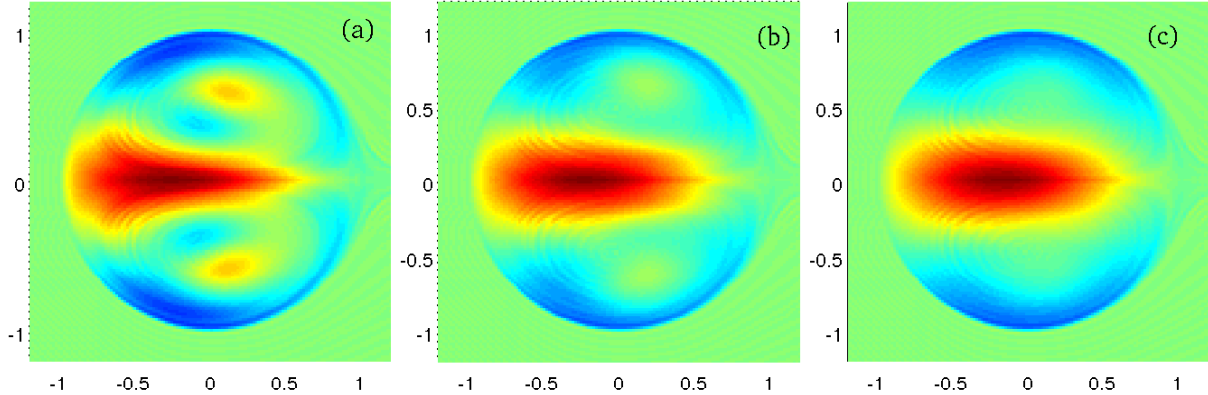
59

Figure 4.7: Perturbation vertical vorticity ω_z at the zigzag peak for $F_h = 0.2$ (left), 0.1 (middle) , 0.05 (right) and $Re = 20{,}000$.

plots that follow, we have normalised the plots so red represents the maximum velocity or vorticity and blue represents the minimum velocity or vorticity. Since the vorticity field is real, we have chosen the real part. Only $Re = 20{,}000$ has been included, since the structure is nearly identical for $Re = 10{,}000$ and 5000. This confirms the assumption made by Billant and Chomaz [10] that the zigzag peak emerges at the buoyancy scale U/N independent of Re. A detailed study of the structure of the zigzag instability is done by Billant and Chomaz [11].

The minimum between the zigzag and short-wave instability is the oscillatory minimum. Fig. 4.9 and Fig. 4.10 are the vorticity and velocity fields respectively at the oscillatory minimum. Following Billant and Chomaz [11] we only plot the real part of the velocity fields. In the vorticity structure, for $Re = 20{,}000$ the structure is much more defined than the smoothed out structure of the zigzag instability. At $F_h = 0.2$, (a),(d),(g) , the vorticity is in thin strips around the dipole. At at $F_h = 0.1$, panels (b),(e),(h), new structure has emerged in the core of the dipole and has a swirl-like pattern. At the $F_h = 0.05$, (c),(f),(i), this structure has become much more detailed and a swirl-like pattern has clearly emerged. Additionally, as we increase the viscosity, this swirl-like structure becomes more diffused out.

Fig. 4.11 and Fig. 4.12 show the spatial structure of the perturbation vertical vorticity and fields at the second peak for different Re and F_h. Qualitatively, we observe greater variation for different Froude numbers versus different Reynolds number as suggested above.
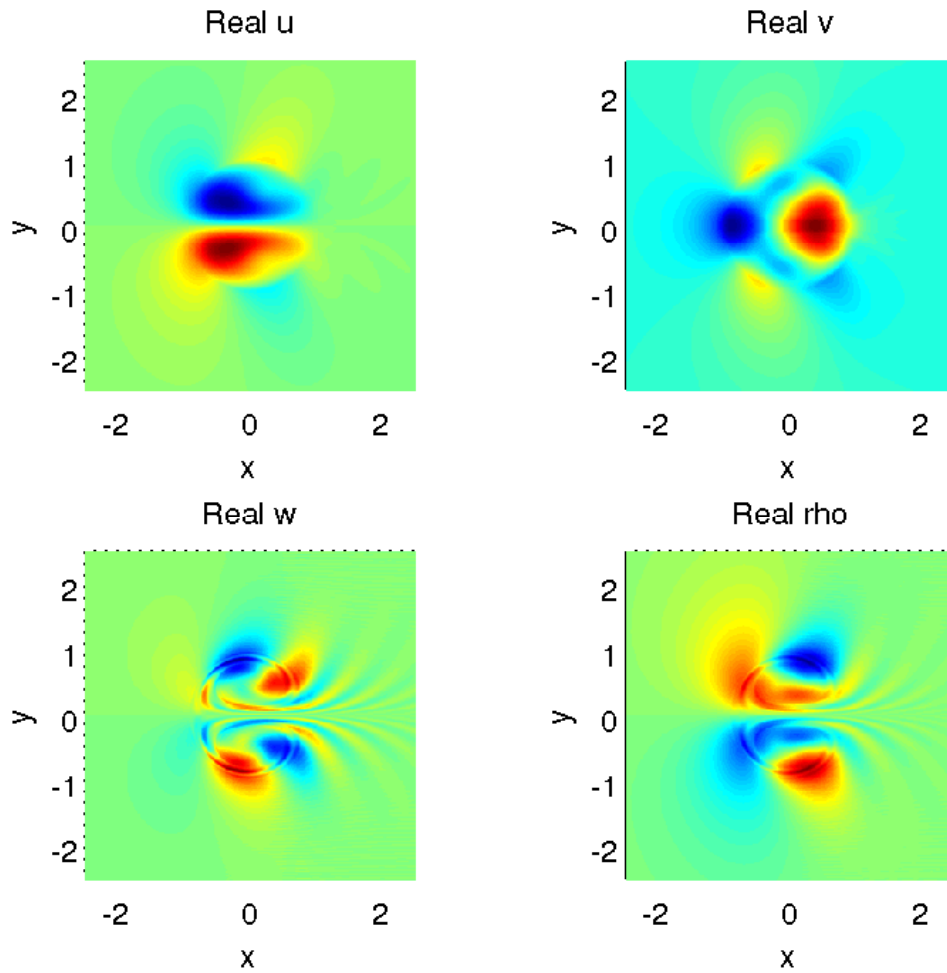
Figure 4.8: Perturbation fields u, v, w, ρ at the zigzag peak for $F_h = 0.1$ and $Re = 20{,}000$. Here $k_z = 6$.

Figure 4.9: Perturbation vertical vorticity ω_z at local oscillatory minimum for $Re = 20{,}000$ (top) , 10,000 (middle) , 5000 (bottom); and $F_h = 0.2$ (left) , 0.1 (middle) , 0.05 (right).

Figure 4.10: Perturbation fields u, v, w, ρ at the oscillatory minimum for $F_h = 0.1$ and $Re = 20{,}000$. Here $k_z = 20$.

Figure 4.11: Perturbation vertical vorticity ω_z at the short-wave peak for $Re = 20,000$ (top), 10.000 (middle), 5000 (bottom) ; and $F_h = 0.2$ (left) , 0.1 (middle) , 0.05 (right).
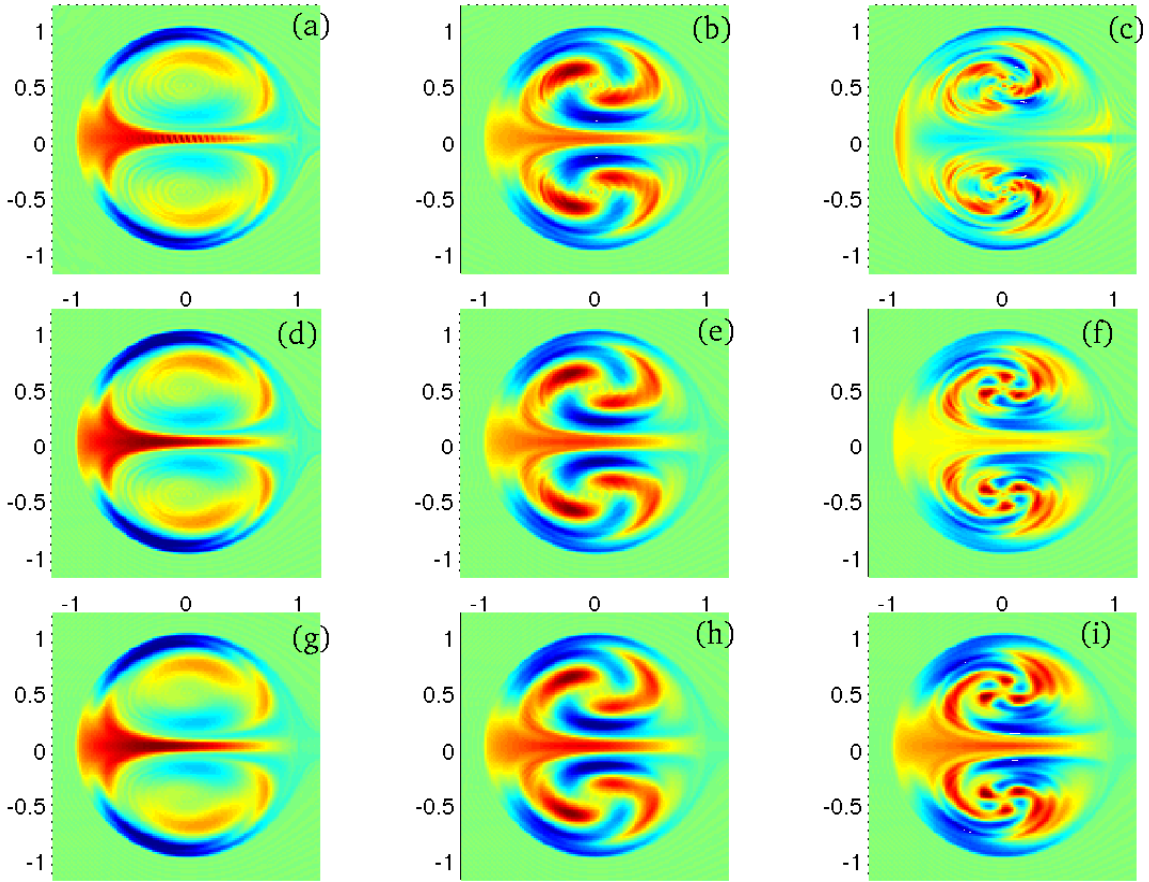
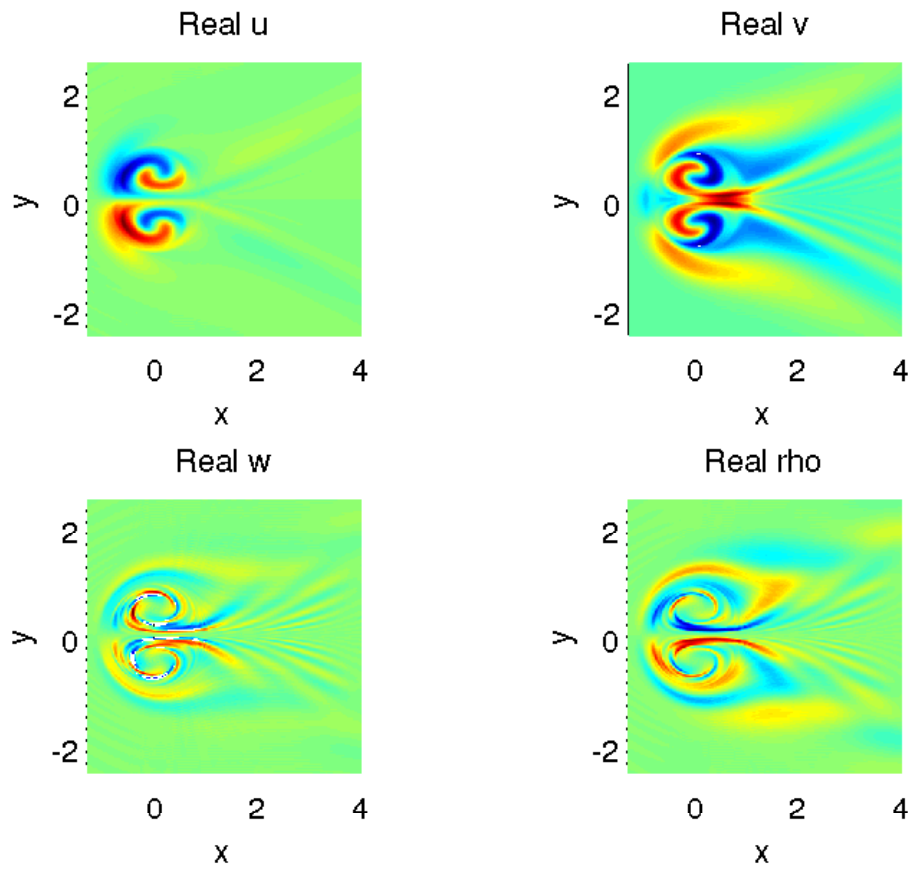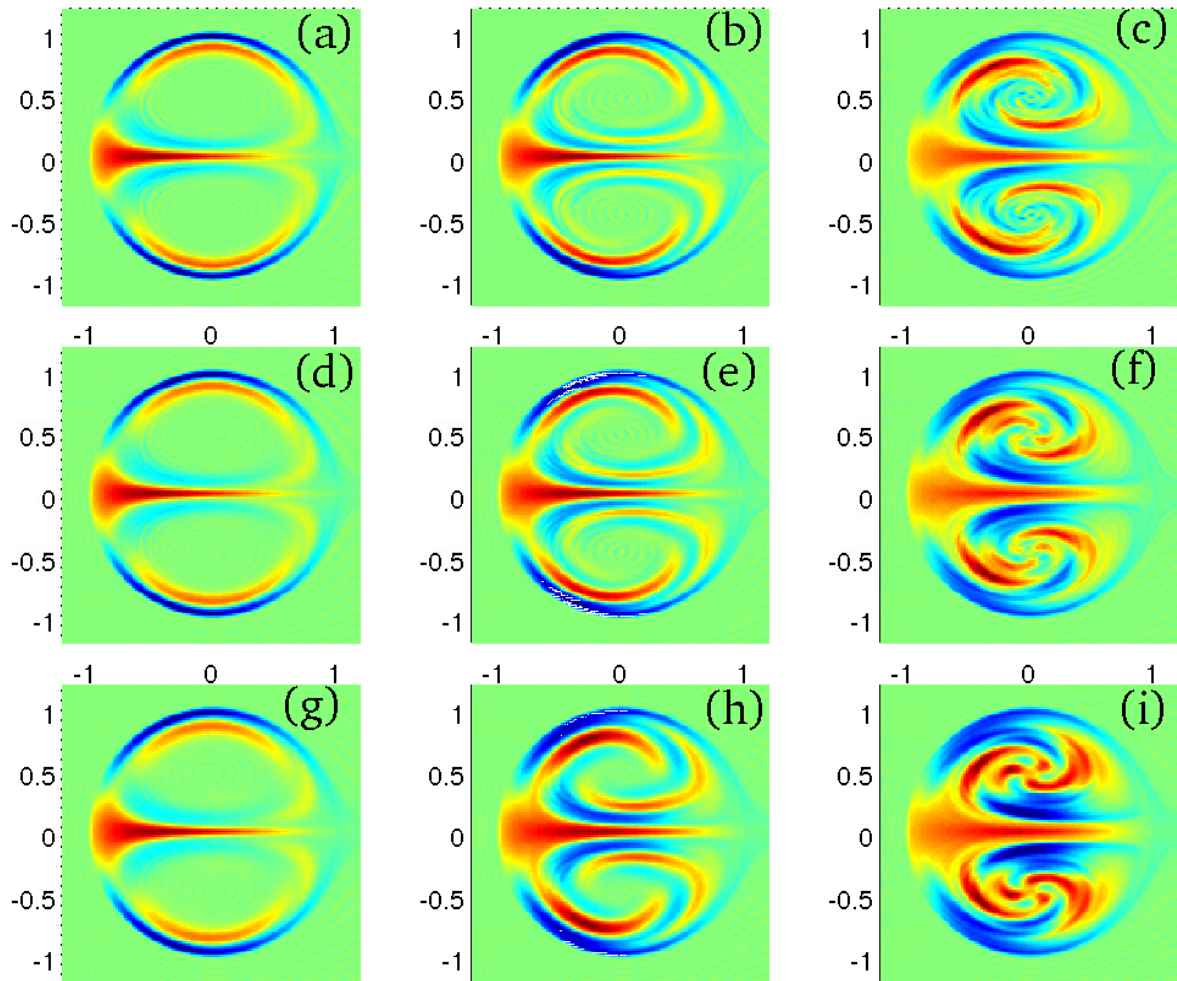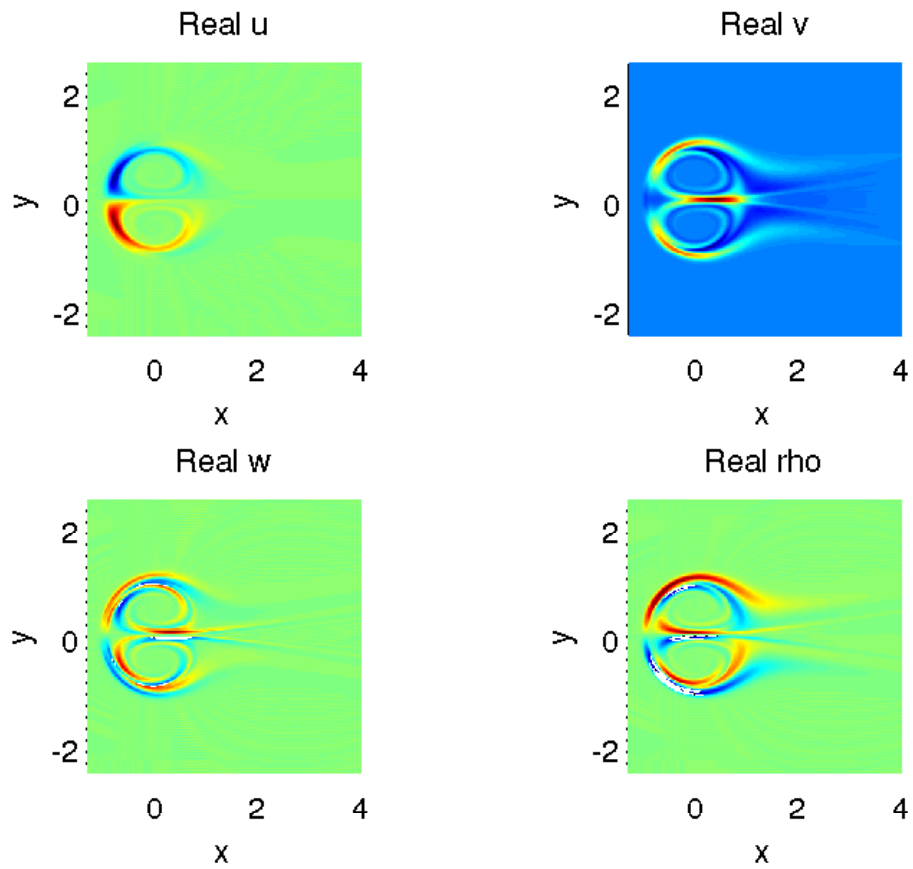Figure 4.12: Perturbation fields u, v, w, ρ at the short-wave instability for $F_h = 0.1$ and $Re = 20{,}000$. Here $k_z = 60$.
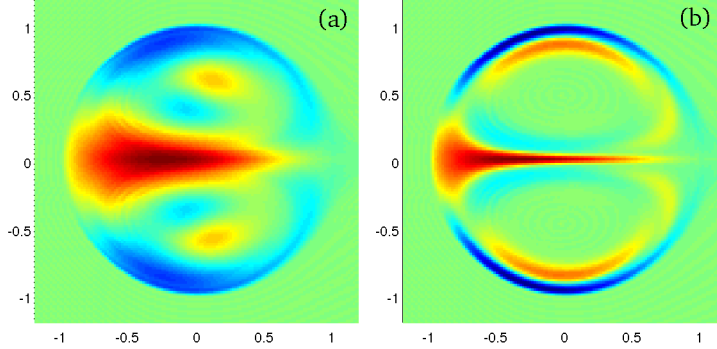
Figure 4.13: Perturbed vertical vorticity ω_z at (a) the zigzag peak (b) the second peak for $Re = 5000, F_h = 0.2$.

At the largest Froude number, the perturbation vorticity is organised in thin strips around and inside the dipole core between the two vortices. Panels (b),(e),(h) have $F_h = 0.1$ and have a similar overall structure to the larger Froude number. Here, in the cores of the vortices, there is an emergence of a swirl-like pattern. At lower Reynolds number, the structure is spread out due to diffusion, while at higher Reynolds number, small-scale structure is beginning to emerge. This trend continues overall as we move to lower Froude numbers.

Examining Figs. 4.11 (g)-(i) (fixed Re and decreasing F_h), the core of the dipoles has a twisting-like behaviour as the Froude number decreases. From this we can conclude that the instability structure of the second peak depends more on the Froude number than on the Reynolds number, which again reinforces the buoyancy Reynolds number scaling. Indeed, if we consider the cases with $Re_b = 50$ and 200 as above, which correspond to Fig. 4.11 (b),(g) and (c),(h) respectively, we can see similar structure in the vorticity fields. Additionally, the anti-symmetric structure of the perturbation can be observed in the dominant eigenmodes in all cases, as found by [8, 11].

Fig. 4.13 shows the perturbation structure for the zigzag peak (a) and the short-wave peak (b) for the case of $Re = 5000, F_h = 0.2$. This case was chosen because the growth rates of the two wavenumbers is roughly the same (see Fig 4.2 a). The zigzag instability exhibits a quadrupole vorticity structure as discussed in [11], which corresponds to a bend and a twist of the basic state dipole. The short-wave instability shares some common overall structure with the zigzag instability. Both have a line of vorticity centred in between two Lamb-Chaplygin vortices and have a ring of negative vorticity around the outer edges of

66

the dipoles. Additionally, the number of local maxima and minima remains the same. However, in the short-wave instability, these bands of vorticity have been squeezed into thinner strips and are much more localised along the outer edges of the vortices. In the cores of the dipoles, there is almost no structure and we do not see a quadrupole moment. The full vorticity field of the short-wave instability has a much more dominant twist then the zigzag instability and the bending of the dipole is reduced. As the stratification is increased, this behaviour continues but there is a significant emergence of structure within the cores of the vortices, as observed in Fig 4.11.

Fig. 4.14 demonstrates the structure of the v component of velocity for $F_h = 0.1$ and $Re = 20{,}000$ for a range of wavenumbers. Here the transition from the zigzag peak, through the oscillatory minimum to the short-wave instability is explicit. Initially the structure has a large positive and negative velocity but as we increase k_z this positive velocity is stretched forward and flattened out and becomes stretched out in the middle of the velocity field. The initial negative velocity simply dies out. The initial small areas of positive velocity in front of the dipole undergo an interesting evolution and become larger and stretched out wrapping around the back of the dipole and become very thin. The small initial negative velocity also becomes stretched out but instead forms a v-like shape behind the dipole. The evolution of this wake looks quantitatively similar to the wake of a boat through water. Fig. 4.15 is a loglog plot of the angle of this wake as a function of the perturbation wavelength. The red line is a reference slope of $k = 1$ and suggests the relationship between the angle and the wavenumber to be

$$\theta \sim \frac{1}{k_z}. \tag{4.4}$$

An investigation by Sharman and Wurtele [55] found an inverse relationship between the angle of the wake and the vertical wavenumber, similar to our result here. However their stratification set-up is non-constant and is not directly applicable to our constant value stratification. But, their result does suggest that a similar result could be derived for the case of waves behind vortices.

4.5   Subdominant modes

The method we have used so far is limited to only determining the leading eigenmode. An interesting question is whether or not we can determine sub-dominant eigenmodes and what we can learn from these modes. For example, is the same eigenmode dominating at both the zigzag peak and the short-wave peak? To investigate this question, we use a
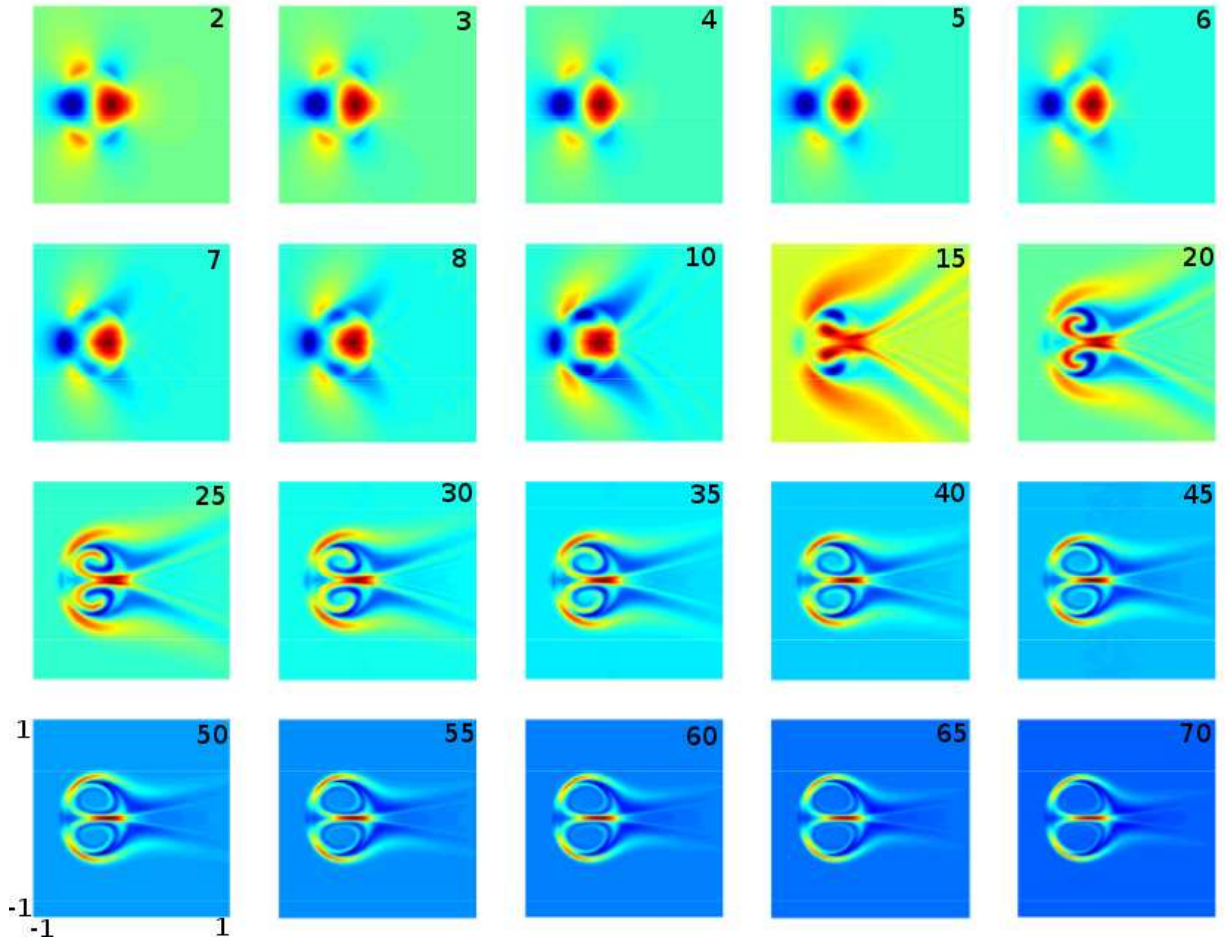
Figure 4.14: Structure of the v velocity from $k_z = 3$ up to $k_z = 110$ for $F_h = 0.1$ and $Re = 20{,}000$. The wavenumber is increasing left to right and top to bottom, with the wavenumber in the top right. Unlike in previous figures, we have not normalised with respect to the maximum vorticity. When a normalisation was applied, the wake behind the dipole was obscured. Here red corresponds to the maximum vorticity and blue the minimum vorticity.
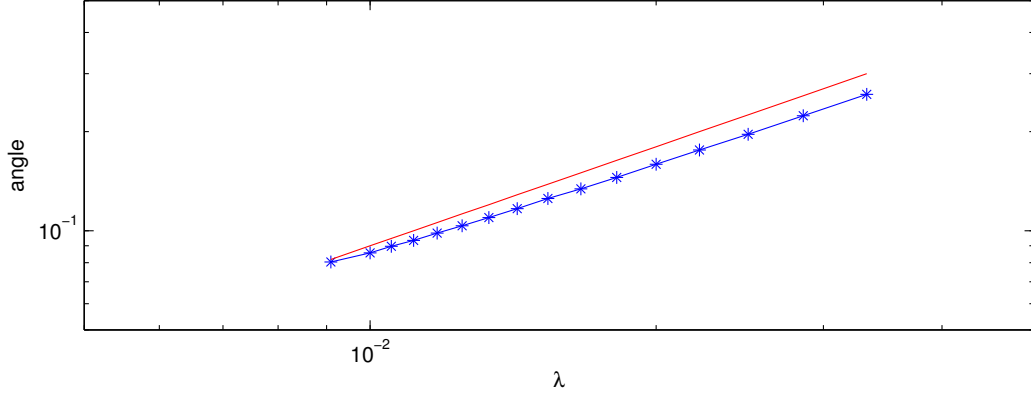
Figure 4.15: Angle of the wake behind the v velocity field as a function of the perturbation wavelength for $F_h = 0.1$ and $Re = 20{,}000$. The red line is a reference slope of 1.

Krylov space method to obtain the growth rates for subdominant modes [25]. Recall that our linear stability problem can be written as

$$\frac{d\boldsymbol{u}}{dt} = A\boldsymbol{u} \tag{4.5}$$

where $\boldsymbol{u} = \boldsymbol{u}(\boldsymbol{x}, t)$ is vector of the unknowns and A is the associated linear operator. We can consider solutions of the form $\boldsymbol{u}(\boldsymbol{x}, t) = \hat{\boldsymbol{u}}(\boldsymbol{x})e^{\sigma t}$, where σ is the growth rate. Substituting in we obtain the following eigenvalue equation for u

$$\sigma\hat{\boldsymbol{u}} = A\hat{\boldsymbol{u}}. \tag{4.6}$$

As mentioned, we have only been trying to find the leading eigenvalue σ but since this is an eigenvalue problem, many algorithms exist to find the eigenspectrum.

   If we want to solve this eigenvalue problem, we must discretise the operator A. For our numerical scheme, we do not explicitly construct this operator because it would get very large. Our code is equivalent to this matrix multiplication if one were to write all the FFTs as a matrix multiplication. Writing out operators this way in practice is unfeasible since for our problem, it would require a matrix that is of size $4N^2 \times 4N^2$ and is very dense. Thus trying to find the eigenvalues using a direct eigenvalue routine is not possible. Instead we investigate other algorithms that can determine the eigenvalues without computing A explicitly.

4.5.1 Krylov eigenvalue routines

One of the simplest and easiest to code algorithms for finding eigenvalues is the power method. It is given by the following iteration [42]

$$u_{k+1} = \frac{Au_k}{|Au_k|}, \sigma_k = \frac{u_k^t A u_k}{u_k^t u_k}. \tag{4.7}$$

The reasoning for this algorithm is very simple. If we suppose that the operator A has a spectrum of eigenvalues such that $\lambda_1 > \lambda_2 > \dots$ then by the spectral theorem we can re-write the operator A as

$$A = \lambda_1 \boldsymbol{u}_1 \boldsymbol{u}_1^T + \lambda_2 \boldsymbol{u}_2 \boldsymbol{u}_2^T + \lambda_3 \boldsymbol{u}_3 \boldsymbol{u}_3^T + \dots \tag{4.8}$$

where $\boldsymbol{u}_i$ is the eigenvector associated with λ_i. Now recall that by the spectral theorem we have the following [42]

$$\left(\frac{A}{\lambda_1}\right)^n = \boldsymbol{u}_1 \boldsymbol{u}_1^T + \left(\frac{\lambda_2}{\lambda_1}\right)^n \boldsymbol{u}_2 \boldsymbol{u}_2^T + \left(\frac{\lambda_3}{\lambda_1}\right)^n \boldsymbol{u}_3 \boldsymbol{u}_3^T + \dots \tag{4.9}$$

and since there is an ordering on the eigenvalues we have that $\lambda_i/\lambda_1 < 1$ and hence as $n \to \infty$ these terms will vanish. Thus if we consider a random initial vector $\boldsymbol{b}_0$ we have that

$$\frac{A^n \boldsymbol{b}_0}{\lambda_1^n} \to \boldsymbol{u}_1 \boldsymbol{u}_1^T \boldsymbol{b}_0, n \to \infty. \tag{4.10}$$

Now in practice we don't have λ_1 but if we replace λ_1 with the norm of $|A^n \boldsymbol{b}_0|$ we can still get a good approximation [42]. By repeated iteration we obtain the scheme from above. This very simple algorithm is able to give us the leading eigenvalue and eigenvector starting from any random initial vector. A rigorous derivation is contained in any good numerical linear algebra book, e.g. Trefethen and Bau [57].

One drawback of this method is that we are throwing away a lot of information at each iteration. It does not seem unreasonable that maybe these previous approximations can tell us something. Utilising this extra information is the key of Krylov methods. First, we define a Krylov sequence to be

$$\{u, Au, A^2 u, \dots, A^{n-1} u\}. \tag{4.11}$$

This definition is just taking the first n iterations of the power method and defining a sequence of them. Likewise we can also define the Krylov matrix as

$$K_n(A, u) = (u|Au|A^2 u| \dots |A^{n-1} u), \tag{4.12}$$

where we are defining a new matrix whose ith column is the i iteration. This Krylov matrix allows us to compute the sub-dominant modes.

Consider the following matrix, $L = K^{-1}AK$, which is the similarity transformation of A by K. Recall that the eigenvalues of similar matrices are the same [42]. This is the key idea of the Krylov methods, if we apply a similarity transform to our original matrix A by K we can instead compute the eigenvalues of L. However we still are stuck with the inverse matrix K^{-1}. To compute this inverse, we orthogonalise K (by the Gram-Schmidt method) and thus $K^{-1} = K^t$.

So far everything has been exact since the size of K must be the same size as A. Now we make the approximation that we can replace K with K_n. Now taking the first n iterations, and n being small in some sense, let us define a new matrix P as above

$$P = K_n^t A K_n. \tag{4.13}$$

Now P is no longer the same size as A. Clearly the similarity properties no longer hold but if the eigenvalues of P are computed, they, rather amazingly, turn out to be a very good approximation to A. This leads to a very simple idea for finding dominant eigenvalues for A: simply choose a small n and then find the eigenvalues of P which is only $n \times n$ and there exist many good algorithms for finding the eigenvalues of small n.

This amazing fact has been fairly well understood for symmetric A and leads to the Lanczos algorithm [42]. The non-symmetric case leads to the Arnoldi iteration [42]. Similar ideas of using Krylov sequences and matrices form the theoretical basis for conjugate gradient and GMRES algorithms for solving linear systems [69].

4.5.2   Results

Fig. 4.16 shows the results from applying the Krylov method for finding sub dominant eigenvalues for the linear stability of a Lamb-Chaplygin dipole in a stratified fluid for $Re = 10,000, F_h = 0.1$ with resolution $N = 256$. The reason $N = 256$ was chosen was for memory issues in MATLAB. Some tests of various sizes of N showed some robustness although a thorough convergence investigation was not completed and the results were only compared to those of the previous sections. To find the Krylov sequence, the output from the simulation of the previous section was saved at n times. This sequence of outputs was then orthogonalised using a Gram-Schmidt procedure and used to form the Krylov matrix K. To evaluate AK the linear code was simulated as normal and reformatted into a giant vector. Then P was constructed and the eigenvalues of the resulting matrix were found using MATLAB's `eigs` routine.
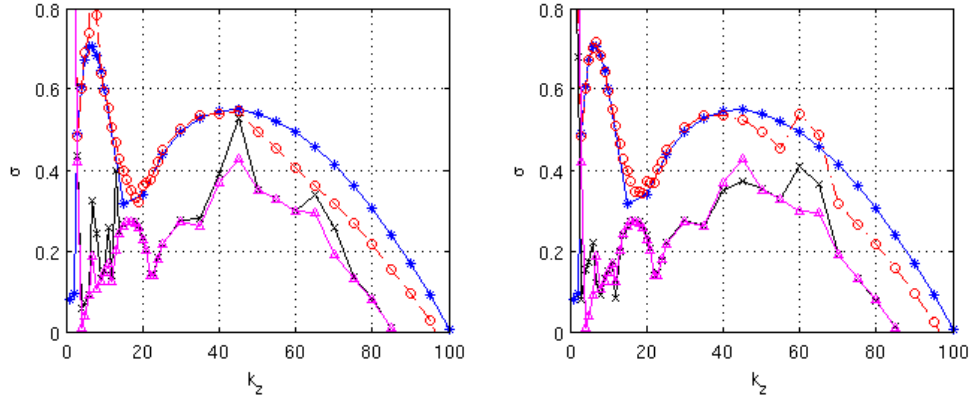
Figure 4.16: Growth rates computed with Krylov methods for two different choices of $n = 50$ (left), 100 (right) for $Re = 10{,}000, N = 256, F_h = 0.1$. Star denotes the dominant eigenvalues from the energy method, circle is the leading approximation from the Krylov method, triangle and x are the second and third eigenvalues respectively.

The results of Fig. 4.16 are somewhat promising. As can be seen, doubling n does improve convergence, although there are still numerical anomalies, such as the random jump in growth rate at $k_z = 60, 65$ for $n = 100$. As mentioned above, the theory of Krylov methods for non-symmetric matrices is still not well developed and few rigorous results on errors have been derived. The leading eigenvalue is reproduced accurately up to just about the short-wave peak before the Krylov results decay faster. The most promising result is at the local minimum between the two peaks. Here there is a very smooth curve of the growth rates of the second and third eigenmodes whose values are close to the values of the leading eigenmode. This result suggests that different eigenmodes might be responsible for the zigzag and short-wave peaks. Returning to the structure, Fig. 4.14 supports this viewpoint as the zigzag and short-wave peak velocity fields are different and the oscillatory region in between suggests a combination of the two which might be the two different modes interchanging dominance.

4.6 Dimensional analysis

Motivated by the scale analysis of those presented in the Chapter 2 review [12, 15, 37, 53], we present a modified scale analysis for small vertical scales as considered in the above

numerical simulations. We consider the Boussinesq equations

$$\frac{\partial \boldsymbol{u}'_h}{\partial t'} + \boldsymbol{u}'_h \cdot \nabla'_h \boldsymbol{u}'_h + u'_z \frac{\partial \boldsymbol{u}'_h}{\partial z'} = -\frac{1}{\rho_0} \nabla'_h p' + \nu \nabla'^2 \boldsymbol{u}_h, \tag{4.14}$$

$$\frac{\partial u'_z}{\partial t'} + \boldsymbol{u}'_h \cdot \nabla'_h u'_z + u'_z \frac{\partial u'_z}{\partial z'} = -\frac{1}{\rho_0} \frac{\partial p'}{\partial z'} - \frac{\rho' g}{\rho_0} + \nu \nabla'^2 u_z, \tag{4.15}$$

$$\nabla'_h \cdot \boldsymbol{u}'_h + \frac{\partial u'_z}{\partial z'} = 0, \tag{4.16}$$

$$\frac{\partial \rho'}{\partial t'} + \boldsymbol{u}'_h \cdot \nabla'_h \rho' + u'_z \frac{\partial \rho'}{\partial z'} + \frac{\partial \rho}{\partial z'} u'_z = D \nabla^2 \rho', \tag{4.17}$$

where the primed notation denotes the dimensional variables in this section only.

Following [12] let U, W be the characteristic velocities in the horizontal and vertical directions, L_h, L_v be the corresponding characteristic length scales, P be the pressure, and R be density perturbation scales, not to be confused with the dipole radius R from above. We assume, differing from the analysis of [12, 37], that in addition to U, L_h being imposed on the system, we also impose a separate vertical scale L_v. This scaling is motivated by the above numerical simulations where we impose a vertical length scale through the vertical wavenumber k_z. The aspect ratio $\delta = L_v/L_h$ is assumed to be small, i.e. $\delta < 1$. We define the horizontal Froude number to be $F_h = U/NL_h$, which is also assumed to be small. Following the above numerical simulations, let $\delta < F_h$, which we can also write as $L_v < U/N$, i.e. vertical scales are assumed to be smaller than the buoyancy scale. We now define the advective time scale $T = L_h/U$. To determine the characteristic scale of W, we are left with two choices: imposing the scaling from the continuity equation or from the density equation. Previous work [12] chose the latter and obtained a characteristic velocity

$$W \lesssim \frac{R F_h g}{\rho_0 N}. \tag{4.18}$$

By contrast, we use the continuity equation (4.16), which implies

$$W \lesssim \delta U. \tag{4.19}$$

This scaling for w is consistent with the assumption that $\delta < F_h$. Using (4.19), the vertical momentum equation (4.15) gives a density scaling of $R \sim \rho_0 U^2/(gL_v)$. Substituting this result into (4.18), we obtain $W \sim UF_h^2/\delta$. Because $\delta < F_h$ we have $U\delta < UF_h^2/\delta$ so our assumptions are consistent. Setting $W \sim U\delta$ the horizontal momentum equation (4.14)

gives $P \sim \rho_0 U^2$. Combining this all, we obtain the following scaling for the Boussinesq equations with $L_v < U/N$:

$$\boldsymbol{u}'_h = U\boldsymbol{u}_h, \qquad u'_z = U\delta u_z, \qquad \rho' = \frac{U^2 \rho_0}{gL_v}\rho, \qquad p' = \rho_0 U^2 p,$$

$$\mathbf{x} = L_h x, \qquad z' = L_v z, \qquad t' = \frac{L_h}{U}t, \qquad Re = \frac{UL_h}{\nu}, \qquad Sc = \frac{\nu}{D}, \tag{4.20}$$

which leads to

$$\frac{\partial \boldsymbol{u}_h}{\partial t} + \boldsymbol{u}_h \cdot \nabla_h \boldsymbol{u}_h + u_z \frac{\partial \boldsymbol{u}_h}{\partial z} = -\nabla_h p + \frac{1}{Re}\nabla_h^2 \boldsymbol{u}_h + \frac{1}{\delta^2 Re}\frac{\partial^2 \boldsymbol{u}_h}{\partial z^2}, \tag{4.21}$$

$$\delta^2\left(\frac{\partial u_z}{\partial t} + \boldsymbol{u}_h \cdot \nabla_h u_z + u_z \frac{\partial u_z}{\partial z}\right) = -\frac{\partial p}{\partial z} - \rho' + \frac{\delta^2}{Re}\nabla_h^2 u_z + \frac{1}{Re}\frac{\partial^2 u_z}{\partial z^2}, \tag{4.22}$$

$$\nabla_h \cdot \boldsymbol{u}_h + \frac{\partial u_z}{\partial z} = 0, \tag{4.23}$$

$$\frac{\partial \rho'}{\partial t} + \boldsymbol{u}_h \cdot \nabla_h \rho' + u_z \frac{\partial \rho'}{\partial z} - \frac{\delta^2}{F_h^2}u_z = \frac{1}{ReSc}\nabla_h^2 \rho + \frac{1}{\delta^2 ReSc}\frac{\partial^2 \rho}{\partial z^2}, \tag{4.24}$$

which holds when $\delta < F_h \ll 1$. This suggests that for very small vertical scales with $\delta \ll F_h$ the effects of stratification should be negligible. At such small vertical scales, density variation due to stratification would be negligible and thus we would not expect stratification to play an important role in the overall evolution. Additionally, the presence of the factors of δ in the denominator of the vertical viscous terms suggests that the effects of viscosity become more dominant at very small vertical scales.

As a result of this scaling analysis we expect that the nature of the instability at short vertical scales to become independent of F_h for large k_z. To test this hypothesis Fig. 4.17 shows growth rate as a function of k_z for four sets of simulation with $Re = 10{,}000$: $F_h = 0.2, 0.1, 0.05$ and a new unstratified case with $F_h = \infty$ (note that, unlike in Fig. 4.4, we are not scaling k_z by F_h). The growth rate curves appear to be converging for large k_z where $\delta \ll F_h$, which agrees with the conclusion of the above scaling analysis. These large k_z are well into the viscous damping range and as discussed above, the effects of viscosity become stronger and we observe a sharper decrease in the growth rate. The curves stop at different k_z due to the range of k_z initially explored. Since these scales are well into the damping range, we did not probe too far as viscosity was smoothing out any potential instabilities.

For the short-wave instability examined above, $\delta/F_h = 1/(k_z F_h)$ ranges from ≈ 0.5 down to 0.1, which is < 1 but not $\ll 1$. As a result, we do not necessarily expect the
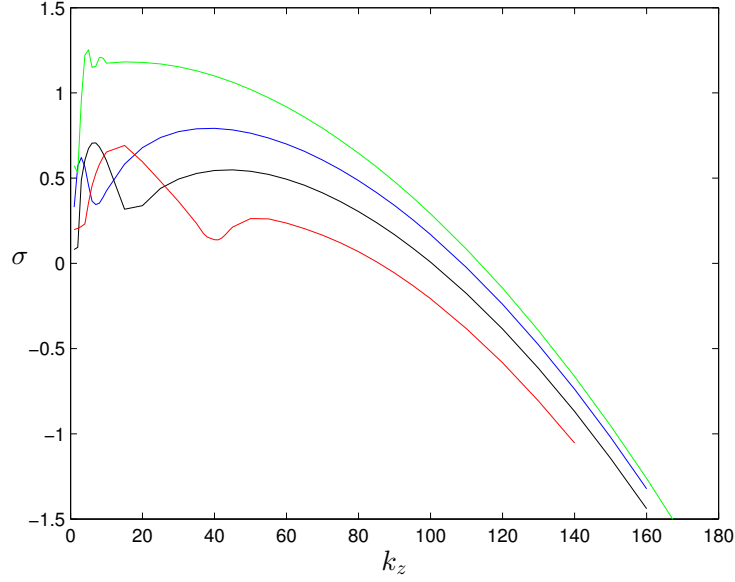
Figure 4.17: Growth rate σ as a function k_z at $Re = 10{,}000$ with $F_h = \infty$ (green), $F_h = 0.2$ (blue), $F_h = 0.1$ (black), $F_h = 0.05$ (red).

characteristics of this instability to be independent of F_h for the parameters considered here. Indeed, our stability analysis shows that the (unscaled) wavenumber k_z of the short-wave peak is weakly dependent on F_h, through the $F_h^{1/5}$ factor in (4.3). However, by examining even larger $k_z F_h$ (i.e. even smaller δ/F_h), this scale analysis suggests that the nature of the short-wave instability will eventually become independent of F_h.

Chapter 5

Nonlinear equation simulations

5.1 Introduction

In the previous chapter, we investigated the linear stability of the Lamb-Chaplygin dipole and we showed that the short-wave instability can have growth rates that are comparable to those of the zigzag instability. An important question is if both of these instabilities exist, which will dominate in the transition to turbulence? In the atmosphere and ocean, a wide range of length scales are excited, so it is expected that both the zigzag instability and the short-wave instability will be excited in nature. Understanding the evolution of these two instabilities and what role they play in the transition to turbulence is important to correctly understand the mechanisms at play in the transition to stratified turbulence. Unfortunately, as alluded to in Chapter 2, linear stability analysis can only take us so far.

In this chapter we evolve the full nonlinear Boussinesq equations to determine how the short-wave instability evolves and what role it plays in the transition to turbulence. The importance of the zigzag instability in the breakdown and transition to turbulence has been well studied [2, 3, 20, 66] but apart from a brief mention in [66], the role of the short-wave instability has not been considered. In this chapter we investigate the role of the short-wave instability in the transition to turbulence. Through nonlinear simulations, we will demonstrate that the saturation level of the short-wave instability is relatively small and depends upon the aspect ratio $\delta = L_v/L_h$. Thus, for many geophysical flows, where $\delta \ll 1$, the short-wave instability may not affect the overall breakdown and transition to turbulence.

5.2 Set-up

To investigate the nonlinear evolution, we use a code developed by Waite [64], which is a parallel version of the code originally developed by Bartello [5]. The code implements the spectral method technique discussed in Chapter 3 to solve the nonlinear Boussinesq equations. Unlike in linear stability analysis, nonlinear analysis of the Boussinesq equations is much more complicated as particular attention must be taken to ensure proper resolution of the small scales. The breakdown of the zigzag instability exhibits small scale turbulence [3] which suggests that we might observe a similar result for the short-wave instability. Thus we need to choose grid sizes that resolve the smallest scales of such turbulence, known as the Kolmogorov scale.

The Kolmogorov scale is given by [33]

$$\eta = \left(\frac{\nu^3}{\epsilon} \right)^{1/4},\tag{5.1}$$

where ϵ is the kinetic energy dissipation rate, which is commonly approximated as [38]

$$\epsilon \sim \frac{U^3}{R},\tag{5.2}$$

where U, R are the characteristic velocity and length respectively. Rewriting the Kolmogorov scale η in terms of the Reynolds number by multiplying by the characteristic length R we obtain

$$\frac{\eta}{R} = \frac{1}{Re^{3/4}}.\tag{5.3}$$

We want to choose the number of grid points to be such that the horizontal and vertical grid spacings satisfy $\Delta x \approx \Delta z \approx \eta/R$, where the factor of R takes into account the $\Delta x, \Delta z$ are the grid spacings of the dimensionless equations Eqs. (2.39-2.41).

To focus specifically on the short-wave instability, we choose the vertical scale to be that of the short-wave instability. To illustrate, consider $Re = 2000, F_h = 0.2$ where the short-wave instability peaks at $k_z = 20$. Here we set the vertical domain size to be one vertical wavelength of the short-wave instability, i.e.

$$L_v = \frac{2\pi}{k_z} = \frac{2\pi}{20}.\tag{5.4}$$

Re	F_h	Δt	k_z
2000	0.2	10^{-4}	10-50
5000	0.2	10^{-4}	20-45 20-45

Table 5.1: Overview of the numerical parameters.

From our linear results, we again take $L = 9$. Due to the set-up of the code, the number of grid points in every direction has to be a power of small primes; we choose powers of 2. Thus let us a priori consider the number of horizontal grid points to be $n_x = 1024$. We have that the horizontal resolution is

$$\Delta x = \frac{L}{n_x} = \frac{9}{1024} \approx 0.00878, \qquad \frac{\eta}{R} \sim \frac{1}{Re^{3/4}} = 0.003343, \tag{5.5}$$

and we approximately have that $\Delta x \sim \eta/R$. In nonlinear simulations of the zigzag instability, Augier et al. [2] used $n_x = 512$ with $Re = 2500$ and $L = 10$; our resolution is slightly higher. If we choose $n_z = 32$ grid points in the vertical, we find that $\Delta z \approx 0.00982$ which is very similar to Δx. For our timestep we choose $\Delta t = 5.0 \times 10^{-4}$. Each run was initialised with a random density perturbation that was random in x and y and sinusoidal in z, with amplitude 0.01. The parameters are summarised in Table 5.1.

5.3   Saturation level of short-wave instability

As mentioned in the introduction, previous investigations into the transition to turbulence have focused only on the zigzag instability. In all these simulations, it is clear that the dominant instability is the zigzag instability. For example, in Waite and Smolarkiewicz [66], the growth rates of the zigzag instability agree with the linear theory. It is possible that these simulations were not resolving the small scales, although this does not seem likely based on the parameters given. This is because the length scale of the short-wave instability is about an order of magnitude or so smaller than that of the zigzag instability. Since these simulations were intended to study the transition to turbulence, they would be resolving, or close to resolving, the Kolmogorov scale, which is much smaller than the short-wave instability. Hence it is unlikely a resolution issue. Instead, it could be the case that the short-wave instability is present but saturates out and does not contribute significantly to the transition to turbulence. We explore this option here.

Consider the following scaling argument and results due to Ngan et al. [46]. They were interested in three-dimensionalisation of a two-dimensional flow in small aspect ratio

domains, which they referred to as quasi-two-dimensional turbulence. They considered this as they were interested in geophysical flows which exhibit small aspect ratios, $\delta = 0.01 - 0.1$ [46]. As we have seen, stratified turbulence tends to have a small aspect ratio and, as discussed in Chapter 2, exhibits characteristics of geophysical flow. However, it is important to note that Ngan et al. [46] did not consider stratification and they were only focusing on the unstratified case of turbulence with small aspect ratios.

To investigate this three-dimensionalisation, in their numerical experiments they took fully developed 2D turbulence and subjected it to a 3D perturbation. They then measured the saturation level of this 3D perturbation. The saturation level is defined to be

$$\text{saturation} = \left. \frac{u}{U} \right|_{t_{sat}}, \tag{5.6}$$

where the ratio between the 3D rms velocity u and the 2D rms velocity U are evaluated at the saturation time. The saturation time is the time at which the time series of the 3D rms velocity levels off or saturates. They found, numerically, that this saturation level depended linearly on the aspect ratio δ, up to a certain aspect ratio, $\delta = 0.5$. Beyond $\delta = 0.5$ the numerical simulations could no longer be considered quasi-two dimensional.

To explain this result, Ngan et al. considered a simple scaling argument [45, 46]. Initially the time scales of the 2D base flow is long compared to that of the 3D perturbation flow. However once the 3D perturbation settles down and saturates, its timescale becomes similar to that of the 2D flow. Consider the following timescales for these flows [46] as

$$T_{2D} = \frac{U}{L}, \qquad T_{3D} = \frac{u}{H}, \tag{5.7}$$

where U is the characteristic velocity of the 2D flow at saturation and u is the characteristic velocity of the 3D flow at saturation. At saturation $T_{2D} \sim T_{3D}$ and thus we have that

$$\frac{U}{L} \sim \frac{u}{H} \Rightarrow \frac{u}{U} \sim \frac{H}{L} = \delta, \tag{5.8}$$

which is the result they confirmed numerically.

Motivated by this result, we consider the saturation levels of the short-wave instability for $Re = 2000, 5000$ and $F_h = 0.2$. These two cases were chosen as they both had short-wave instability growth rates similar to that of the zigzag peak. Higher Re could not be explored due to resolution issues, as alluded to in the previous section.

There are different strategies available for determining the perturbation energy in these simulations. One approach is to compute the 2D and 3D rms velocities using the vertical

wavenumber k_z[1] kinetic energy spectrum. The two-dimensional kinetic energy is in $k_z = 0$; the three-dimensional kinetic energy is the contribution from all non-zero k_z.

However, a simpler approach is to use the potential and kinetic energy, since the potential energy is entirely due to the perturbation, while (at early times at least) the kinetic energy is mainly due to the dipole.

Both methods were used to compute the saturation level and it was found that the results using the kinetic and potential energy collapsed better than those of the 2D and 3D kinetic energy. Fig. 5.1 demonstrates the evolution of these quantities for $Re = 5000, F_h = 0.2, k_z = 40$. As can be observed, the total kinetic and 2D kinetic energies are nearly indistinguishable. The 3D kinetic and potential energies have similar amplitude and trend, but the saturation level seems clearer and better defined in the potential energy. For this reason, we choose to use the potential energy to identify the saturation level. Despite the differences, both curves have the same saturation time, roughly $t = 20$. For the parameters investigated, the saturation time was approximately $t = 20$. Nevertheless, it is still interesting to consider the evolution of the contributions to the kinetic energy from different vertical wavenumbers. Fig. 5.2 demonstrates this for the parameters given above. Here we can explicitly see which wavenumbers are contributing to the total 3D kinetic energy. For almost the entire simulation, the primary vertical mode ($k_z = 20$) domainted. However at around the saturation time $t = 20$, $k_z = 2 \times 20$ appears to make a small, but noticeable contribution to the total 3D kinetic energy. This lasts for about 5 time units before diffusion begins to rapidly diffuse out the smaller scales, which is especially evident in the highest wavenumbers.

To determine the saturation level as a function of δ, we performed a number of simulations of the short-wave instability perturbed at a range of k_z values around the short-wave peak for $Re = 2000, 5000, F_h = 0.2$. Fig. 5.3 is the case of $Re = 2000$. As found by Ngan et al. [46], the saturation level increases for increasing delta. Using a least-squares fit we find that the best fit curve is $\delta^{3.02}$ and have plotted a reference curve of slope 3. Fig. 5.4 is the case of $Re = 5000$. Again, the trend of saturation level with increasing aspect ratio is observed here. Using a least-squares fit we find that the best fit curve is $\delta^{3.16}$ and a reference curve of slope 3 is plotted. At this higher Reynolds number, it was observed that although the saturation was clear, the actual time to choose to evaluate the saturation ratio was not well defined. In Fig. 5.1 although the saturation level here is fairly flat, there is still a bit of variation in the saturation level. In some cases this variation was more pronounced so defining where to evaluate the saturation ratio was not well defined. For consistency, the first maximum after $t = 20$ times unit was chosen.

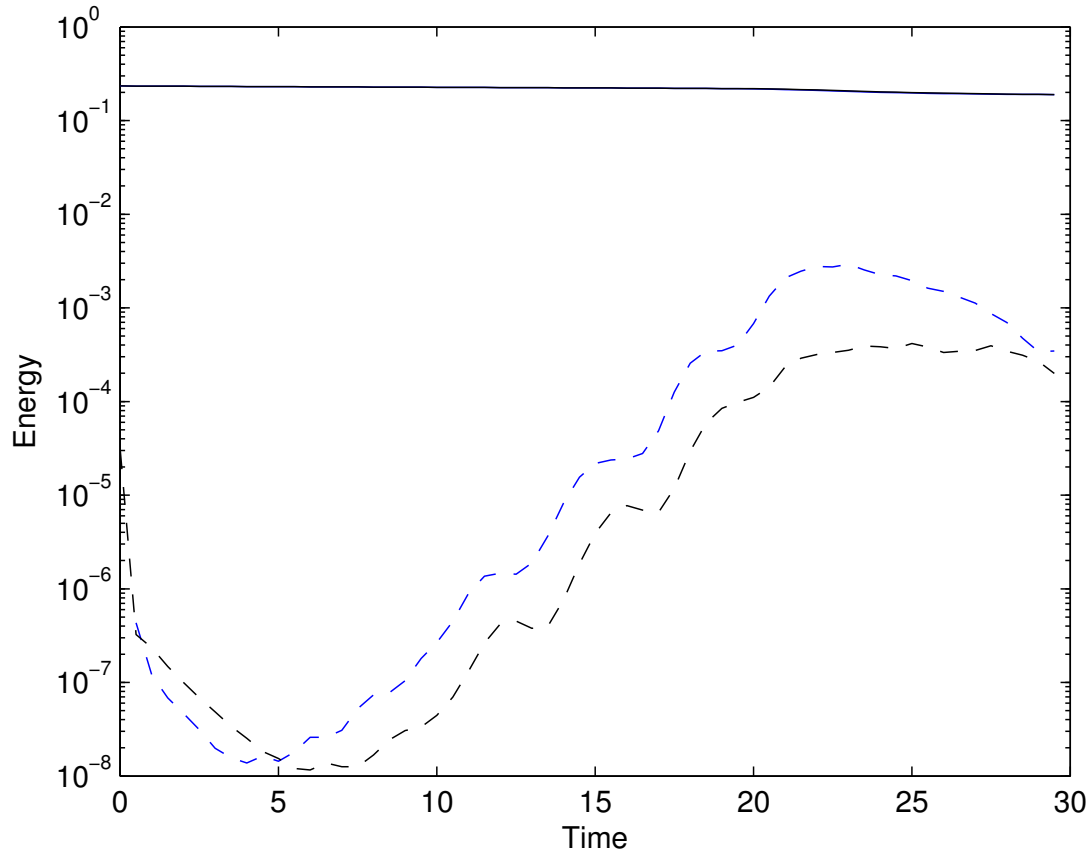[1]This is the vertical wavenumber of the nonlinear simulation, not that of the short-wave instability.

Figure 5.1: Time series demonstrating the two ways of computing the energy for $Re = 5000$, $F_h = 0.2$, and $k_z = 40$. The blue curves correspond to the kinetic energy separated into 2D (solid) and 3D (dashed); the black curves are the total kinetic energy (solid) and potential energy (dashed). All energies are domain averages.

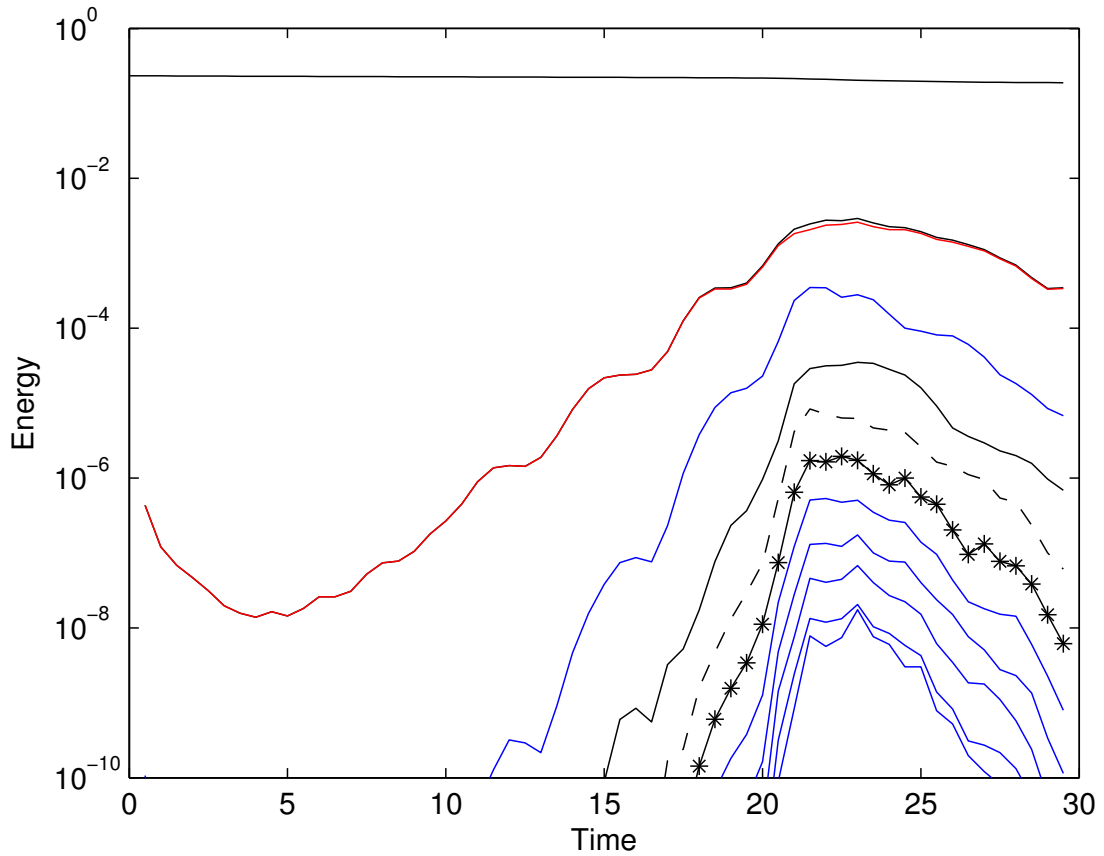Figure 5.2: Time series for the contribution to the kinetic energy from different vertical wavenumbers for $Re = 5000$, $F_h = 0.2$, and $k_z = 40$. The top black curve corresponds to $k_z = 0$, i.e. the 2D kinetic energy. The remaining curves correspond to $k_z = 40n$ where $n = 1$ (red), 2 (blue), 3 (black), etc. The black curve that is obscured by the red line is the total 3D kinetic energy.
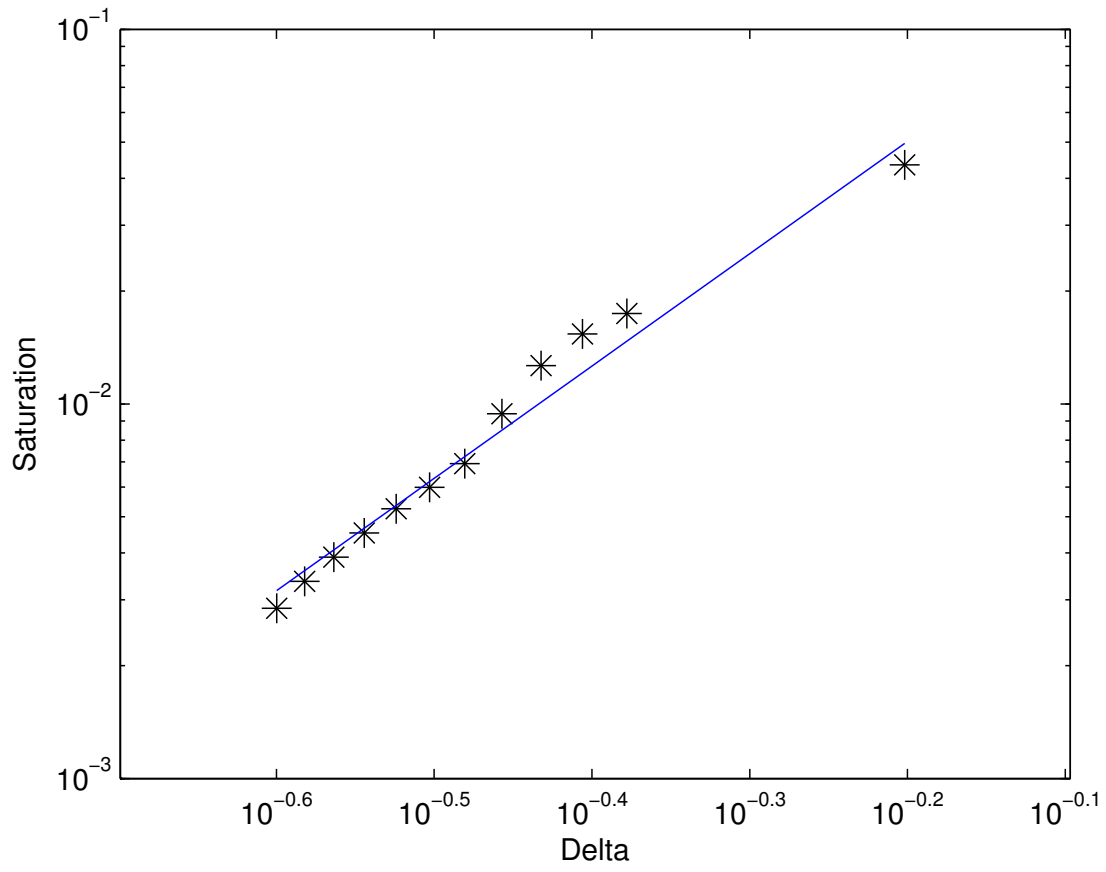
Figure 5.3: Saturation levels for a range of aspect ratios δ for $Re = 2000$ and $F_h = 0.2$. The curve is the linear best with slope of 3.
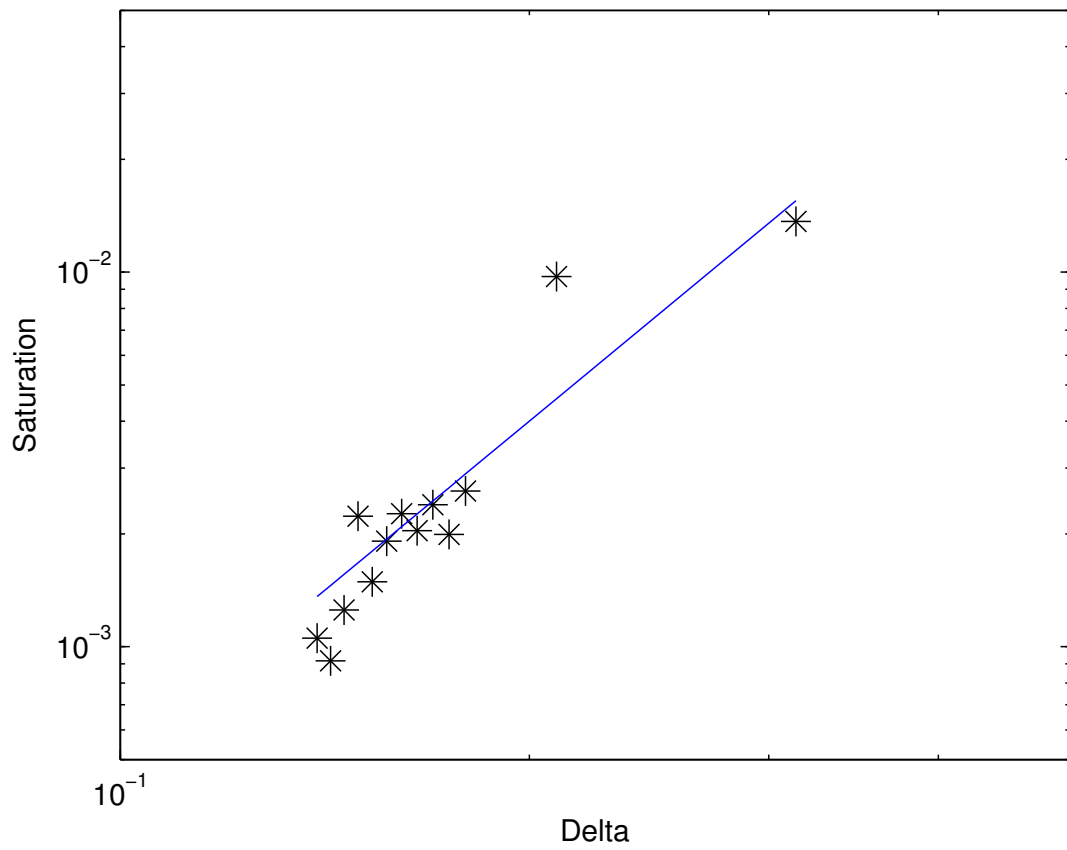
Figure 5.4: Saturation levels for a range of aspect ratios δ for $Re = 5000$ and $F_h = 0.2$. The curve is the linear best with slope of 3.

From these two curves it suggests that the saturation level of the short-wave instability is given by

$$\left.\frac{E_{2D}}{E_{3D}}\right|_{t_{sat}} \sim \delta^3, \tag{5.9}$$

which suggests that as the aspect ratio decreases, the saturation level decreases. From the linear theory, the wavenumber of maximum short-wave instability was found to scale as $k_z \sim F_h^{-1/5} Re^{2/5}$ or $k_z' \sim F_h^{-1/5} Re^{2/5}/R$ in dimensional units. Then the aspect ratio scales as $\delta = 2\pi(k_z R) \sim F_h^{1/5} Re^{-2/5}$ and hence the saturation level is

$$\left.\frac{E_{2D}}{E_{3D}}\right|_{t_{sat}} \sim (2\pi)^3 F_h^{3/5} Re^{-6/5}. \tag{5.10}$$

Substituting in $Re = 5000$ and $F_h = 0.2$ yields a ratio on the order of 10^{-3} which agrees with Fig. 5.1. For $F_h \ll 1$ and $Re \gg 1$ this ratio is $\ll 1$. Thus given that the short-wave instability seems to saturate at a relatively low level, we should not expect the short-wave instability to play a significant role in the evolution of the Lamb-Chaplygin dipole's transition to turbulence.

This scaling for the saturation level differs from that of Ngan et al. [46]. If we square Eq. (5.6) we obtain

$$\frac{u^2}{U^2} = \frac{KE_{3D}}{KE_{2D}} \sim \delta^2, \tag{5.11}$$

which suggests that the saturation level will scale quadratically instead of cubically.

Fig. 5.5 is the vertical vorticity at three times, $t = 15, 20$, and 25. Just before saturation ($t = 20$) the structure of the dipole does not exhibit any small-scale features. However at $t = 20$, the saturation time, the dipole exhibits many small-scale features. By $t = 25$ they appear to have been diffused out and the structure of the dipole has returned to one similar to before saturation, albeit with the two cores of the dipole more homogeneous in vorticity. The structure suggests that the saturation time is important as the dipole is undergoing some sort of transition, but as we saw, this transition is short lived as 5 time units later, small-scale behaviour has diffused out and there is no suggestion that the system will transition to turbulence. Indeed, this result reaffirms that the gridspacing is sufficient enough to resolve the nonlinear evolution. Note that there are small vortices outside the main dipole because the initial condition is not perfectly periodic. If the domain size was larger, these vortices would disappear. They do not contribute to the
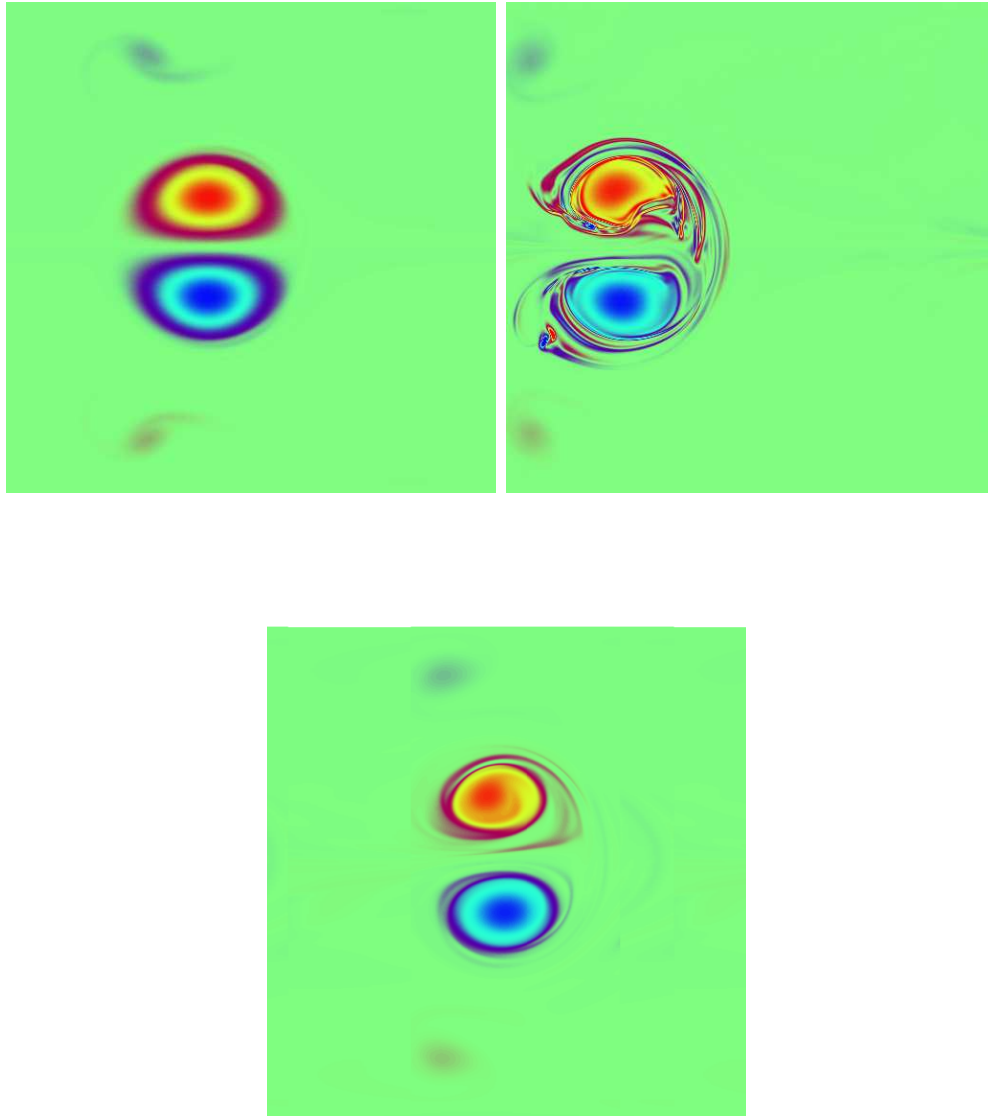
Figure 5.5: Evolution of the vertical vorticity for $Re = 5000, F_h = 0.2, k_z = 40$ for $t = 15$ (top right), $t = 20$ (top left), $t = 25$ (bottom). Red corresponds to maximum vorticity and blue corresponds to minimum vorticity. The domain size is 9×9.

overall simulation. Since this system does not suggest it will transition to turbulence, resolving the Kolmolgorov scales is likely unnecessary.

We now examine the growth rate of the linear theory compared to that seen in the nonlinear simulations. In comparing the linear theory with the nonlinear theory, there is a problem with what defines the linear regime of the nonlinear simulation. If we examine the growth of the potential energy between $t = 5$ and $t = 20$ in Fig. 5.1, it is very difficult to justify approximating this growth rate as linear. For most of the cases of $Re = 5000$ and $F_h = 0.2$, we were unable to determine a consistent way to determine the growth rate of the perturbation and thus we have not included the results for this simulation. For $Re = 2000$ and $F_h = 0.2$, the growth rate of the potential energy was more linear and a linear fit was done to determine the growth rate. Fig. 5.6 illustrates the results for the linear and nonlinear theories for $Re = 2000$ and $F_h = 0.2$. Here the nonlinear growth rates are greater than those of the linear theory; however the shape of the curve follows the linear theory curve reasonably well. Again, the issue of the growth in the potential energy not being perfectly linear could contribute to this discrepancy of $8\% - 40\%$. It is unclear why the nonlinear simulations do not exhibit exponential growth, even at early times when the initial perturbation is small. It could be that sub-dominant modes with similar growth rates are contributing to the time series in Fig. 5.1 and the discrepancy with the linear theory, but more work is required to resolve this question.

We conclude with a brief discussion of the robustness of the results. To ensure our results were not under-resolved, we ran another simulation with double the horizontal and vertical resolution. In order to keep the computational cost manageable, we shrank the horizontal domain to $L = 5$, but kept $n_x = 1024$, however n_z doubled to 64. The results are plotted in Fig. 5.7. As can be observed, the domain-averaged kinetic and potential energy in the system is higher with $L = 5$ because the domain is smaller and hence the dipole takes up a greater percentage of available grid points. Calculating the saturation level, here taken to be the maximum of the potential energy, yields a difference of 2% between $L = 5$ and $L = 9$. In calculating the growth rate there is a difference of 8%. Thus if we increase the resolution, we will obtain similar results.
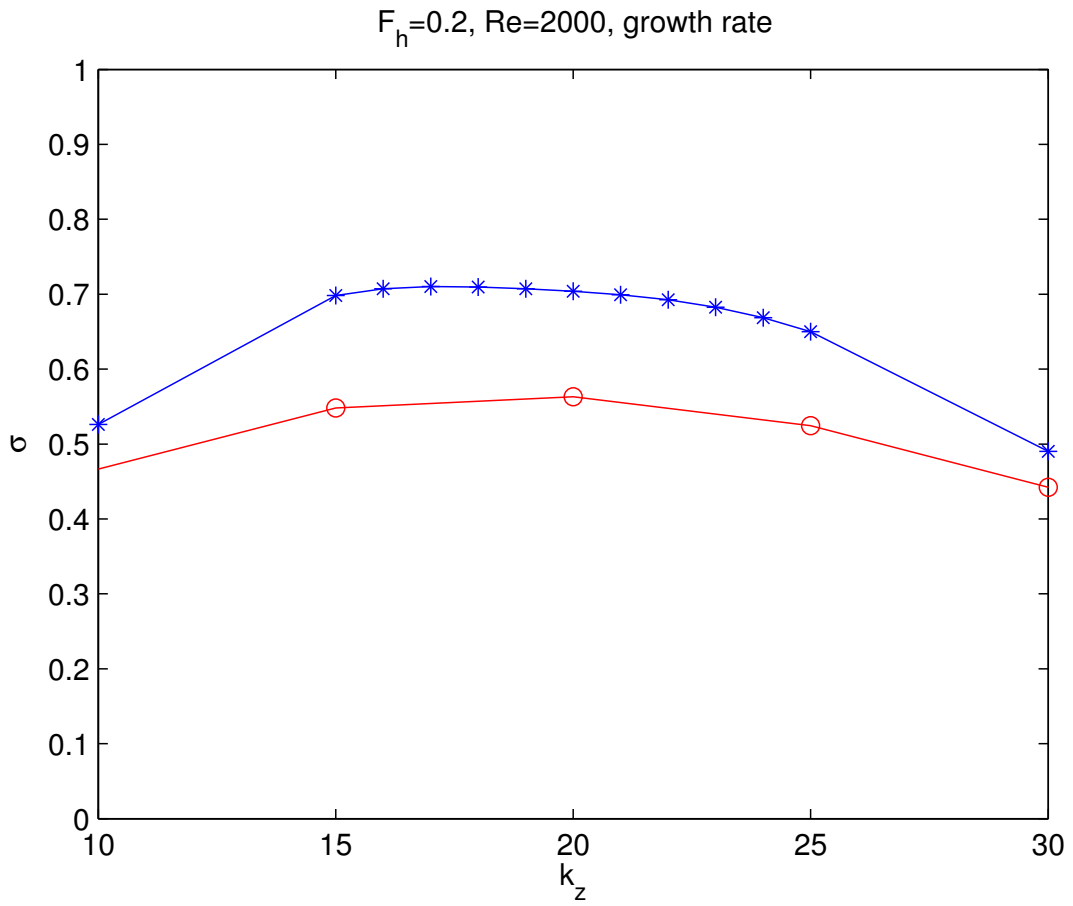
Figure 5.6: Growth rate for $Re = 5000$ and $F_h = 0.2$ with the linear results (red) and the nonlinear results (blue). Note we have not scaled by F_h unlike the results in Chapter 3.
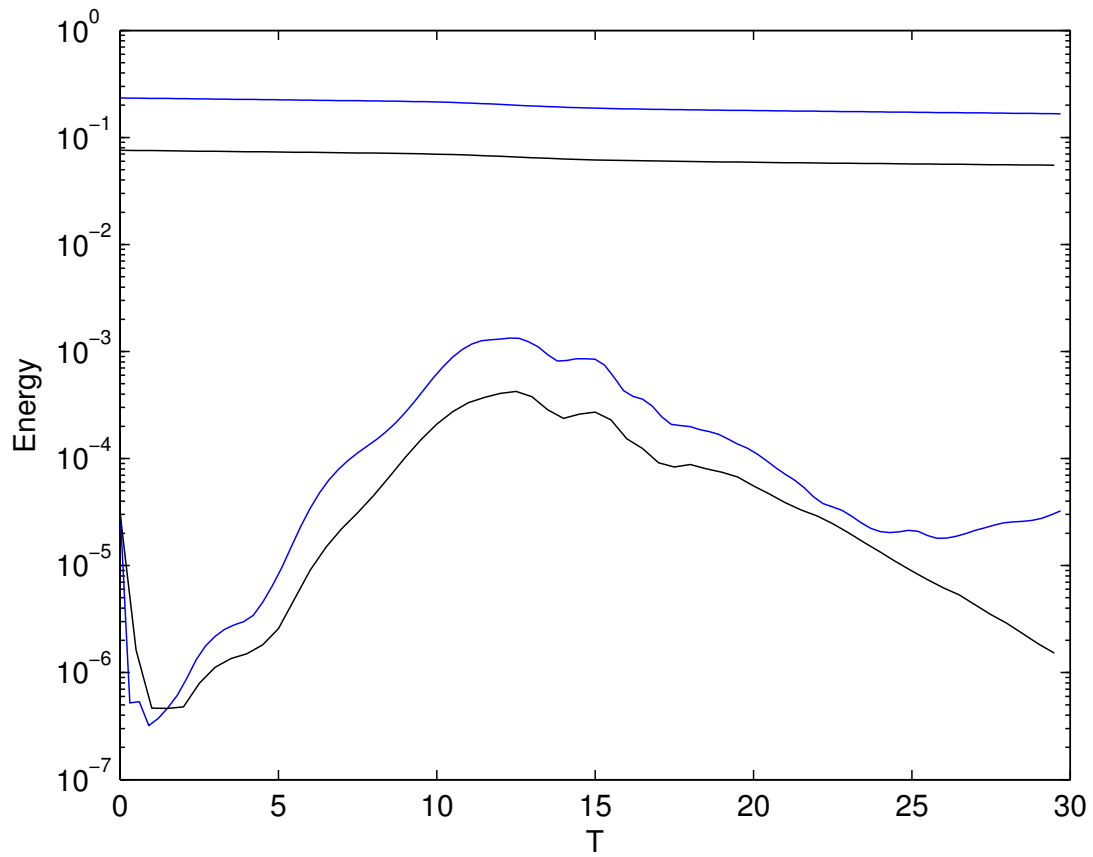
Figure 5.7: Time series of the potential energy (bottom curves) and kinetic energy (top curves) for $L = 5$ (blue) and $L = 9$ (black). Here $Re = 2000, F_h = 0.2, k_z = 20$.

Chapter 6

Conclusions

In this thesis, we have investigated the linear stability of the Lamb-Chaplygin dipole for perturbations with small vertical scales. In particular, we have considered vertical scales from around the buoyancy scale U/N, where the zigzag instability occurs [11, 12, 64, 65], down to the dissipation scale. We have discovered a short-wave instability that emerges at scales much smaller than the buoyancy scale. This instability can exhibit a growth rate that is comparable to, and possibly even greater than, that of the zigzag instability. Despite having a similar growth rate in some cases, the structure of the instability is qualitatively different than the structure of the zigzag instability suggesting a different mechanism is governing the evolution. We have discovered that the location of the peak depends upon a combination of the Reynolds and Froude numbers, specifically the buoyancy Reynolds number Re_b which plays an important role in stratified fluids. The wavenumber of maximum growth rate for the short-wave instability is found to scale like $F_h k_z \sim Re_b^{2/5}$ for the range of Re_b considered here. We expect this may change at even larger Re_b. By contrast, the maximum growth rate of the zigzag instability occurs for $F_h k_z \sim 1$ [10]. As a result, these instabilities will be widely separated when $Re_b \gg 1$, as in the case of strongly stratified turbulence [15].

Despite the similar growth rates, we have discovered that these short-wave instabilities saturates at a level proportional to the cubed of the aspect ratio. For geophysical applications, δ is frequently $\ll 1$, which suggests that the short-wave instabilities do not contribute significantly to the breakdown of the Lamb-Chaplygin dipole to turbulence.

Some unanswered questions still remain and provide inspiration for future work. Structure-wise the short-wave instability is very different from that of the zigzag instability. As suggested by the sub-dominant mode analysis, there is likely a transition of leading eigen-

modes between the zigzag and short-wave peaks. Furthermore, the nature of this transition is also interesting as it exhibits oscillations not observed in either the short-wave or zigzag instabilities. Briefly discussed were the waves behind the dipole, which resmeble a ship wave pattern with an angle that follows a simple scaling law. Investigations into waves behind vortices, especially those behind stratified vortices, has remained unexplored. Such flow might resemble flow over terrain which predicts a similar scaling law for the angle of those waves [55]. It would be interesting to investigate the short-wave instability in other systems, specifically adding in the effects of rotation. Such investigations of buoyancy length effects have illustrated the zigzag instability, which demonstrates the universality of the result in other flow configurations. It is likely that such short-wave instabilities may be universal as well.

Throughout, we have assumed that the stratification is constant. While this is possible in a lab setting, it is not a very physical assumption for real geophysical systems where the stratification is non-constant. While there are vertical leves in the atmosphere and ocean over which N is approximately constant, both fluids are characterised by distinctive stratification profiles – e.g. the pycnocline in the ocean, and boundary layer inversions and the tropopause in the atmosphere (e.g. Gill [27]) – which may sigificantly alter the structure of the instabilities discussed. Furthermore, it seems unlikely that the short-wave instability generates turbulence which will make future computations significantly easier as there is no need to resolve the Kolmogorov scales. This will allow for a greater potential computational parameter search, specifically in a larger Reynolds number limit. Furthermore, since we have determined a scaling law for the short-wave instability through the buoyancy Reynolds number, it would be interesting to investigate how robust this observation is in more physical systems.

In this thesis we focused specifically on the numerical aspects of vortex instabilities. The impetus for this work was an experiment [9] and it would be interesting to investigate the possibility of observing the short-wave in an experimental setting. However there are technical details that would need to be addressed. To isolate the short-wave instability, a tank that has a height that is roughly an order of magnitude smaller than that of [9] would be required. However, given lab constraints, such experiments would encounter boundary effects due to the smaller size of the tank whereas such effects were avoided in [9]. Such technical details are left to future experimentalists.

APPENDICES

Appendix A

Matlab Code for Solving Advection Equation

The following code is the MATLAB code for evaluating the advection-diffusion equation
with 2/3-rule deliasing

```
%construct the grid and basic parameters
N=128; dx=2*pi/N; x=dx*(1:N);t=0;dt=dx/10;tf=5;nsteps=ceil(tf/dt);
c=0.2+sin(x-1).^2;
%store the wavenumbers
kx=[0:N/2-1 0 -N/2+1:-1];
%define cut to cut out the highest Fourier modes
cut=ones(1,N); ksq=kx.*kx;
%cut out the Fourier co-efficients according to dealiasing
%because of wavenumber ordering cut out (most negative wave numbers start
%at N/2) e.g. (2/3)*(N/2) : (N/2+(1/3)(N/2) for 2/3s
cut(ceil(dealias_coeff*N/2):(N/2+ceil((1-dealias_coeff)*N/2))+1)=0;
%initial condition
u=exp(-100*(x-1).^2);uhat=fft(u);
%do initial timestep using Euler
Fold=-fft(c.*real(ifft(1i*cut.*kx.*uhat)));
uhat=(uhat+dt*Fold);

%do Adams Bashforth
for i=1:nsteps
```

```
        F=-fft(c.*real(ifft(1i*cut.*kx.*uhat)));
        uhat=uhat+1.5*dt*F-0.5*dt*Fold;
        Fold=F;
end
```

In the above code the line `ifft(1i*cut.*kx*uhat)` evalutes the spectral derivative of
the velocity field and adds in the dealiasing by cutting out the top $1/3$ of the Fourier
coefficients. Note that MATLAB stores the wavenumbers `kx=[0:N/2-1 0 -N/2+1:-1]`
and thus to zero out the correct coefficients requires some clever index manipulation.

References

[1] D.J. Acheson. *Elementary fluid dynamics*. Oxford University Press, 1990.

[2] P. Augier and P. Billant. Onset of seconardy instabilities on the zigzag instability in stratified fluids. *J. Fluid Mech*, 682:120–131, 2011.

[3] P. Augier, J.-M. Chomaz, and P. Billant. Spectral analysis of the transition to turbulence from a dipole in stratified fluid. *J. Fluid. Mech*, 713:86–108, 2012.

[4] B.J. Bailey. Three-dimensional instability of elliptical flow. *Phys. Rev. Lett.*, 57:2160, 1986.

[5] P. Bartello. Geostrophic adjustment and inverse cascades in rotating stratified turbulence. *J. Atmos. Sci.*, 52:4410–4428, 1995.

[6] G.K. Batchelor. *An Introduction to Fluid Dynamics*. Cambridge University Press, 1967.

[7] C.M. Bender and S.A. Orszag. *Advanced Mathematical Methods for Scientists and Engineers*. Springer, 1999.

[8] P. Billant, P. Brancher, and J.-M. Chomaz. Three-dimensional stability of a vortex pair. *Phys. Fluids*, 11:2069–2077, 1999.

[9] P. Billant and J.-M. Chomaz. Experimental evidence for a new instability of a vertical columnar vortex pair in a strongly stratified fluid. *J. Fluid Mech*, 418:167–188, 2000.

[10] P. Billant and J.-M. Chomaz. Theoretical analysis of the zigzag instability of a vertical columnar vortex pair in a strongly stratified fluid. *J. Fluid Mech*, 419:29–63, 2000.

[11] P. Billant and J.-M. Chomaz. Three-dimensional stability of a vertical columnar vortex pair in a stratified fluid. *J. Fluid Mech*, 419:65–91, 2000.

[12] P. Billant and J.-M. Chomaz. Self-similarity of strongly stratified inviscid flows. *Phys. Fluids*, 13:1645–1651, 2001.

[13] L. Bovard and M.L. Waite. Short wave vortex instability in stratified fluids. *Phys. Fluids*, Submitted.

[14] J.P. Boyd. *Chebyshev and Fourier Spectral Methods*. Dover Publications, 2001.

[15] G. Brethouwer, P. Billant, E. Lindborg, and J.-M. Chomaz. Scaling analysis and simulations of strongly stratified turbulent flows. *J. Fluid Mech*, 585:343–368, 2007.

[16] C. Canuto. *Spectral Methods: Evolution to Complex Geometries and Applications to Fluid Dynamics*. Springer, 2007.

[17] J.W. Cooley and J.W. Tukey. An algorithm for the machine calculation of complex fourier series. *Mathematics of computation*, 19:297–301, 1965.

[18] T.H. Cormen, C.E. Leiserson, R.L. Rivest, and C. Stein. *Introduction To Algorithms*. MIT Press, 2001.

[19] S.C. Crow. Stability theory for a pair of trailing vortices. *AIAA journal*, 8:2172–2179, 1970.

[20] A. Deloncle, P. Billant, and J.-M. Chomaz. Nonlinear evolution of the zigzag instability in stratified fluids: a shortcut on the route to dissipation. *J. Fluid Mech*, 660:229–238, 2008.

[21] A. Deloncle, P. Billant, and J.-M. Chomaz. Three-dimensional stability of vortex arrays in a stratified and rotating fluid. *J. Fluid Mech*, 678:482–510, 2011.

[22] P.G. Drazin and W.H. Reid. *Hydrodynamic Instability*. Cambridge University Press, 2004.

[23] D.R. Durran. *Numerical Methods for Fluid Dyanimcs 2nd Edition*. Springer, 2010.

[24] Moore D.W. and P.G. Saffman. The instability of a straight vortex filament in a strain field. *Proc. R. Soc. Lond. A*, 346:413–425, 1975.

[25] W.S. Edwards, L.S. Tuckerman, R.A. Friesner, and D.C Sorensen. Krylov methods for the incompressible navier-stokes equations. *J. Comput. Phys.*, 110:82–102, 1994.

[26] M. Frigo and S.G. Johnson. The design and implementation of fftw3. *Proc. IEEE*, 93:216–231, 2005.

[27] A.E. Gill. *Atmosphere-ocean Dynamics*. Academic Press, 1982.

[28] D.A. Herbert and S.M. de Bruyn Kops. Predicting turbulence in flows with strong stable stratification. *Phys. Fluids*, 18:18–28, 2006.

[29] Clay Mathematics Institute. Navier-Stokes equations. http://www.claymath.org/millennium/Navier-Stokes_Equations/. Accessed November 8th, 2013.

[30] R. Kerswell. Elliptical instability. *Annu. Rev. Fluid Mech.*, 34:83–113, 2002.

[31] D. Kimmler. *A First Course in Fourier Analysis*. Cambridge University Press, 2008.

[32] P.K. Kundu. *Fluid Dynamics*. Academic Press, 5th edition, 2012.

[33] M. Lesieur. *Turbulence in Fluids*. Springer, 2008.

[34] R. LeVeque. *Finite Difference Methods for Ordinary and Partial Differential Equations: Steady-State and Time-dependent Problems*. SIAM, 2007.

[35] T. Leweke and C.H.K. Williamson. Cooperative elliptic instability of a vortex pair. *J. Fluid Mech*, 360:85–119, 1998.

[36] T. Leweke and C.H.K. Williamson. Long-wavelength instability and reconnection of a vortex pair. In E. Krause and K. Gersten, editors, *IUTAM Symposium on Dynamics of Slender Vortices*, volume 44 of *Fluid Mechanics and Its Applications*, pages 225–234. 1998.

[37] D.K. Lilly. Stratified turbulence and the mesoscale variability of the atmosphere. *J. Atmos. Sci*, 40:749, 1983.

[38] E. Lindborg. The energy cascade in a strongly stratified fluid. *J. Fluid Mech*, 550:207–242, 2006.

[39] MathWorks. 2-D Fast Fourier Transform. http://www.mathworks.com/help/matlab/ref/fft2.html. Accessed November 8th, 2013.

[40] V.V. Meleshko and G. J. F. van Heijst. On Chaplygin's investigations of two-dimensional vortex structures in an inviscid fluid. *J. Fluid Mech*, 272:157–182, 1994.

[41] O. Métais and J.R. Herring. Numerical simulations of freely evolving turbulence in stably stratified fluids. *J. Fluid Mech.*, 202:117–148, 1989.

[42] C. Meyer. *Matrix Analysis and Applied Linear Algebra Book and Solutions Manual.* SIAM, 2000.

[43] T. Miyazaki and Y. Fukumoto. Three-dimensional instability of strained vortices in a stably stratified fluid. *Phys. Fluids A*, 4:2515–2522, 1992.

[44] G.D. Nastrom and K.S. Gage. A climatology of atmospheric wavenumber spectra of wind and temperature observed by commercial aircraft. *J. Atmos. Sci.*, 42:950–960, 1985.

[45] K. Ngan, D.N. Straub, and P. Bartello. Three-dimensionalisation of freely-decaying two-dimensional turbulence. *Phys. Fluids*, 16:2918, 2004.

[46] K. Ngan, D.N. Straub, and P. Bartello. Aspect ratio effects in quasi-two-dimesional turbulence. *Phys. Fluids*, 17:1–10, 2005.

[47] S.A. Orszag and G.S. Patterson. Numerical simulations of turbulence. In M. Rosenbatt and C. Van Atta, editors, *Statistical models and and turbulence*. Springer, 1972.

[48] P. Otheguy, P. Billant, and J.-M. Chomaz. Elliptic and zigzag instabilities on co-rotating vertical vortices in a stratified fluid. *J. Fluid Mech*, 553:253–272, 2006.

[49] R.T. Pierrehumbert. Universal short-wave instability of two-dimensional eddies in an inviscid fluid. *Phys. Rev. Lett*, 57:2157–2159, 1986.

[50] P.G. Potylitsin and W.R. Peltier. Stratification effects on the stability of columnar vortices on the f-plane. *Journal of Fluid Mechanics*, 355:45–79, 1998.

[51] O. Reynolds. An experimental investigation of the circumstances which determine whether the motion of water shall be direct or sinuous, and of the law of resistance in parallel channels. *Proc. R. Soc. A*, 35:84–99, 1883.

[52] J.J. Riley and S. M. de Bruyn Kops. Dynamics of turbulence strongly influenced by buoyancy. *Phys. Fluids*, 15:2047–2059, 2003.

[53] J.J. Riley and M.-P. Lelong. Fluid motions in the presence of strong stable stratifica-tions. *Annu. Rev. Fluid Mech.*, 32:613–657, 2000.

[54] J.J. Riley and E. Lindborg. Recent progress in stratified turbulence. In K. Sreenivasan P. Davidson, Y. Kaneda, editor, *Ten Chapters in Turbulence*. Cambridge University Press, 2013.

[55] R.D. Sharman and M.G. Wurtele. Ship waves and lee waves. *J. Atmos. Sci.*, 40:396–427, 1983.

[56] L.N. Trefethen. *Spectral Methods in MATLAB*. SIAM, 2000.

[57] L.N. Trefethen and D. Bau. *Numerical Linear Algebra*. Society for Industrial and Applied Mathematics, 1997.

[58] D.J. Tritton. *Physical Fluid Dynamics*. Clarendon Press, 1988.

[59] C.Y. Tsai and S.E. Widnall. The stability of short waves on a straight vortex filament in a weak externally imposed strain field. *J. Fluid Mech*, 73:721–733, 1976.

[60] G.K. Vallis. *Atmospheric and Oceanic Fluid Dynamics: Fundamentals and Large-scale Circulation*. Cambridge University Press, 2006.

[61] M. Van Dyke. *Perturbation Methods in Fluid Mechanics*. Parabolic Press Stanford, 1975.

[62] M. Van Dyke. *An Album of Fluid Motion*. Parabolic Press Stanford, 1982.

[63] M.L. Waite. Course notes for AMATH 463, 2011.

[64] M.L. Waite. Stratified turbulence at the buoyancy scale. *Phys. Fluids*, 23:23–35, 2012.

[65] M.L. Waite and P. Bartello. Stratified turbulence dominated by vortical motion. *J. Fluid Mech*, 517:281–301, 2004.

[66] M.L. Waite and P.K. Smolarkiewicz. Instabilty and breakdown of a vertical vortex pair in a strongly stratified fluid. *J. Fluid Mech.*, 606:239–273, 2008.

[67] R.M. Wald. *General Relativity*. University of Chicago Press, 2010.

[68] F. Waleffe. On the three-dimensional instability of strained vortices. *Phys. Fluids A*, 3:76, 1990.

[69] D.S. Watkins. *The Matrix Eigenvalue Problem: GR and Krylov Subspace Methods*. SIAM, 2007.

[70] S.E. Widnall, D.B. Bliss, and C.Y. Tsai. The instability of short waves on a vortex ring. *J. Fluid Mech*, 66:35, 1974.

[71] Wikipedia. Aliasing sines. http://en.wikipedia.org/wiki/File:AliasingSines.svg. Accessed November 8th, 2013.

[72] Wikipedia. Wagon-wheel effect. http://en.wikipedia.org/wiki/Wagon-wheel_effect. Accessed November 8th, 2013.